X-Ray Study of Ejecta-Dominated Supernova Remnants with Suzaku

Hiroya Yamaguchi

Department of Physics, Graduate School of Science, Kyoto University
Kitashirakawa Oiwake-cho, Sakyo-ku, Kyoto, 606-8502, Japan
hiroya@cr.scphys.kyoto-u.ac.jp

This thesis was submitted to the Department of Physics,
Graduate School of Science, Kyoto University
on January 2008
in partial fulfillment of the requirements
for the degree of Doctor of Philosophy in physics.

Abstract

We present the results of spectral and spatial studies of the young supernova remnants (SNRs: SN 1006, E0509–67.5, RCW 86, Tycho, and N103B), using the data obtained by the Suzaku satellite.

Almost all of the heavy elements which exist in the present universe have been synthesized in stars, and ejected to interstellar space by supernova (SN) explosions. Therefore, we are motivated to study the nucleosynthesis and explosion mechanisms of SNe, in order to understand chemical evolution of the universe. The young SNRs are bright and dominated by the emission from ejecta, and hence they provide fruitful information about the elements synthesized by the SNe.

From SN 1006, we detected the K-shell emission from Fe, for the first time. The full-band spectrum extracted from southeast of the remnant was well-fitted with a model consisting of three optically thin thermal non-equilibrium ionization plasmas and a non-thermal component. Two of the thermal components are due to ejecta, and have different ionization ages. The other thermal component is associated with the swept-up interstellar medium (ISM). The Fe-K emission was found in the ejecta with the lower ionization age.

The full-band spectrum of E0509–67.5 could be well-described by a composite model which was very similar to the best-fit model for the SN 1006 spectrum, but an ISM component was not required. The relative abundances of the ejecta component strongly suggest that this remnant is a Type Ia SN origin.

In the analysis of the northwestern shell of RCW 86, we revealed for the first time the morphology of the Fe-K emission in this region. The origin of the emission was found to be Fe-rich ejecta heated by the reverse shock very recently. The morphology and the plasma age of the ejecta suggest that the evolution of the reverse shock in RCW 86 is quite different from position to position, because the density of the ISM around this SNR has a large spatial variation.

Analyzing the high-quality Fe-K line spectra extracted from Tycho and N103B, we gave the tight constraints to the ionization ages of Fe-K ejecta in each SNR. Additionally, we detected Cr-K lines from both the SNRs, for the first time.

In all of the Type Ia SNRs which we observed (SN 1006, E0509–67.5, Tycho, and N103B), we found that the ionization ages of Fe (in the ejecta) are significantly lower than those of the lighter elements. It suggests that the Fe ejecta have been heated by reverse shock more recently than the other elements, because it concentrates toward the center of the remnant. At least in the Type Ia SN explosion, the ejecta mixing effect inside the progenitor star is suggested to be almost negligible.

Contents

Chapter 1

Introduction

Figure 1.1 shows abundance ratio of elements ($1 \leq Z \leq 30$) in the solar photosphere, called "solar abundance" (Anders & Grevesse 1988), which is almost consistent to the average element abundance ratio of the present universe. Immediately after the beginning of the universe, elements other than hydrogen and helium (and tiny light elements such as lithium) did not exist. At present, however, various heavy elements exist abundantly, as shown in figure 1.1. In addition to the elements shown in this figure, the universe consists of more than 90 kinds of elements up to uranium, and about 280 kinds of their isotopes. Almost all of these main heavy elements were synthesized in stars, and were ejected to interstellar space by supernova (SN) explosions. Nucleosynthesis (nuclear

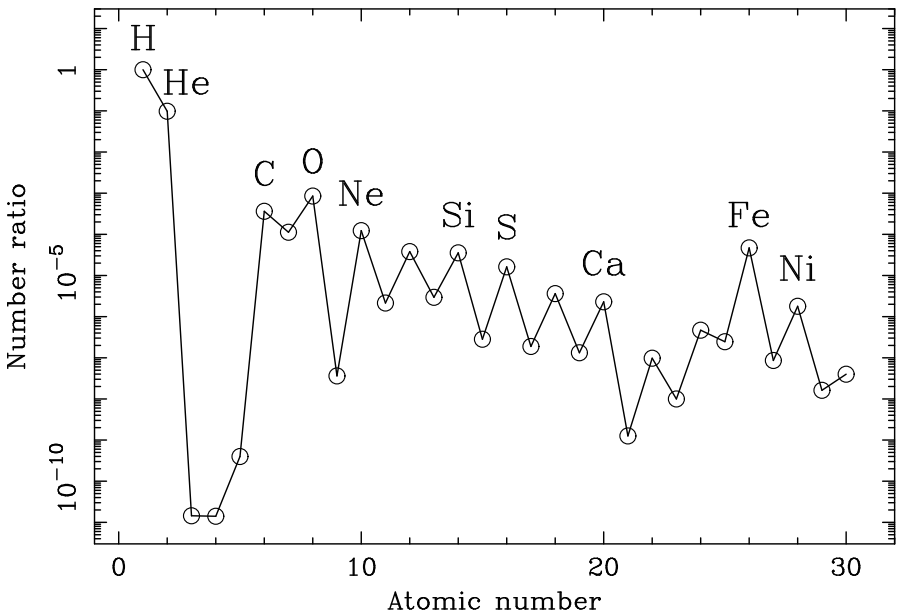

Fig. 1.1.—: Abundances of elements (relative to H) in the solar photosphere (Anders & Grevesse 1988).

fusion) is performed very actively just at the moment of the SN explosion as well. Therefore, we are motivated to study the abundance ratio and total amounts of the heavy elements ejected by each SN in order to understand chemical evolution of the universe.

Although SN explosions are extensively studied by optical observations, since the density of SN ejecta immediately after the explosion is quite high, the light emitted from inside matters cannot reach to the stellar surface directly. Therefore, we can only obtain the information of the synthesized elements laid on the surface layer of SNe. However, the remnants of SNe, supernova remnants (SNRs), compose high temperature plasmas by interacting with interstellar medium (ISM), and provide X-rays (or light in other wavelength) for a few tens of thousands of years after the explosion. Since the plasma is optically thin, all the elements included in the SNRs can be observed by X-rays directly at the same time. This is the most remarkable advantage of the X-ray observation on SNRs.

Especially, young SNRs whose ages are a few hundred or about a thousand years are not only bright but also dominated by the emission from ejecta (compared with the emission from swept-up ISM). Therefore, the observation on the young SNRs is the best method to investigate the abundances of the elements synthesized by the SNe.

Since the abundances of SNRs can be known by measuring the intensities of the emission lines from highly ionized heavy elements, the detector sensitivity for the line spectrum is essential to the accurate measurements. Suzaku, the newest Japanese X-ray astronomy satellites, has good energy resolution, high efficiency, and low background level for diffuse sources. Especially, it is superior to the other X-ray missions, in the sensitivity for the K-shell line emission from Fe, one of the main products of SN explosions.

This thesis focuses on the study of X-ray emission from young SNRs utilizing the excellent performances of Suzaku. In chapters 2 and 3, we describe the reviews of SNe and SNRs, respectively. The basic characteristics of the instruments on board Suzaku which we used in this work are summarized in chapter 4. The following chapters provide the first results on the analyses of individual SNRs with Suzaku: SN 1006 in chapter 5, E0509–67.5 in chapter 6, RCW 86 in chapter 7, and Tycho and N103B in chapter 8. SN 1006, RCW 86, and Tycho are historical SNRs in our Galaxy (the Milky Way). while E0509–67.5 and N103B are the young SNRs in the Large Magellanic Cloud. Combining all the works, we develop the discussions in chapter 9, and we finally summarize our findings in chapter 10.

Chapter 2

Supernovae and Nucleosynthesis

A Supernova (SN), an explosion of a star at the end of its lifetime, is one of the most dramatic events in the universe. The brightness of SN is comparable to that of whole galaxy, and its explosion energy is typically larger than 10^{51} ergs. It is believed that SN explosions occur per $\sim$30 years in our Galaxy (e.g., van den Bergh & Tammann 1991). SN explosions synthesize various heavy elements and release them into interstellar space. Furthermore, the shock wave generated by the SN explosions produce density fluctuation of interstellar matter (ISM), which promote new star formation. Therefore, SNe play a very important role in the chemical evolution of the universe. This chapter is devoted to explain the basic characteristics of SNe and their nucleosynthesis.

2.1 Nucleosynthesis

2.1.1 Stellar Nucleosynthesis

A star is maintained by balance between the thermal pressure and the gravity. Since stellar temperature (T) is in inverse proportion to a radius (R) of the star, if gravitational contraction progresses and the central temperature of the star exceeds the critical value, a thermo-nuclear fusion reaction will start.

When the central temperature is $\sim 10^7$ K, hydrogen is ignited via p-p chain process:

$$\begin{aligned} \mathrm{p} + \mathrm{p} &\rightarrow {}^2\mathrm{H} + e^+ + \nu_e + 1.44 \text{ MeV} \\ {}^2\mathrm{H} + \mathrm{p} &\rightarrow {}^3\mathrm{He} + \gamma + 5.49 \text{ MeV} \\ {}^3\mathrm{He} + {}^3\mathrm{He} &\rightarrow {}^4\mathrm{He} + 2\mathrm{p} + 12.86 \text{ MeV} , \end{aligned}$$

while the central temperature exceeds $\sim 2 \times 10^7$ K, the hydrogen ignition proceeds dominantly via CNO cycle:

$$\mathrm{p} + {}^{12}\mathrm{C} \rightarrow {}^{13}\mathrm{N} + \gamma + 1.95 \text{ MeV}$$

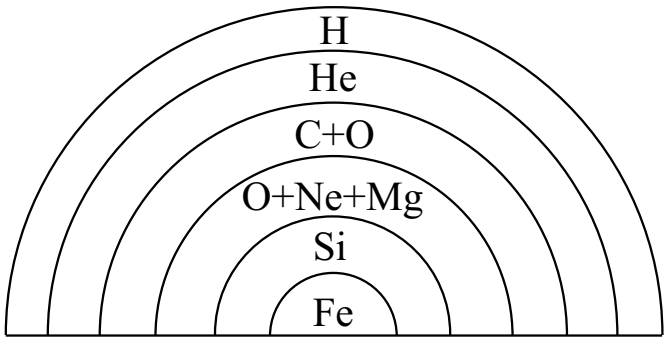

Fig. 2.1.—: Onion-like structure in massive, evolved stars just prior to core collapse. (The scale is not exact.)

$$
\begin{aligned}
{}^{13}\mathrm{N} &\rightarrow {}^{13}\mathrm{C} + e^{+} + \nu_e + 1.37 \text{ MeV} \\
\mathrm{p} + {}^{13}\mathrm{C} &\rightarrow {}^{14}\mathrm{N} + \gamma + 7.54 \text{ MeV} \\
\mathrm{p} + {}^{14}\mathrm{N} &\rightarrow {}^{15}\mathrm{O} + \gamma + 7.35 \text{ MeV} \\
{}^{15}\mathrm{O} &\rightarrow {}^{15}\mathrm{N} + e^{+} + \nu_e + 1.86 \text{ MeV} \\
\mathrm{p} + {}^{15}\mathrm{N} &\rightarrow {}^{12}\mathrm{C} + {}^{4}\mathrm{He} + 4.96 \text{ MeV} \ .
\end{aligned}
$$

Eventually, helium is synthesized from hydrogen by each process. The former is dominant in the sun. Stars spend most of their lifetime with the hydrogen burning, and hence they are called main-sequence stars.

When the supply of hydrogen at the core is exhausted, the outward pressure is no longer created. Then, the core begins to collapse, causing a rise in temperature and pressure which becomes high enough to ignite helium, and carbon and oxygen are synthesized by helium burning. This precess progresses quickly in stars whose mass is larger than $\sim 2M_{\odot}$. If the stellar mass exceeds $\sim 8M_{\odot}$, carbon burning takes place, and O+Ne+Mg core is produced. If the mass is larger than $\sim 10M_{\odot}$, silicon is synthesized by O burning, and Fe is synthesized by Si burning. As a result, the star has an onion-like structure as shown in figure 2.1, at the final stage of its evolution. Such a massive star finally becomes a core-collapse SN (section 2.4).

2.1.2 Explosive Nucleosynthesis

The elements synthesized by explosive nuclear fusion depend on the temperature and density. The relation between dominant nucleosynthesis processes and temperature are summarized in table 2.1. Since the explosive nucleosynthesis must take place quickly before the temperature decreasing, it requires higher temperature than the stellar nucleosynthesis.

When the maximum temperature is $\sim 2 \times 10^{9}$ K, explosive carbon burning takes place:

$$
{}^{12}\mathrm{C} + {}^{12}\mathrm{C} \rightarrow {}^{4}\mathrm{He} + {}^{20}\mathrm{Ne} \ ,
$$

Table 2.1:: Explosive nucleosynthesis.

	Main products	Ignition temperature (K)
C & Ne burning	Ne, O, Mg, Si	2×10^9
O burning	O, Si, S, Ar, Ca	3–4×10^9
Incomplete Si burning	Si, S, Ar, Ca	4×10^9
Complete Si burning	Fe, Co, Ni, Zn	5×10^9

and explosive neon burning takes place, at the same temperature. Main reactions of the Ne burning are as follows:

$$\begin{aligned} {}^{20}\mathrm{Ne}+\gamma &\rightarrow {}^{4}\mathrm{He}+{}^{16}\mathrm{O} \\ {}^{20}\mathrm{Ne}+{}^{4}\mathrm{He} &\rightarrow \gamma+{}^{24}\mathrm{Mg} \\ {}^{24}\mathrm{Mg}+{}^{4}\mathrm{He} &\rightarrow \gamma+{}^{28}\mathrm{Si}\ . \end{aligned}$$

If the maximum temperature is 3–4×10^9 K, explosive oxygen burning takes place:

$$\begin{aligned} {}^{16}\mathrm{O}+{}^{16}\mathrm{O} &\rightarrow {}^{4}\mathrm{He}+{}^{28}\mathrm{Si} \\ {}^{16}\mathrm{O}+{}^{16}\mathrm{O} &\rightarrow \gamma+{}^{32}\mathrm{S}\ . \end{aligned}$$

Furthermore, ^{36}Ar and ^{40}Ca are synthesized by the reaction between ^{32}Si and ^{4}He. If the temperature exceeds $\sim 4\times10^9$ K, explosive silicon burning mainly takes place. Silicone and sulfur (and so on) absorb the nucleus of a helium and synthesize heavy elements, such as chromium, iron, nickel, and zinc. In particular, a large amount of ^{56}Ni are synthesized in the complete Si burning process. As described in the following section, the radioactive decay of ^{56}Ni (through ^{56}Co to ^{56}Fe) generates the luminosity of SNe.

2.2 Classification of SNe

The fundamental classification scheme for SNe is traditionally based on their optical spectra near maximum light, as given in figure 2.2. This classification is not reflecting the difference in the origins of SNe as below-mentioned. If a optical spectrum lacks absorption lines of hydrogen Balmer series, the SN is classified as Type I. A spectrum contains the hydrogen lines, on the other hand, the SN is classified as Type II (Minkowski 1939; 1940). Type I SNe are sub-classified according to the presence or absence of the strong Si II absorption feature at 6150 Å (e.g., Elias et al. 1985). The SNe with strong Si line spectrum are defined as Type Ia, while the other Type I SNe have further subclasses: Type Ib whose spectrum contains He lines, and Type Ic without He lines (Wheeler et al. 1987). On the other hand, subclasses of Type II SNe are distinguished by the shape of their light curves. Those with a pronounced "plateau", producing a nearly constant luminosity ∼100 days, are termed Type II-P, while those with a nearly linear decline in magnitude with time from

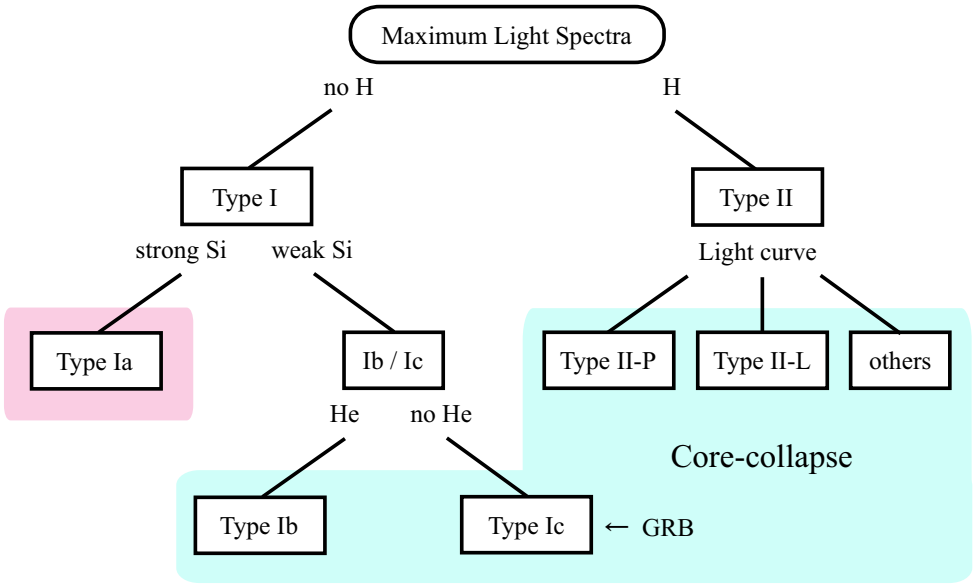

Fig. 2.2.—: Classification sheme for supernovae based on the early spectra and light curve features.

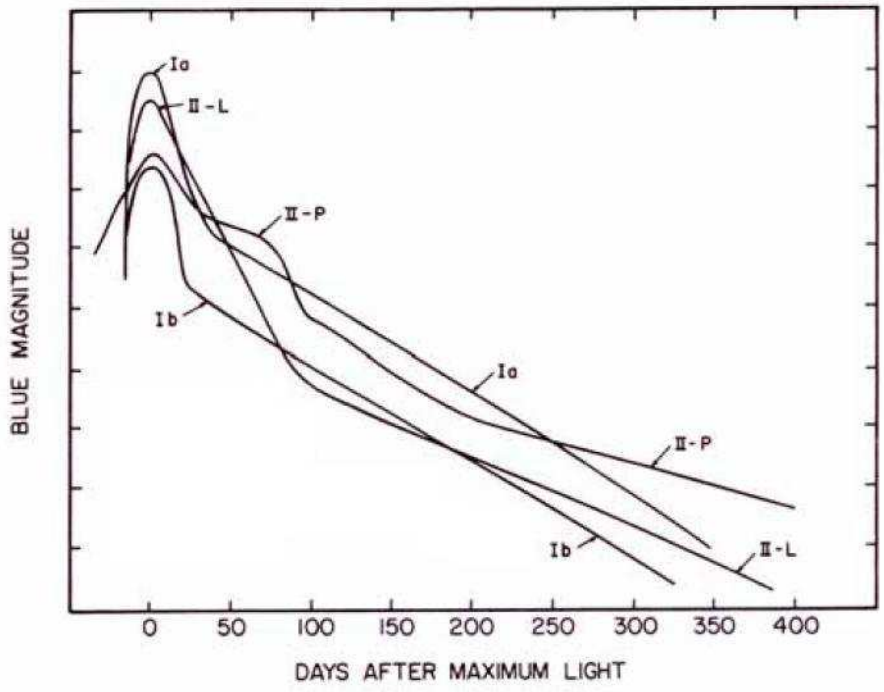

Fig. 2.3.—: Light curves for Type Ia, Ib, II-P, and II-L supernovae (Wheeler et al. 1990).

peak are termed Type II-L (e.g., Barbon et al. 1973). The typical light curves of each type of SNe are shown in figure 2.3. Although SN 1987A, occurred in the Large Magellanic Cloud (LMC) on 1987, is classified into Type II SN, the shape of its light curve is agreed with neither Type II-P nor II-L.

The progenitors of Type Ia SNe are now believed to be near-Chandrasekhar mass ($\sim 1.4 M_\odot$) white dwarfs, while Type II progenitors are believed to be massive stars ($M \gtrsim 10 M_\odot$). Details of Type Ia and II are described in sections 2.3 and 2.4, respectively. Although the Type Ib spectrum lacks H absorption lines, the property of their light curves is very similar to that of Type II SNe. Furthermore, Type Ib SNe are observed only in spiral galaxies and star forming regions. Therefore, the progenitors of Type Ib SNe are thought to be massive stars that have lost their hydrogen envelope. Wolf-Rayet stars are the possible progenitors, because they lose their outer hydrogen envelope by means of very strong stellar wind. The progenitors of Type Ic are also believed to be massive stars. There is some evidence that a few percent of the Type Ic SNe may be the progenitors of γ-ray bursts (GRB).

2.3 Type Ia SNe

Type Ia SNe are observed in all types of galaxies including elliptical galaxies, where no massive stars exist, and not concentrated in spiral arms (e.g., Wheeler 1982). The lack of absorption lines of hydrogen in the early-time optical spectra of Type Ia SNe suggests that progenitors of Type Ia SNe have no outer hydrogen envelope. From these facts, thermonuclear explosions of mass-accreting C+O white dwarfs in binary systems have been considered to be the most plausible models for Type Ia SNe (e.g., Nomoto 1982).

If the accretion from the companion star is as rapid as $\dot{M} \gtrsim 4 \times 10^{-8} M_\odot$ yr^{-1}, the white dwarf can increase the C+O core mass. Especially at $\dot{M} \gtrsim 4 \times 10^{-6} M_\odot$ yr^{-1}, the accreting white dwarf blows off a strong stellar wind, and increases the core mass by steady hydrogen burning with the rate of $\sim 10^{-6} M_\odot$ yr^{-1} (Hachisu et al. 1996). When the mass of the white dwarf reaches about the Chandrasekhar limit ($\sim 1.4 M_\odot$), the central density becomes near 2×10^9 g cm^{-3}, and the gravity exceeds the electron degeneracy pressure. As a result, the carbon burning is ignited at the core. Nuclear fusion advances explosively, and the star is totally disrupted by the nuclear reaction energy, leaving no neutron star nor black hole.

First, Arnett (1969) proposed that the flame front propagates at a supersonic speed ("detonation wave"). However, this theory failed because most of the material of the white dwarf are burned to ^{56}Ni, which is contradictory to the fact that the strong absorption lines of Si are observed in the spectra of Type Ia SNe. Then, the carbon deflagration model, whose flame speed is 10–30% of the sound speed, was proposed (W7 model: Nomoto et al. 1976; 1984). This model successfully reproduces the observational abundance ratio of the heavy elements, and hence is widely used as "the standard model" for the Type Ia SNe. By the carbon deflagration, $\sim 0.6 M_\odot$ of ^{56}Ni is synthesized in the inner region of the star, and it powers the light curves of Type Ia SNe thorough radioactive

decays via ^{56}Ni$\rightarrow^{56}$Co$\rightarrow^{56}$Fe. An e-folding time of ^{56}Co is $\sim$111 days, which corresponds to the rate of the light curve decline of $\sim$0.01 mag day^{-1}.

However, the result of carbon deflagration depends on its flame speed, which is highly uncertain. If the initial flame speed is much lower than that of W7 model, the hydrodynamical behavior is very different. The deflagration might induce a detonation at low density layers. In the delayed detonation model (Khokhlov 1991; Woosley & Weaver 1994) the deflagration wave is assumed to be transformed into detonation at a certain layer during the first expansion phase. Iwamoto et al. (1999) constructed delayed detonation models with several parameterized transition densities. The slow deflagration with a flame speed of 1.5% of the local sound speed is artificially transformed into detonation when the density ahead of the flame decreases to 3.0, 2.2, and 1.7×10^7 g cm^{-3} (WS15DD3, WS15DD2, and WS15DD1, respectively). They found that the amount of synthesized ^{56}Ni (and the other elements) changes slightly.

In both models of the fast deflagration (W7) and the delayed detonation, the total explosive energy is estimated to be $\sim$1.3–1.5$\times10^{51}$ ergs. Furthermore, the peak luminosity of the light curve was almost consistent across Type Ia SNe, which led to the use of Type Ia SNe as a standard candle to determine cosmological parameters.

Nucleosynthesis

The Mass of synthesized heavy elements by Type Ia SNe are given in table 2.2, which are predicted by the deflagration model (W7: Nomoto et al. 1984) and the delayed detonation models (Iwamoto et al. 1999). Figure 2.4 shows the comparison between the abundance ratio of the W7 and that of the WS15DD2. The ratio predicted by the other delayed detonation model is similar to the WS15DD2. We can see the abundances of the heavy elements such as Si and Fe (relative to O-Ne-Mg) are larger in the delayed detonation model than in the W7 model.

Table 2.2:: Predicted mass of heavy elements nucleosynthesized by Type Ia supernova.

Species	Mass ($M_\odot$)			
	W7*	WS15DD1†	WS15DD2†	WS15DD3†
C	3.2×10^{-2}	5.4×10^{-3}	9.0×10^{-3}	1.7×10^{-2}
N	2.6×10^{-9}	2.8×10^{-4}	2.7×10^{-4}	1.8×10^{-4}
O	1.4×10^{-1}	8.8×10^{-2}	6.6×10^{-2}	5.6×10^{-2}
Ne	1.3×10^{-2}	1.5×10^{-3}	1.0×10^{-3}	1.3×10^{-3}
Mg	2.3×10^{-2}	7.7×10^{-3}	4.5×10^{-3}	2.6×10^{-3}
Si	1.6×10^{-1}	2.7×10^{-1}	2.1×10^{-1}	1.6×10^{-1}
S	8.4×10^{-2}	1.6×10^{-1}	1.2×10^{-1}	9.5×10^{-2}
Ar	2.2×10^{-2}	3.2×10^{-2}	2.5×10^{-2}	1.9×10^{-2}
Ca	4.1×10^{-2}	3.1×10^{-2}	2.4×10^{-2}	1.9×10^{-2}
Cr	1.1×10^{-2}	2.1×10^{-2}	1.7×10^{-2}	1.4×10^{-2}
Fe	7.7×10^{-1}	6.7×10^{-1}	7.9×10^{-1}	8.7×10^{-1}
Ni	7.2×10^{-2}	3.8×10^{-2}	5.9×10^{-2}	7.3×10^{-2}

*Nomoto et al. (1984).

†Iwamoto et al. (1999).

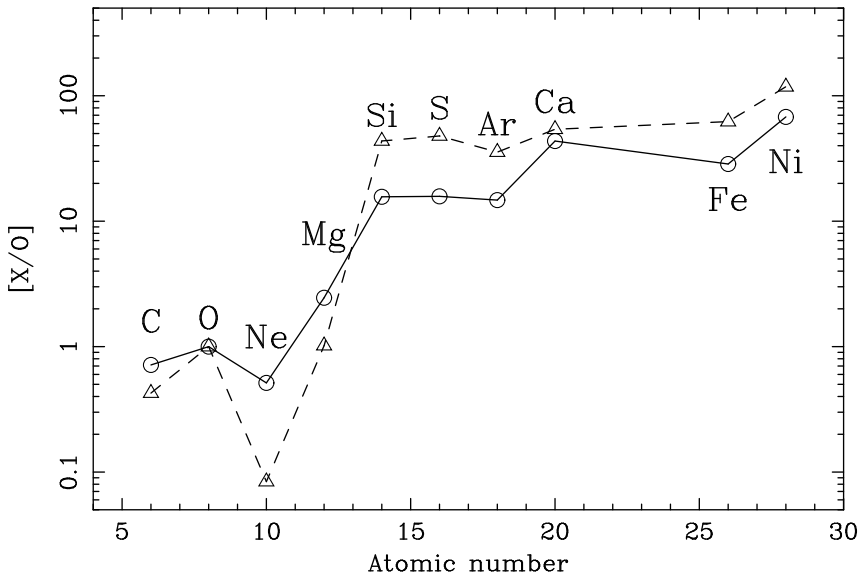

Fig. 2.4.—: Abundance ratio of elements (relative to solar values) in the carbon deflagration model (circle: W7 model by Nomoto et al. 1984) and the delayed detonation model (triangle: WS15DD2 model by Iwamoto et al. 1999). The ratio is normalized to oxygen.

2.4 Type II SNe

Since Type II SNe are observed in arms of spiral galaxies, their progenitors are believed to be massive stars. A star with more than $\sim 10 M_{\odot}$ finally has an onion-like structure (figure 2.1), and obtains an Fe core. Since Fe is the most stable element, the core can no longer generate nuclear energy. However, neutrino continue taking away the energy from the star, and hence the density and temperature in the Fe core continually increase due to the subsequent contraction. When the internal temperature exceeds $\sim 3 \times 10^9$K, photo-disintegration of Fe nuclei takes place:

$$\begin{aligned} {}^{56}\mathrm{Fe} &\rightarrow 13\ {}^{4}\mathrm{He} + 4\mathrm{n} - 124.4\ \mathrm{MeV} \\ {}^{4}\mathrm{He} &\rightarrow 2\mathrm{p} + 2\mathrm{n} - 28.3\ \mathrm{MeV}\ , \end{aligned}$$

and the thermal energy is absorbed, as a result. Then, the star cannot support the gravitational force any more and collapses gravitationally.

The energy explosively released by the infalling matter creates a shock wave. It propagates outward and reaches the outermost part of the star. The total energy generated by the gravitational collapse is $\sim 10^{53}$ ergs. However, most of the energy are carried off by neutrinos, and the kinetic energy of the shock wave is typically 10^{51} ergs. After the explosion, a neutron star or a stellar black hole is left. The Crab pulsar (figure 2.5) is one of the most famous neutron star, which was left by a Type II SN explosion of A.D. 1054.

Fig. 2.5.—: Composite image of Crab pulsar and its nebula. Red and blue are respectively optical image from Hubble telescope and X-ray image from Chandra.

A decay rate of the Type II SN light curve is typically lower than that for the Type Ia SN. Since the progenitor of Type II SN has a thick hydrogen envelope, the SN possesses the thermal energy due to the shock heating over a long duration. Therefore, the light curve of most Type II SNe shows plateau (II-P in figure 2.3). After the plateau phase, the light curve is powered by ^{56}Ni decay. The shape of Type II-L SN light curve is probably due to the expulsion of most of the hydrogen envelope of the progenitor star.

Nucleosynthesis

The shock wave propagating in the star elevates the temperature of the mantle, and leads explosive nucleosynthesis. The relation between the temperature (T) behind the shock, the explosion energy (E), and the stellar radius (R) is given as

$$E \sim \frac{4\pi}{3} R^3 a T^4 \ , \tag{2.1}$$

where $a = 7.57 \times 10^{-15}$ ergs cm^{-3} K^{-4}. Therefore, the maximum temperature, which decides the synthesized elements (see table 2.1), is lower for the outer layer. Since the temperature of the outermost layer is lower than that of ignition temperature of carbon burning, the abundances of the ejected material are also affected by the envelope, which depends on the mass of the star. The mass and relative abundance of the synthesized elements for Type II SNe with $15M_\odot$, $20M_\odot$, and $25M_\odot$ are given in table 2.3 and figure 2.6, respectively (Thielemann et al. 1996).

Table 2.3:: Predicted mass of heavy elements nucleosynthesized by core-collapse supernovae. (Thielemann et al. 1996)

Species	Mass ($M_\odot$)		
	SN II ($15M_\odot$)	SN II ($20M_\odot$)	SN II ($25M_\odot$)
C	8.3×10^{-2}	1.1×10^{-1}	1.5×10^{-1}
N	5.4×10^{-3}	2.7×10^{-3}	9.5×10^{-4}
O	4.4×10^{-1}	1.5	3.0
Ne	4.1×10^{-2}	2.6×10^{-1}	6.3×10^{-1}
Mg	4.8×10^{-2}	1.8×10^{-1}	2.3×10^{-1}
Si	7.5×10^{-2}	1.0×10^{-1}	1.2×10^{-1}
S	2.3×10^{-2}	2.5×10^{-2}	4.1×10^{-2}
Ar	3.8×10^{-3}	4.5×10^{-3}	7.4×10^{-3}
Ca	3.1×10^{-3}	3.9×10^{-3}	6.2×10^{-3}
Cr	9.5×10^{-4}	1.1×10^{-3}	1.5×10^{-3}
Fe	1.4×10^{-1}	8.0×10^{-2}	5.8×10^{-2}
Ni	1.1×10^{-2}	7.4×10^{-3}	2.2×10^{-3}

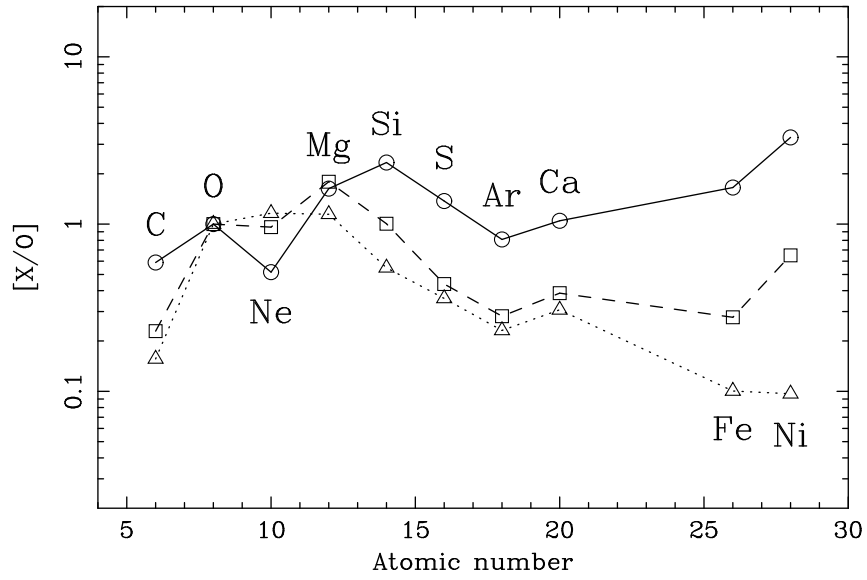

Fig. 2.6.—: Abundance ratio of elements (relative to solar values) synthesized by core-collapse supernovae with stellar mass of $15M_\odot$ (circle), $20M_\odot$ (square), and $25M_\odot$ (triangle), predicted by Thielemann et al. (1996). The ratio is normalized to oxygen.

Chapter 3

Supernova Remnants

A supernova remnant (SNR) is the structure resulting from the SN explosion. It consists of ejected material (ejecta) expanding from the explosion, and the swept-up ISM. Most SNRs have been discovered in radio survey. They are distinguished from H II regions by the relatively flat shape of their radio spectra. Now, 265 SNRs are identified in our Galaxy (Green 2006), and about a half of them are observed by X-rays. In this chapter, we explain the overview of physics concerning SNRs: the macroscopic evolution of SNRs, the heating process performed by their shock wave, and the mechanism of X-ray emission from the SNRs.

3.1 Evolution of SNRs

The evolution of SNRs can be divided into several phases. Their conditions are mainly determined by the ratio between the mass of ejecta ($M_{\rm Ej}$) and that of swept-up ISM ($M_{\rm ISM}$). Here, we assume that the density of the ambient medium is uniform. The detailed descriptions are shown in Truelove & McKee (1999) for young stages (from free expansion phase through Sedov phase) and Cioffi et al. (1988) for evolved stages (radiation phase).

3.1.1 Free Expansion Phase

Since $M_{\rm ISM}$ is negligible compared to $M_{\rm Ej}$ in the initial phase, the ejecta expand without deceleration. The expansion velocity ($\sim 10^4$ km s^{-1}) is much larger than the sound speed in the ambient gas (~ 10 km s^{-1}), and hence shock wave (blast wave) precede the ejecta. The physics of the shock wave is described in next section. Since most of the explosion energy (E) is released kinetically (only 2–3% of the energy converted into thermal energy), the expansion velocity (v_s) and the radius (R_s) of the shock front can be expressed by

$$v_s = \sqrt{\frac{2E}{M_{\rm Ej}}} = 8.5 \times 10^8 \left(\frac{E}{10^{51}{\rm erg}}\right)^{1/2} \left(\frac{M_{\rm Ej}}{1.4 M_\odot}\right)^{-1/2} \ \ [{\rm cm\ s^{-1}}] \ , \tag{3.1}$$

$$R_s = v_s t \ , \tag{3.2}$$

where t is the time since the explosion. The mass of the ISM swept-up by the blast wave is described as

$$M_{\rm ISM} = \frac{4}{3}\pi R_s^3 \mu m_{\rm H} n_0 \ , \tag{3.3}$$

where μ, $m_{\rm H}$, and n_0 are mean atomic weight of solar metallicity per hydrogen, mass of hydrogen atom, and hydrogen number density of the ISM, respectively. Since the free expansion phase continues until that $M_{\rm ISM}$ becomes comparable to $M_{\rm Ej}$, its timescale can be approximately estimated from equation 3.1, 3.2, and 3.3 to be

$$t \sim 2.5 \times 10^2 \left(\frac{E}{10^{51}\ {\rm erg}}\right)^{-1/2} \left(\frac{M_{\rm Ej}}{1.4 M_\odot}\right)^{5/6} \left(\frac{\mu}{1.4}\right)^{-1/3} \left(\frac{n_0}{1\ {\rm cm}^{-3}}\right)^{-1/3} \ [{\rm yr}] \ . \tag{3.4}$$

Therefore, this phase typically continues for a few hundred years. If the ambient density is low, however, the timescale becomes longer. SN 1987A is believed to be in this phase.

3.1.2 Adiabatic Phase (Sedov Phase)

When $M_{\rm ISM}$ becomes much larger than $M_{\rm Ej}$ (typically $M_{\rm ISM} \gtrsim 10 M_{\rm Ej}$), the blast wave is decelerated by the swept-up ISM. However, energy loss via radiation is still negligible compared with its initial energy. Therefore, the SNR expands adiabatically. In this stage, the shock evolution can be approximated with that generated by a point explosion in a uniform medium, which is well explained by a self-similar solution derived by Sedov (1959). Therefore, this phase is often called as "Sedov phase". The pattern of the gas flow can be characterized only by two parameters, E and n_0. The radius (R_s) and velocity (v_s) of the blast wave, and the mean temperature just behind the shock front (T_s) are written as

$$R_s = 4 \times 10^{19} \left(\frac{t}{10^4 {\rm yr}}\right)^{2/5} \left(\frac{E}{10^{51} {\rm erg}}\right)^{1/5} \left(\frac{n_0}{1 {\rm cm}^{-3}}\right)^{-1/5} \ [{\rm cm}] \tag{3.5}$$

$$v_s = \frac{dR_s}{dt} = 5 \times 10^7 \left(\frac{t}{10^4 {\rm yr}}\right)^{-3/5} \left(\frac{E}{10^{51} {\rm erg}}\right)^{1/5} \left(\frac{n_0}{1 {\rm cm}^{-3}}\right)^{-1/5} \ [{\rm cm\ s}^{-1}] \tag{3.6}$$

$$T_s = 3 \times 10^6 \left(\frac{t}{10^4 {\rm yr}}\right)^{-6/5} \left(\frac{E}{10^{51} {\rm erg}}\right)^{2/5} \left(\frac{n_0}{1 {\rm cm}^{-3}}\right)^{-2/5} \ [{\rm K}] \ . \tag{3.7}$$

In this phase, the density of the swept-up ISM is much higher than that of ejecta, and hence X-ray emission is dominated by the ISM. Therefore, we can determine T_s and n_0 from an X-ray spectrum of the SNR. If the distance to the SNR is known, R_s is also determined observationally. Then, the age of the SNR (t) and the explosion energy (E) can be derived according to equation 3.5 and 3.7.

The Sedov phase continues for a few ten thousand years. Until the end of this phase, $\sim 70\%$ of the initial explosion energy is converted into thermal energy of swept-up ISM (Chevalier 1974).

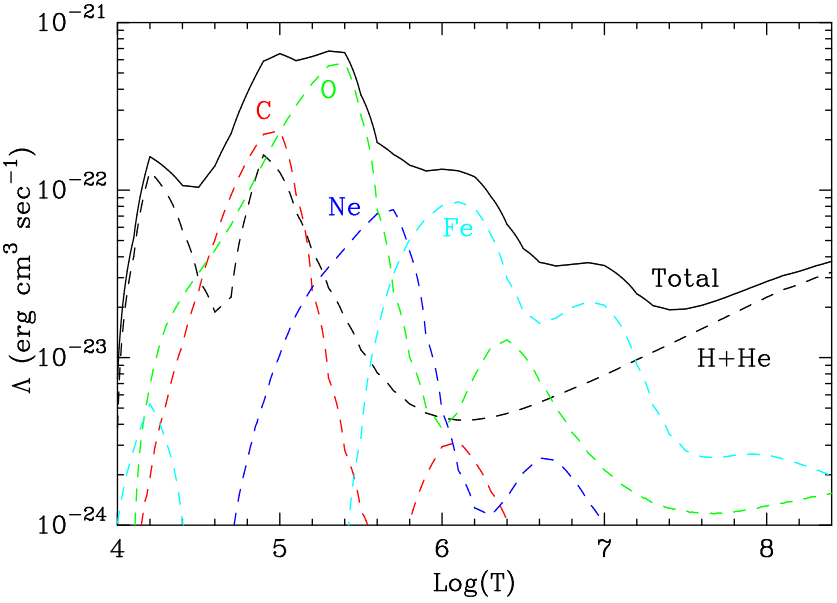

Fig. 3.1.—: Cooling coefficient for an optically-thin thermal plasma with solar abundances (Anders & Grevesse 1989) as a function of plasma temperature. The individual contributions from major elements are shown with dashed lines, and black solid line shows the total value.

3.1.3 Radiative Cooling Phase

In the Sedov phase, the temperature behind the shock (T_s) decreases with time, according to equation 3.7. Then, the cooling rate gradually increases, and hence the evolution is no longer adiabatic. As shown in figure 3.1, when the temperature drops to about (2–3)$\times 10^5$ K, electrons efficiently recombine with the heavy elements which are dominant in solar abundance ISM, such as carbon and oxygen, and the gas radiates ultraviolet emission lines. Since the pressure in the shell becomes lower as the temperature decreases, the materials in the shell are further compressed, and cool more rapidly. It provides a dense shell, while the interior is still hot and expands adiabatically. Thus, the shell is driven by the pressure of the internal gas according to $PV^\gamma = $ const., where P and V are the mean pressure and the volume of the internal gas respectively, and γ is the specific heat ratio ($= C_p/C_V$). For the non-relativistic single atomic gas, $\gamma = 5/3$. Then, the shock expands with the time dependency of

$$R_s \propto t^{2/7} \ . \tag{3.8}$$

This stage is called pressure-driven snowplow phase (McKee & Ostriker 1977). Cygnus Loop is believed to be in this phase.

As the temperature cools down further, the pressure can be ignored and the cool shell expands at a constant radial momentum ($M_s v_s = $ const., where M_s is the mass of the shell) with the time dependency of

$$R_s \propto t^{1/4} \ . \tag{3.9}$$

This stage is called momentum-conserving snowplow phase (Cioffi et al. 1988).

When the shock speed becomes comparable to the proper motion of surrounding ISM (10–20 km s^{-1}), the SNR lose its boundary between the outside and went out into the ISM. This phase is called as "Disappearance phase". The age of SNRs in this phase is larger than $\sim 10^6$ yr.

3.1.4 Transition Phase Between the Free Expansion and Sedov Stages

In subsections 3.1.1 and 3.1.2, we considered the limited situations of $M_{\rm ISM} \ll M_{\rm Ej}$ and $M_{\rm ISM} \gg M_{\rm Ej}$ (although energy loss is negligible). However, the transition phase between these two stages, when $M_{\rm ISM}$ is comparable to $M_{\rm Ej}$, is very important, because the most of young SNRs, such as Cas A and SN 1006, are probably in this stage. Figure 3.2 shows the *realistic* evolution of the blast wave between the self-similar limits of the free expansion phase and the Sedov phase.

In this transition phase, the interaction with ISM cannot be ignored, although it is not yet dominant. The swept-up ISM pushes back on the ejecta, which are thus decelerated. It causes another shock wave to propagate inward through the ejecta, called as "reverse shock" (McKee 1974). Therefore, the ejecta are compressed and heated by the reverse shock. The boundary between the ISM (shocked by the blast wave) and the ejecta (shocked by the reverse shock) is called the "contact discontinuity". The schematic view of SNRs in the transition phase is shown in figure 3.3. Only between the two shock waves, the material is hot enough to emit X-rays and this forms the bright shell of young SNRs. In the central region, ejecta is not hot and is still freely expanding. Such ejecta cannot emit X-rays, and hence its information cannot been received

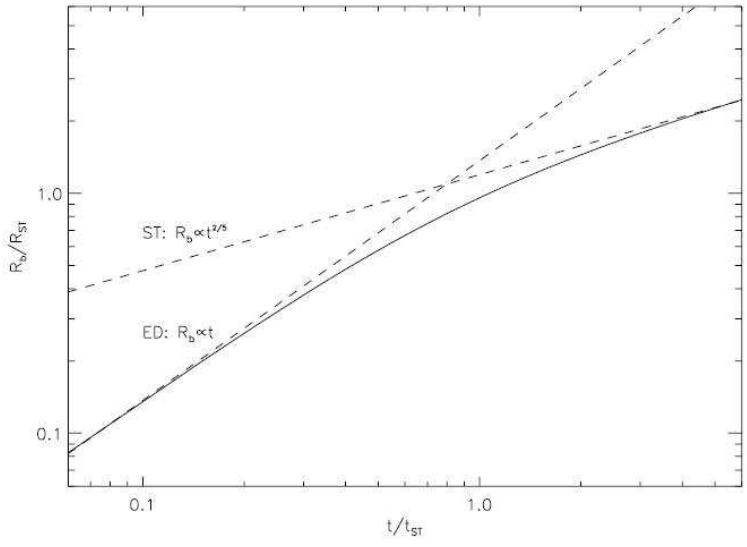

Fig. 3.2.—: Position of the blast wave shock as a function of time from a simulation of uniform ejecta expanding into a uniform ISM (Truelove & McKee 1999).

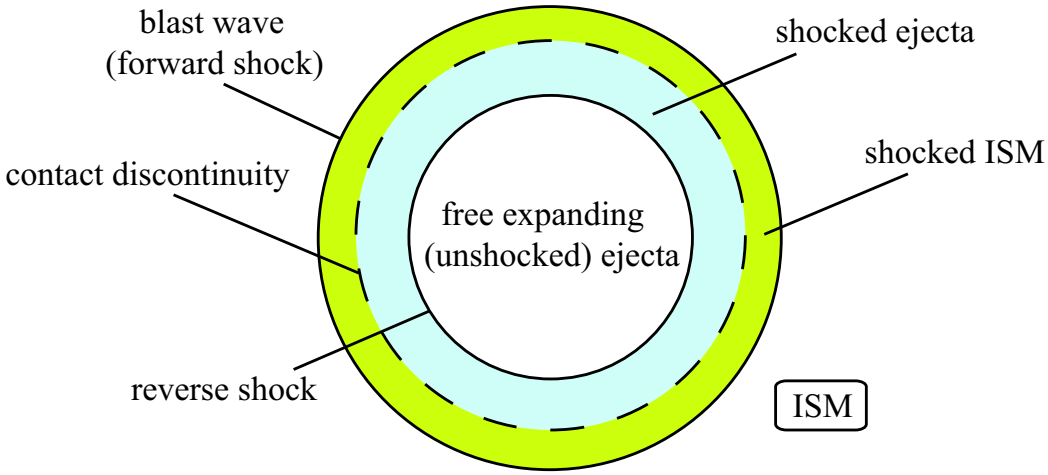

Fig. 3.3.—: Schematic view of SNRs in the transition phase. Only the shocked material (between the forward and reverse shocks) is hot enough to emit X-rays.

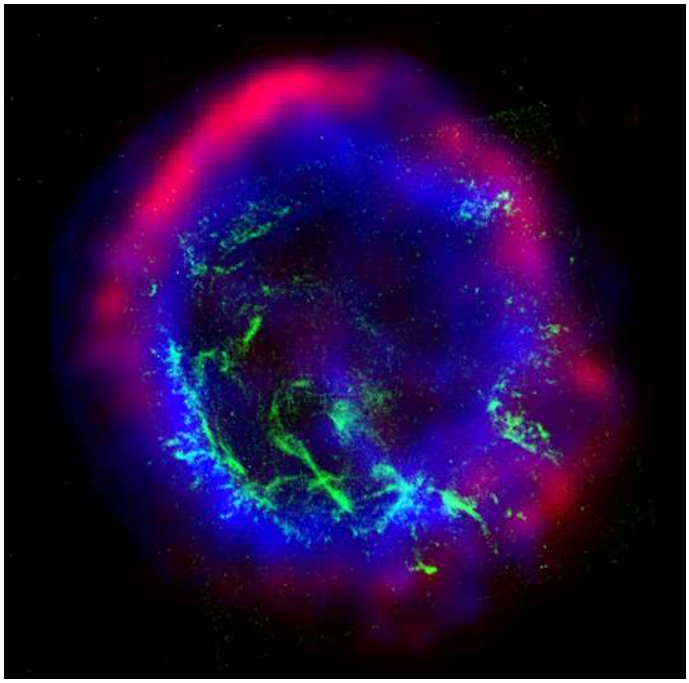

Fig. 3.4.—: Composite image of E0102–72, an SNR in the Small Magellanic Cloud. Red and blue respectively show the shocked ISM and the shocked ejecta. Green structures are the optical filaments. Credit: X-ray (NASA/CXC/SAO); optical (NASA/HST); radio: (ATNF/ ATCA)

directly. Figure 3.4 shows a typical composite image of E0102–72, a young SNR in the Small Magellanic Cloud (Gaetz et al. 2000). Blue shows X-rays from ejecta shocked by reverse shock, while red shows optical light from swept-up ISM.

As shown in figure 3.5, not only blast wave but also reverse shock initially propagate outward (as seen by an outside observer). After $M_{\rm ISM}$ becomes greater than $M_{\rm Ej}$, the reverse shock propagates back to the centre. In the case that uniform ejecta expand in homogeneous ISM, approximate shock trajectories in the moderate transition phase ($0.5 < t^* < 2.2$, in figure 3.5) are given as

$$R_b^* = (1.42t^* - 0.254)^{2/5} \tag{3.10}$$

$$R_r^* = t^*(0.779 - 0.106t^* - 0.533 \ln t^*) \tag{3.11}$$

for the blast wave and reverse shock, respectively (Truelove & McKee 1999). R^* and t^* are dimensionless values of radius and time normalized by these characteristic quantities: $R^* \equiv R/R_{\rm ch}$ and $t^* \equiv t/t_{\rm ch}$. $R_{\rm ch}$ and $t_{\rm ch}$ are those when $M_{\rm ISM} = M_{\rm Ej}$ is achieved. The shock trajectories for the cases that the ejecta distribution is not uniform but is power-law or exponential like are calculated by Truelove & McKee (1999) and Dwarkadas & Chevalier (1998) in details.

Note that, however, they do not treat effects of the convective or Rayleigh-Taylor instability. This instability appears when the blast wave is still inside the progenitor star and is believed to lead to mixing and clumping of the ejecta (e.g., Chevalier & Klein 1978; Muller & Arnett 1982), and arise again in the SNR evolution, at the contact discontinuity (e.g., Gull 1973; 1975). Therefore, geometry of SNRs is generally complicated by irregularities in both the ejecta and ISM: shock fronts are not exactly spherical (see figure 3.4).

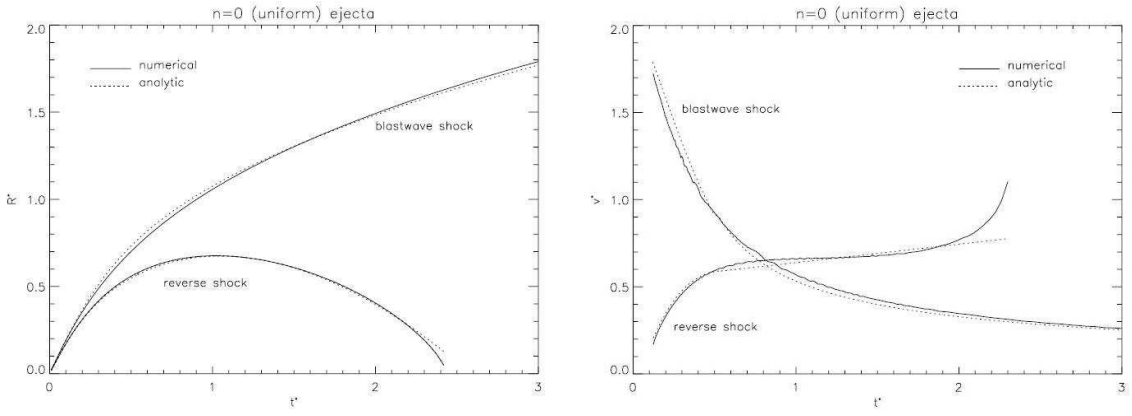

Fig. 3.5.—: Shock positions (left) and velocities (right) for blast wave and reverse shock in remnants of uniform ejecta. Note that the reverse shock velocity is measured in the frame of the unshocked ejecta ahead of it. Both figures are taken from Truelove & McKee (1999).

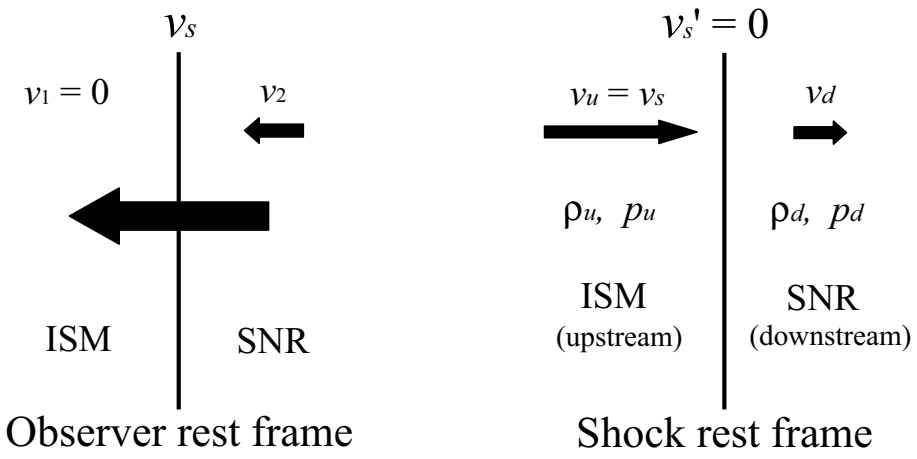

Fig. 3.6.—: A schematic view around the shock front in observer rest frame (left) and Shock rest frame (right). v, ρ, and p, are the velocity, density, and pressure, respectively.

3.2 Shock Wave Heating

When the shell of an SNR expands supersonically, a shock wave is formed, and the gas is compressed and heated. We here take a coordinate system in which the shock is at rest, and define upstream and downstream as figure 3.6. The tangential component of the gas velocity is assumed to be zero on both sides. Then, conservation of mass, momentum, and energy across the shock front can be expressed respectively as

$$\rho_u v_u = \rho_d v_d \tag{3.12}$$

$$\rho_u v_u^2 + p_u = \rho_d v_d^2 + p_d \tag{3.13}$$

$$\frac{1}{2}v_u^2 + w_u = \frac{1}{2}v_d^2 + w_d \ , \tag{3.14}$$

where ρ, v, p, and w are the density, velocity, pressure, and enthalpy of both upstream (subscript u) and downstream (subscript d), respectively. If the fluid is ideal gas, the enthalpy is given as

$$w = C_p T = \frac{\gamma p}{(\gamma - 1)\rho} \ , \tag{3.15}$$

where γ is the specific heat ratio ($= C_p/C_V$). Therefore, from equations 3.12, 3.13, 3.14, and 3.15, relations between the physical condition of the upstream and the downstream (Rankine-Hugoniot relations) are obtained as

$$\frac{\rho_u}{\rho_d} = \frac{v_d}{v_u} = \frac{(\gamma+1)p_u + (\gamma-1)p_d}{(\gamma-1)p_u + (\gamma+1)p_d} \tag{3.16}$$

$$\frac{p_u}{p_d} = \frac{(\gamma+1)\rho_u - (\gamma-1)\rho_d}{(\gamma+1)\rho_d - (\gamma-1)\rho_u} \tag{3.17}$$

$$\frac{T_d}{T_u} = \frac{p_d \rho_u}{p_u \rho_d} = \frac{p_d}{p_u}\frac{(\gamma+1)p_u + (\gamma-1)p_d}{(\gamma-1)p_u + (\gamma+1)p_d} \ . \tag{3.18}$$

For the velocities of the gas, we obtain

$$v_u^2 = \frac{1}{2\rho_u}[(\gamma-1)p_u + (\gamma+1)p_d] \tag{3.19}$$

$$v_d^2 = \frac{1}{2\rho_u}\frac{[(\gamma+1)p_u + (\gamma-1)p_d]^2}{(\gamma-1)p_u + (\gamma+1)p_d} \ . \tag{3.20}$$

Assuming the strong shock ($p_d/p_u \gg 1$), equations 3.16, 3.18, 3.19, and 3.20 can be respectively rewritten as

$$\frac{\rho_u}{\rho_d} = \frac{v_d}{v_u} = \frac{\gamma-1}{\gamma+1} \tag{3.21}$$

$$\frac{T_u}{T_d} = \frac{p_d}{p_u}\frac{\gamma-1}{\gamma+1} \tag{3.22}$$

$$v_u^2 = \frac{(\gamma+1)p_d}{2\rho_u} \tag{3.23}$$

$$v_d^2 = \frac{(\gamma-1)^2 p_d}{2(\gamma+1)\rho_u} \ . \tag{3.24}$$

Here, v_u equals to v_s, the shock velocity at the rest frame of the upstream (see figure 3.6), Using equations 3.21 and 3.24, therefore, we can derive the mean post-shock temperature:

$$kT_d = \mu m_{\rm H}\frac{p_d}{\rho_d} = \frac{2(\gamma-1)}{(\gamma+1)^2}\mu m_{\rm H} v_s^2 \ , \tag{3.25}$$

where k, μ, and $m_{\rm H}$ are the Boltzmann constant, the mean atomic weight, and the hydrogen mass, respectively. For the non-relativistic single atomic gas ($\gamma = 5/3$), the ratio (among the upstream and downstream) of the density and velocity are derives as $\rho_d/\rho_u = 4$ and $v_d/v_u = 1/4$, respectively. Moreover, the post-shock temperature is described as

$$kT_d = \frac{3}{16}\mu m_{\rm H} v_s^2 \ . \tag{3.26}$$

The shock wave heating can be understood as the energy conversion from the kinetic energy to the internal (thermal) energy.

3.3 Thermal X-Ray Emission from SNRs

In this section, we summarize thermal X-ray emission mechanisms concerning SNRs. They tell us a lot of informations about the SNR itself. Since the plasma in SNRs are optically-thin, the main emission processes which we observe are bremsstrahlung continuum and line emissions.

3.3.1 Bremsstrahlung

Charged particles in the Coulomb field of other charged particles emits radiation called bremsstrahlung or free-free emission. The most intense emission in neutral plasma is the bremsstrahlung from electrons by the Coulomb field of ions. The emission power of the emission per unit time, volume, and frequency is given by

$$\frac{dW}{dV\,dt\,d\nu} = \frac{16\pi^2 e^6}{3\sqrt{3}c^3 m_e^2 v_e} n_e n_i Z^2 g_{ff}(v,\ \nu)\ , \tag{3.27}$$

where n_e, n_i, e, m_e, v_e, c, Z, and g_{ff} are electron and ion density, charge unit, electron mass and velocity, light speed, and Gaunt factor, respectively. Gaunt factor is a certain function of the energy of electron and of the frequency of emission, reviewed in Bressaard & van de Hulst (1962), and Karzas and Latter (1961).

The shocked ISM and ejecta are heated up to $\sim 10^7$ K and become thin-thermal plasma ($n \lesssim 1$ cm^{-3}). When the electron temperature is kT_e, the probability dP that a particle has a velocity in the velocity range dv_e is estimated under the assumption of an isotropic distribution of velocities to be

$$dP \propto v^2 \exp\left(-\frac{m_e v_e^2}{2kT_e}\right) dv\ . \tag{3.28}$$

Combining equations 3.27 and 3.28, and performing the integral, the emission power of plasma in an isotropic thermal distribution (thermal bremsstrahlung) is derived as

$$\frac{dW}{dV\,dt\,d\nu} = \frac{32\pi e^6}{3mc^3}\left(\frac{2\pi}{3km_e}\right)^{1/2} T_e^{-1/2} Z^2 n_e n_i \mathrm{e}^{-h\nu/kT_e}\overline{g_{ff}} \tag{3.29}$$

$$= 6.8\times10^{-38} Z^2 n_e n_i T_e^{-1/2} \mathrm{e}^{-h\nu/kT_e}\overline{g_{ff}} \quad [\mathrm{ergs\ s^{-1}\ cm^{-3}\ Hz^{-1}}], \tag{3.30}$$

where $\overline{g_{ff}}(T_e,\ \nu)$ is a velocity averaged Gaunt factor. For typical thermal plasma emitting X-rays,

$$\overline{g_{ff}} = \left(\frac{3}{\pi}\frac{kT_e}{h\nu}\right)^{-1/2}\ . \tag{3.31}$$

The factor $T_e^{-1/2}$ comes from the fact that $dW/dV\,dt\,d\nu \propto v^{-1}$.

Integrating equation 3.29, the total power per unit volume emitted by thermal bremsstrahlung is obtained as

$$\frac{dW}{dt\,dV} = \frac{32\pi e^6}{3hmc^3}\left(\frac{2\pi kT_e}{3m_e}\right)^{1/2} Z^2 n_e n_i \overline{g_B} \tag{3.32}$$

$$= 1.4\times10^{-27} Z^2 n_e n_i T_e^{1/2}\overline{g_B} \quad [\mathrm{ergs\ s^{-1}\ cm^{-3}}], \tag{3.33}$$

The density and/or temperature of the plasma are higher, the power of the bremsstrahlung emission becomes higher. Therefore, we can investigate the densities (of electrons and ions) and electron temperature from the intensity and shape of the thermal continuum spectrum.

3.3.2 Line Emission

The transitions between two discrete quantum levels often accompany photon emission called line emission or bound-bound emission. In the pure Coulomb cases for hydrogen atom or other hydrogen-like ions (which have only one captured electron), such as He II, O VIII, and Si XIV, a fairly complete discussion of transition rates can be given by quantum theory. For hydrogen atom, the energy of a photon absorbed or emitted in a transition between two discrete levels with principal quantum numbers n and n' is given by

$$E_{bb} = R_y \left(\frac{1}{n^2} - \frac{1}{n'^2} \right) , \tag{3.34}$$

where R_y is Rydberg constant (= 13.6 eV). For heavy elements, E_{bb} roughly becomes

$$E_{bb} \sim Z^2 R_y \left(\frac{1}{n^2} - \frac{1}{n'^2} \right) . \tag{3.35}$$

These H-like transitions are named as "Lyman series" after its discoverer, Theodore Lyman. The transitions are named sequentially by Greek letters: transition of $1s$–$2p$ is Lyα (H-like Kα), $1s$–$3p$ is Lyβ (H-like Kβ), $1s$–$4p$ is Lyγ (H-like Kγ), and so on, where s and p mean azimuthal (orbital angular momentum) quantum numbers (l) are 0 and 1, respectively. The line energies of Lyman series of major elements are listed in table 3.1.

If the ions have two or more electrons, the transition process becomes relatively complicated. For example, He-like ions (which have two electrons) emit three most intense lines: resonance ($1s^2$ ^{1}S$_0$ – $1s2p$ ^{1}P$_1$), forbidden ($1s^2$ ^{1}S$_0$ – $1s2s$ ^{3}S$_1$), and inter-combination ($1s^2$ ^{1}S$_0$ – $1s2p$ ^{3}S$_{2,1}$)

Table 3.1:: K-shell emission line energies of H-like and He-like ions.

Element	Line energy (eV)							
	H-like ion			He-like ion*				
	Lyα	Lyβ	Lyγ	K$\alpha(r)$	K$\alpha(f)$	K$\alpha(i)$	Kβ	Kγ
C	367	436	459	308	299	304	355	371
N	500	593	625	431	420	426	498	522
O	654	774	817	574	561	569	666	698
Ne	1022	1211	1277	921	905	914	1073	1127
Mg	1472	1745	1840	1352	1330	1343	1579	1660
Si	2006	2377	2506	1865	1840	1854	2183	2294
S	2623	3107	3277	2461	2431	2447	2884	3033
Ar	3323	3936	4151	3140	3104	3124	3685	3875
Ca	4106	4864	5130	3908	3845	3892	4582	4819
Fe	6966	8266	8732	6702	6641	6670	7798	8217

*r, f, and i indicate resonance, forbidden, and inter-combination lines.

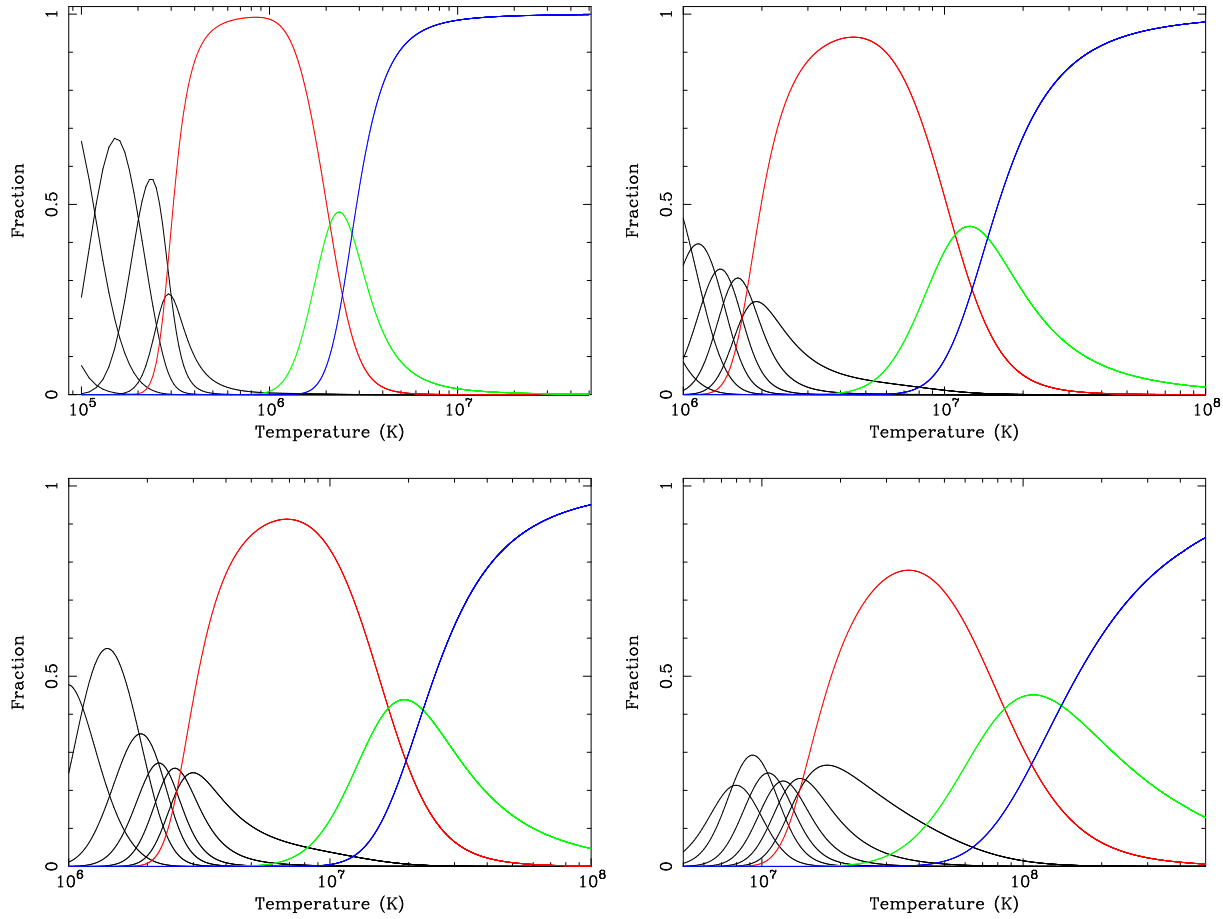

Fig. 3.7.—: Ion fractions of O (top-left), Si (top-right), S (bottom-left), and Fe (bottom-right) as a function of temperature. Plasma condition is assumed to be in collisional ionization equilibrium (CIE) state. In each panel, red, green, and blue, represent He-like, H-like, fully ionized ions, respectively. Black represent ions whose ionization state is lower than He-like.

transition lines. The relative intensities of the these lines depend on the temperature because the collisional excitation rates have not the same dependence with temperature among the three lines. The line energies of He-like ions are listed in table 3.1. Those of He-Kβ ($1s^2$–$1s3p$) and He-Kγ ($1s^2$–$1s4p$) are also listed.

The ionization states depend on the electron temperature. Figure 3.7 shows the ion fractions of O, Si, S, and Fe as a function of temperature, assuming that the plasma reaches collisional ionization equilibrium (CIE) condition (see subsection 3.4.2). When the ionization states are lower than the He-like, the energies of emission lines become lower than those of He-like ion.

Ionized thin-thermal plasma are collisionally excited by free electrons. Since the lifetime of the excited states are much shorter than the average timescale of collision between the electrons and ions, we can assume that the rate of photon emission is the same as that of excitation. Therefore, the line intensity is proportional to $n_e n_i$, which determines the probability of collisions between electrons and ions (n_i is the ion density). We can hence derive relative abundances by comparing line intensities from different elements. Moreover, if the plasma is dominated by hydrogen, the intensity of bremsstrahlung is proportional to $n_e n_{\rm H}$, and hence we can derive absolute abundances (with respect to H) by comparing the intensities of the line and continuum.

3.4 Non-Equilibrium State

3.4.1 Thermal Non-Equilibrium

The hot gas in SNRs is heated by "collisionless shocks", generally propagating in extremely low density ($\lesssim 1$ cm^{-3}), where the shock transition occurs on a length scale much shorter than the typical particle mean free path to Coulomb collisions (Laming 2000). It is suggested that the collisionless shock of young SNRs do not produce electron-ion temperature equilibration. According to equation 3.26, the temperature in the downstream plasma for each particle species a is

$$kT_a = \frac{3}{16} m_a v_s^2 \ , \tag{3.36}$$

with m_a the particle mass, v_s the shock velocity. Therefore, in the limit of true collisionless plasma, the particles will have temperature proportional to their masses: protons will have a temperature $m_{\rm H}/m_e \sim 1800$ times that of the electrons. In realistic conditions, Coulomb equilibration will take place, with rate

$$\frac{d\Delta T}{dn_e t} = -0.13 \frac{Z^2}{A} \frac{\Delta T}{T_e^{3/2}}, \tag{3.37}$$

where $\Delta T = T_i - T_e$, and Z and A are respectively charge and atomic mass of the ions (e.g., Spitzer 1962; Laming 2001). Assuming $T_i > T_e$, we can integrate equation 3.37 to get

$$T_e = \left(\frac{5}{2} \times 0.13 \frac{Z^2}{A} \frac{T_i n_e t}{Z+1} \right)^{2/5} \ . \tag{3.38}$$

In the case that the ions are hydrogen atoms ($Z = A = 1$), we obtain

$$kT_{\rm H} = 2.4 \times 10^{11} \left(\frac{n_e t}{1 \text{ cm}^{-3} \text{ s}} \right)^{-1} \left(\frac{kT_e}{1 \text{ keV}} \right) \text{ [keV]} . \tag{3.39}$$

Therefore, timescale ($t_{\rm eq}$) for electrons and protons to reach equilibrium (energy equipartition) is roughly estimated to be $t_{\rm eq} \sim 10^{11} n_e^{-1}$ s. This corresponds to a few or ten thousand years in a plasma of $n_e = 1$ cm^{-3}.

Although the heating process in collisionless shocks is not well understood, a circumstantial evidences for the non-equilibration have been obtained by the observations of young SNRs, such as Cas A, Tycho, and SN 1006: there are no object whose electron temperature exceeds 5 keV, whereas a typical shock velocity of $\sim$ 2000–5000 km s^{-1} should give rise to a mean plasma temperature of $\gtrsim 10$ keV (e.g., Hughes et al. 2000b). Ion temperature can be measured from the line broadening due to thermal Doppler effect. However, this measurement is very difficult using present X-ray detectors because of their poor energy resolution. In future, ion temperature of thermal plasma in young SNRs will be able to be measured with micro-calorimeter on board NeXT satellite, whose energy resolution will be ~ 5 eV (FWHM) in whole X-ray band.

3.4.2 Non-Equilibrium Ionization (NEI)

After the shock heating, the initial ionization state of the shocked material is considered to be nearly neutral. The ions are gradually losing electrons one-by-one through collisions with free electrons until their ionization states are in equilibrium with the thermal electrons (CIE condition).

The characteristic timescale for a plasma to reach CIE was derived by Masai (1984; 1994). The collisional ionization rate equation for an element of atomic number Z is written as,

$$\frac{df_z}{d(n_e t)} = S_{z-1} f_{z-1} + (S_z + \alpha_z) f_z + \alpha_{z+1} f_{z+1} \tag{3.40}$$

$$\sum_{z=0}^{Z} f_z = 1 \quad (z = 0, 1, ..., Z) , \tag{3.41}$$

where f_z is the ionization fraction of the element which is ionized $(z-1)$ times, and S_z and α_z respectively represent the ionization and recombination rate coefficients for the z-th ionized ion. In the CIE condition, $df_z/d(n_e t) = 0$. Therefore, the timescale ($t_{\rm ion}$) to reach the CIE is estimated with the zero-th order approximation to be,

$$\begin{aligned} n_e t_{\rm ion} &\approx \sum_{z=0}^{Z} (S_z + \alpha_z)^{-1} \\ &\approx [(S_z + \alpha_z)_{\min|S_z - \alpha_z|}]^{-1} \\ &\approx 10^{12} \text{ [cm}^{-3} \text{ s]} , \end{aligned} \tag{3.42}$$

where $(S_z + \alpha_z)_{\min|S_z - \alpha_z|}$ is the absolute value of the diagonal element that gives the minimum difference between S_z and α_z (Masai 1993). The timescale is nearly independent of Z and T_e, but

depends only on n_e. Therefore, "ionization age" (or "ionization parameter") is defined as $\tau = n_e t$, which is often used as a key diagnostic of the non-equilibrium ionization (NEI) state. As given by equation 3.42, τ is typically required to be $\geq 10^{12}$ cm^{-3} s for full ionization equilibrium. Therefore, plasmas in most of young SNRs are in the NEI condition.

3.5 Cosmic-Ray and Non-Thermal Emission

Cosmic-rays are particles with very high energy up to 10^{20} eV. The energy density of cosmic-rays (~ 1 eV cm^{-3}) is larger than those of starlight, Galactic magnetic field and cosmic micro-wave background. Since the discovery of cosmic-rays (Hess 1912), the origin and mechanism of the acceleration have been one of the biggest long-standing problems.

As shown in figure 3.8, the spectrum of cosmic-rays shows a single power-law up to the knee energy ($\sim 10^{15.5}$ eV), where the gyro radius of electrons in the typical interstellar magnetic field is much smaller than the galactic radius. Therefore, cosmic-rays below the knee energy are likely to be of galactic origin. The discoveries of synchrotron X-rays from SN 1006 have indicated that electrons are accelerated close to the knee energy (Koyama et al. 1995). Besides SN 1006, synchrotron X-ray emissions were discovered from other SNRs: e.g., RX J1713.7.3946 (Koyama et al. 1997; Slane et al. 1997), Cas A (Vink et al. 2000a; Hughes et al. 2000a), and Tycho's SNR (Hwang et al. 2002).

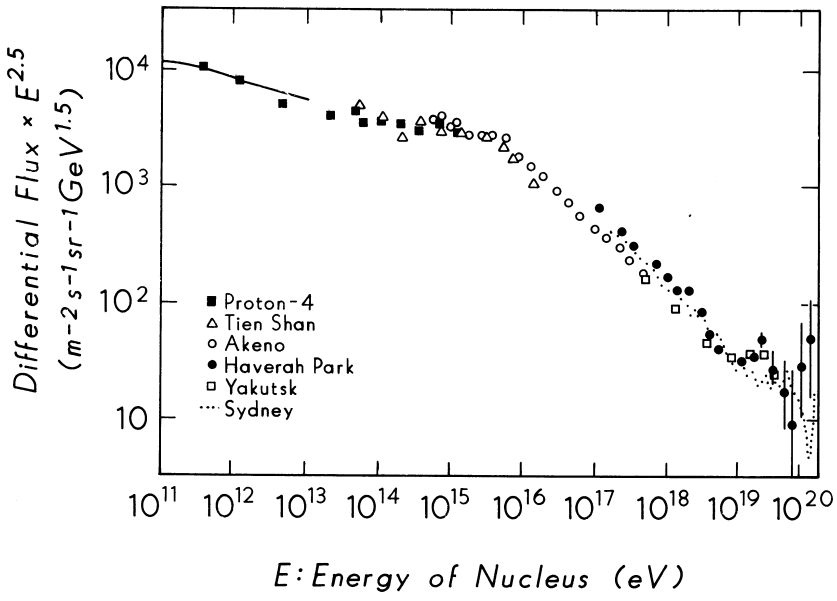

FIGURE 2.2 Differential cosmic ray flux.

Fig. 3.8.—: Energy spectrum of cosmic protons (Sokolsky 1989). The vertical axis is written in differential flux times $E^{2.5}$.

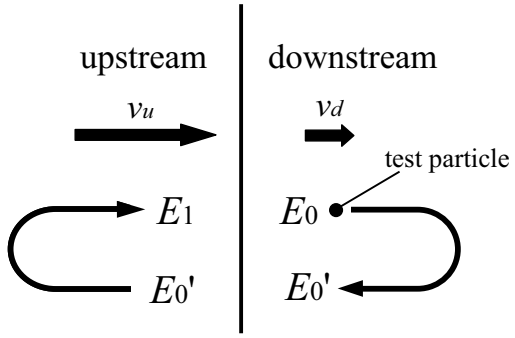

Fig. 3.9.—: A schematic view of first order Fermi acceleration.

Recently, a significant number of SNRs with synchrotron X-rays (called "non-thermal SNRs") have been discovered in Galactic plane (e.g., Ueno 2005). These discoveries provide good evidence for the cosmic-ray acceleration at the shocked shell of SNRs.

In this section, we explain the mechanism of shock acceleration performed at the SNR rims and synchrotron emission from accelerated electrons.

3.5.1 Fermi Acceleration

The most plausible process of the cosmic-ray acceleration is first order Fermi acceleration (Bell 1978; Blandford & Ostriker 1978), which takes place at shock front of SNRs. Similarly to section 3.2, we define the fluid velocities of upstream and downstream as v_u and v_d ($v_u > v_d$), respectively. Here, we consider a test particle in the shock fluid. (Schematic view is shown in figure 3.9.) The particle scattered back elastically in the downstream changes its energy from E_0 into E_0' as

$$E_0' \simeq \gamma_d^2 (1-\beta_d)^2 E_0 \ , \tag{3.43}$$

where $\gamma_d \equiv \sqrt{1-\beta_d^2}$ and $\beta_d \equiv v_d/c$. c is the light speed. Conversely, the particle energy changes in the upstream by a scattering as

$$E_1 \simeq \gamma_u^2 (1+\beta_u)^2 E_0' \simeq (1-2\beta_d)(1+2\beta_u) E_0 \ , \tag{3.44}$$

where we assume $\gamma_u \simeq 1$, $\gamma_d \simeq 1$, and $\beta_d \ll 1$, $\beta_u \ll 1$, which indicates that the shock speed is non-relativistic. Since β_u is larger than β_d, particles obtain energy from the shock fluid during each round-trip between the two regions. The scattering occur through the interactions between charged particles and the magnetic field, not through Coulomb collisions. In the case of 3-dimension, particles are scattered in various direction, therefore equation 3.44 is somewhat modified. The mean particle energy after n round trips is given as (Bell 1978)

$$E_n = E_0 \cdot \exp\left(\frac{4}{3} n(\beta_u - \beta_d)\right) \ . \tag{3.45}$$

Bell (1978) also calculated the probability ($\equiv \eta_s$) that the scattered particles escape from the acceleration region for each round trip as

$$\eta_s = 4\frac{v_d}{v_p} \ , \tag{3.46}$$

where v_p is a particle velocity. Hence the probability that a particle makes n round trips is given as

$$P_n = (1-\eta_s)^n = (1-4\beta_d)^n \ , \tag{3.47}$$

where we assumed $v_p = c$ (particle is relativistic). Using the equation 3.47, we can calculate the differential energy spectrum of accelerated particles as

$$N(E) \propto \frac{dP_n}{dE_n} \propto E^{-\frac{\beta_u+2\beta_d}{\beta_u-\beta_d}} . \tag{3.48}$$

In the case of $\beta_d = \frac{1}{4}\beta_u$ (equation 3.16 for $\gamma = 5/3$), we obtain an equation of

$$N(E) \propto E^{-2} \ . \tag{3.49}$$

3.5.2 Synchrotron Emission

Charged particles emit synchrotron radiation in magnetic field. The synchrotron radiation power per unit frequency from a single electron of energy E in a magnetic field B is given as (Rybicki & Lightman 1979)

$$P(\omega,\alpha) = \frac{\sqrt{3}}{2\pi}\frac{\mathrm{e}^3 B\sin\alpha}{m_\mathrm{e}c^2} F\left(\frac{\omega}{\omega_c}\right) \ , \tag{3.50}$$

where α and $F(x)$ are respectively the pitch angle and the function given by Rybicki & Lightman (1979). The peak frequency ω_c is

$$\omega_c = \frac{3\gamma^2 \mathrm{e} B\sin\alpha}{2m_e c} \ . \tag{3.51}$$

Note that protons radiate little synchrotron radiation since they are as 1800 times heavy as electrons. Integrating over ω, we found that total emission power is written as

$$P_\mathrm{sync} = \frac{4}{3}\sigma_T c\beta^2\gamma^2 U_B \ . \tag{3.52}$$

Here $\sigma_T = 8\pi r_0^2/3$ is the Thomson cross section, and U_B ($= B^2/8\pi$) is the magnetic field energy density.

Assume that the number density of electrons is represented by a power-law distribution expressed in the form

$$N(E)dE = CE^{-p}dE \ , \tag{3.53}$$

or

$$N(\gamma)d\gamma = C\gamma^{-p}d\gamma \ . \tag{3.54}$$

The quantity C can vary with pitch angle and the like. Then, the total power radiated per unit volume and unit frequency is given by the integral of $N(\gamma)d\gamma$ times the single particle radiation formula over all energies or γ. Thus, we have

$$P_{\rm tot}(\omega) = C \int P(\omega)\gamma^{-p} d\gamma \ \propto \int F\left(\frac{\omega}{\omega_c}\right)\gamma^{-p} d\gamma \ . \tag{3.55}$$

Let us change variables of integration to $x \equiv \omega/\omega_c$, noting $\omega_c \propto \gamma^2$;

$$P_{\rm tot}(\omega) \propto \omega^{-(p-1)/2} \int F(x) x^{(p-3)/2} dx \ . \tag{3.56}$$

The integral of this equation becomes constant, then we have

$$P_{\rm tot}(\omega) \propto \omega^{-(p-1)/2} \ , \tag{3.57}$$

so that the spectral index of synchrotron radiation (s) is related to the particle distribution index p by

$$s = \frac{p-1}{2} \ . \tag{3.58}$$

Therefore, power-law emission is an indicator of synchrotron emission, namely accelerated electrons. In the case of first order Fermi acceleration which gives an energy/ index of electron to be $p \sim 2$ (equation 3.49), the spectrum index of the synchrotron emission is 0.5 (photon index = 1.5). This value is almost consistent with the canonical value of the non-thermal radio spectrum from SNR shell.

Chapter 4

Instruments

4.1 Overview of Suzaku

Suzaku (Mitsuda et al. 2007) is the fifth Japanese X-ray astronomy satellites, developed by a Japanese–US collaboration. It was launched from Uchinoura Space Center (USC) on 10 Jury 2005, and successfully put into a near-circular orbit at ∼570 km altitude with an inclination angle of 31°. Figure 4.1 shows a schematic of view of Suzaku in orbit. The spacecraft length is 6.5 m along the telescope axis after deployment of the extensible optical bench (EOB).

Suzaku carries three scientific detector systems: Hard X-ray Detector (HXD: Takahashi et al. 2007), X-ray Imaging Spectrometer (XIS: Koyama et al. 2007), and X-ray Spectrometer (XRS:

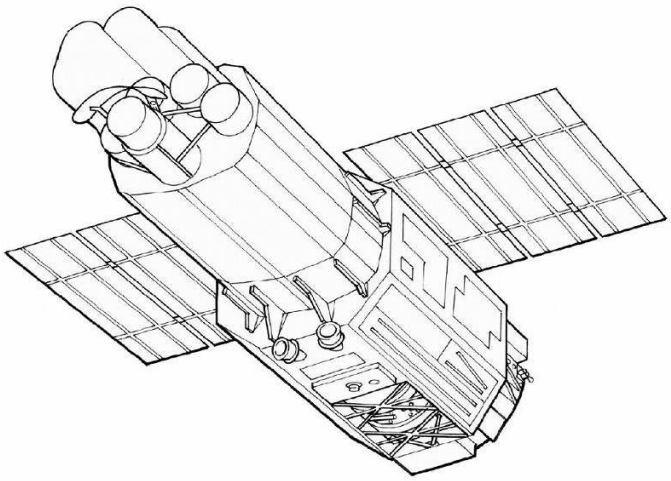

Fig. 4.1.—: Schematic view of the Suzaku satellite in orbit. On the top, the X-ray telescopes (XRT) can be seen. This picture is taken from Mitsuda et al. (2007)

Kelley et al. 2007). The XIS and XRS are placed in the focal plane of X-Ray Telescope (XRT: Serlemitsos et al. 2007). The configuration of the systems are shown in Figure 4.2, where XRT-I and XRT-S are telescopes for the XIS and XRS, respectively.

Although the XRS, one of the main instruments of Suzaku, became not operational because of liquid helium loss, all the other detectors are still working properly. Therefore, Suzaku retains its excellent X-ray sensitivity in a wide-energy range of 0.2–600 keV, with moderate energy resolution and a low background level. We show in following sections the characteristics of each operating instrument.

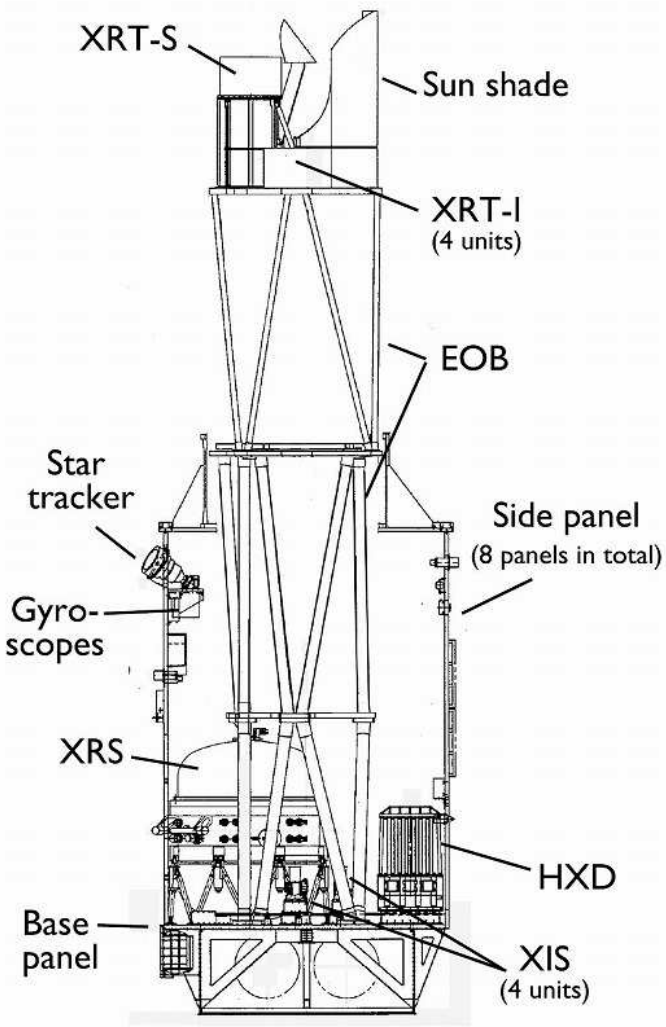

Fig. 4.2.—: Side view of Suzaku with the internal structures after the extensible optical bench deployment. This picture is taken from Mitsuda et al. (2007).

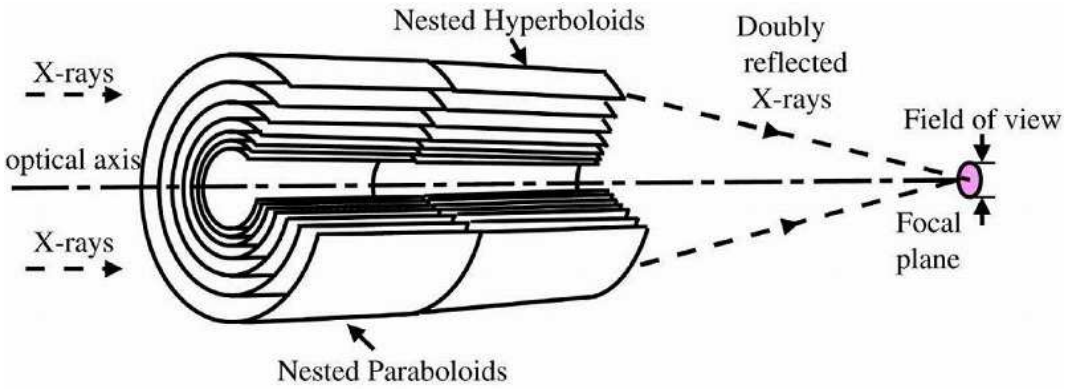

Fig. 4.3.—: Wolter type I reflecting optics.

4.2 XRT

Five sets of the XRT were developed jointly by NASA/GSFC, Nagoya University, Tokyo Metropolitan University, and ISAS/JAXA. One of them is equipped for the XRS (called XRT-S), and the others are equipped for the XIS (XRT-I). Since the XRT-S is no more functional, hereafter the XRT-I is called simply "XRT". All of the four XRT are co-aligned to image the same region of the sky.

Telescope Design

The XRT is configured to form a Wolter type I grazing-incidence reflective optics (figure 4.3). Incident X-rays are reflected twice by parabolic surface and hyperbolic surface, and are condensed to the focal plane, when their incident angle is less than a certain value (see table 4.1). Since the projected area per reflector is very small, the mirrors are formed by a large number of thin-foils in order to enlarge the effective area. The design parameters and basic performance of the XRT are summarized in table 4.1.

Characteristics

The left panel of figure 4.4 shows the energy dependence of the total on-axis effective area of the four XRT, including the detector efficiency, compared with those of other X-ray missions. The XRT provide a large efficiency with a moderate imaging capability in the energy range of 0.2–12 keV. The effective area of the four XRT modules is much larger than that of Chandra in almost whole energy band, and comparable to that of XMM-Newton above $\sim$5 keV. As shown in the right panel of figure 4.4, The effective area also depends on the off-axis angle, because the reflection coefficient decreases with increasing the X-ray incident angle. This dependence is called "vignetting", calculated by the ray-tracing simulator (Ishisaki et al. 2007), and confirmed in the

Table 4.1:: Design parameters and performance of the XRT (Serlemitsos et al. 2007).

Focal length	4.75 m
Substrate	Al (152μm)
Reflector	Au (>0.1 μm)
Number of nesting	175
Inner / outer diameter	118 mm / 399 mm
Incident angle	0.°18–0.°60
Geometrical area	873 cm^2
Field of view*	20′ (@ 1 keV) / 14′ (@ 7 keV)
Effective area	450 cm^2 (@ 1.5 keV) / 250 cm^2 (@ 7 keV)
Half Power diameter	2.′0

* Diameter of the area within which the effective area is more than 50% of the on-axis value.

orbit by the observations of the Crab Nebula (Serlemitsos et al. 2007).

Since the angular resolution of the XRT is limited, the image of a point source becomes blurred on its focus. The Point-Spread Function (PSF) and Encircle-Energy Fraction (EEF) are shown in left and right panel of figure 4.5, respectively. The half power diameter (HPD), defined as the diameter within which the X-ray flux is 50% of the total flux of a point source, is ∼2 arcmin for each XRT. This value is significantly improved from ASCA (∼ 3.′6).

The response of the XRT is described by Ancillary Response Files (ARFs). In all spectral analyses described in following chapters, we use ARFs generated utilizing `xissimarfgen` software (Ishisaki et al. 2007).

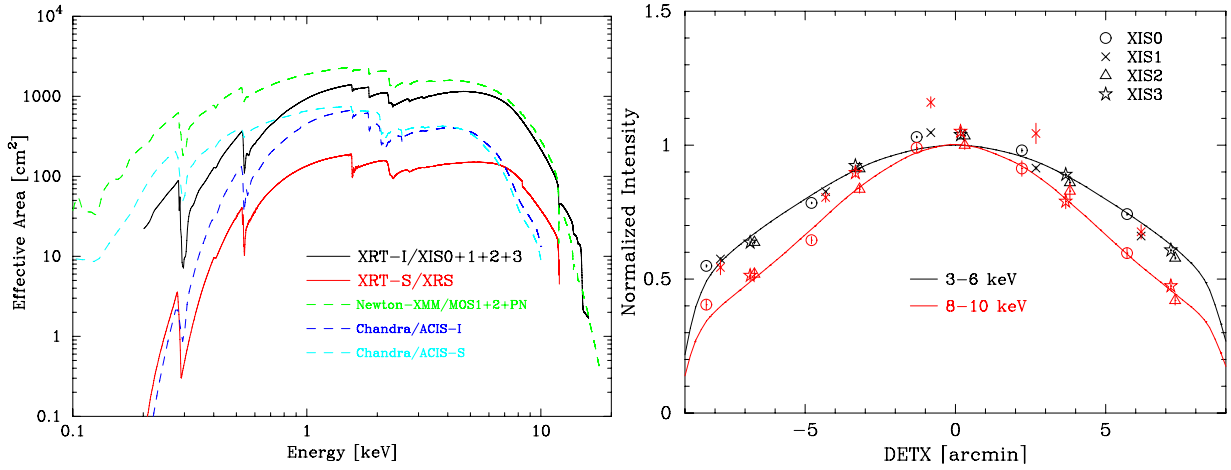

Fig. 4.4.—: Left: Total effective area of the four XRT modules compared with that of XMM-Newton and Chandra. Right: Vignetting of the XRT using the data of the Crab Nebula. The model curves were calculated with the ray-tracing simulator. The left and right figures are taken from Mitsuda et al. (2007) and Serlemitsos et al. (2007), respectively.

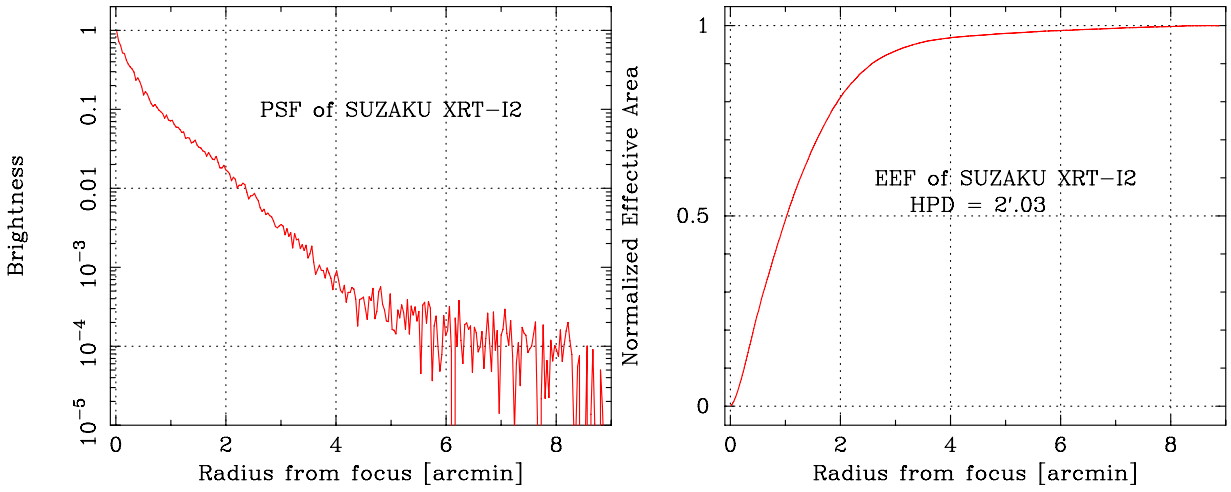

Fig. 4.5.—: Point-Spread Function (PSF) and Encircle-Energy Fraction (EEF) of the XRT (for XIS2) in the focal plane. Both figures are taken from Serlemitsos et al. (2007).

4.3 XIS

Four sensors of the XIS were developed by the collaboration of Kyoto University, Osaka University, ISAS/JAXA, Massachusetts Institute of Technology (MIT), Rikkyo University, and RIKEN (The Institute of Physical and Chemical Research). The XIS employs X-ray sensitive silicon charge-coupled devices (CCD), similar to that used in the ASCA SIS, Chandra ACIS, and XMM-Newton EPIC. Coupled with the XRT, the XIS have imaging capability in the energy range of 0.2–12 keV. The photograph and schematic view of the XIS sensor (CCD+camera body) are shown in figure 4.6.

4.3.1 Overview

Specifications of the CCD

The CCD chip has an imaging area of 1024×1024 pixels and two frame-store regions of 512×1024 pixels, as shown in figure 4.7. The pixel size of the imaging area is 24 μm × 24 μm, while that of the frame-store regions is 21 μm × 13.5 μm. The CCD has four readout nodes (Node

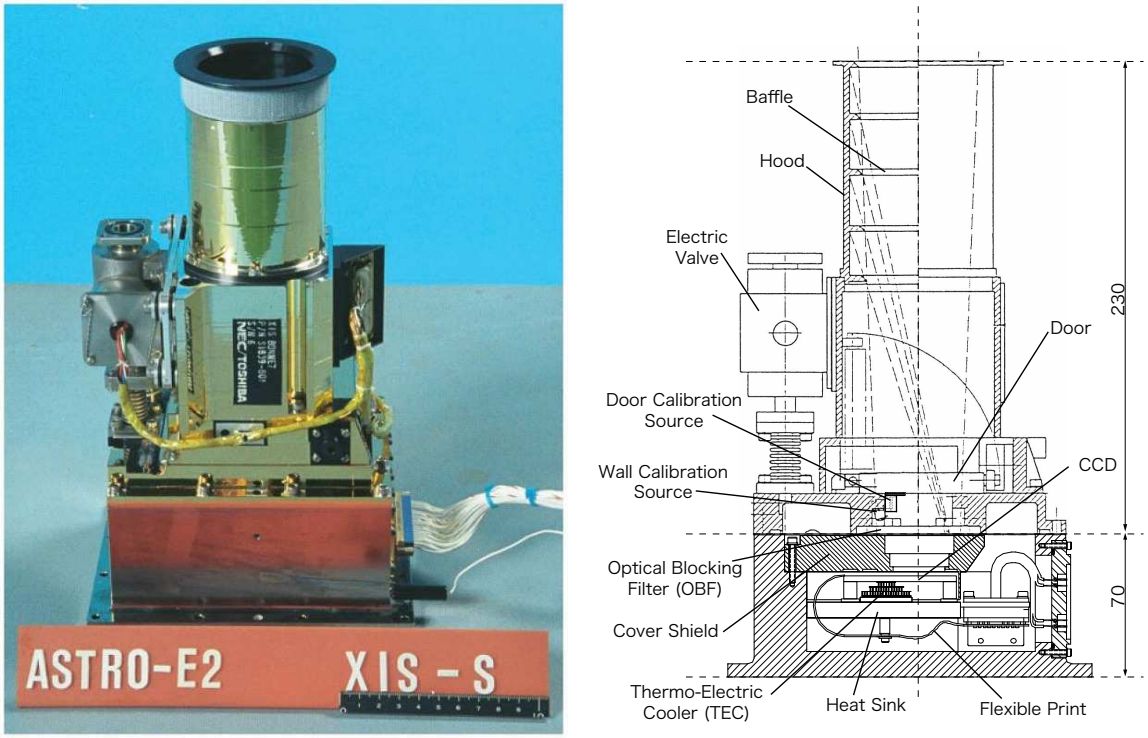

Fig. 4.6.—: The picture (left) and schematic view (right) of XIS sensor. Both pictures are taken from Koyama et al. (2007).

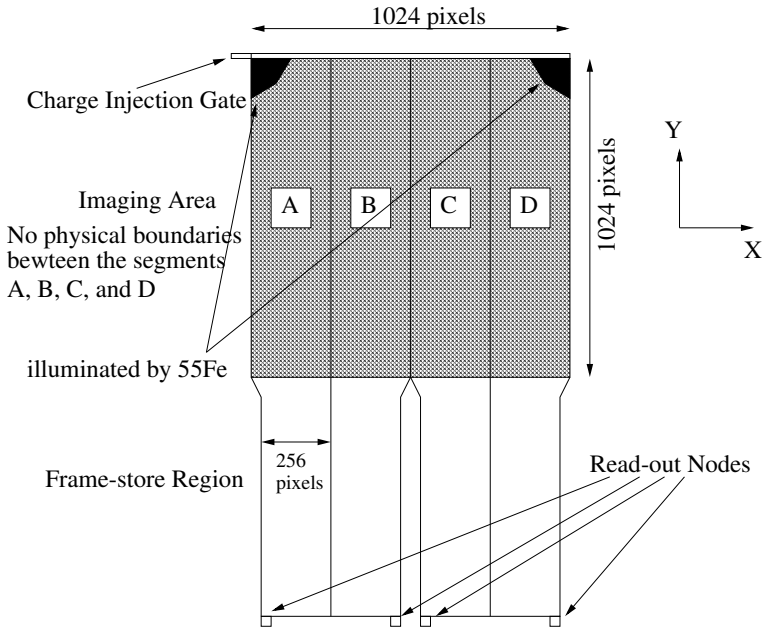

Fig. 4.7.—: Schematic view of CCD chip. The CCD consists of four segments (A, B, C, and D), each with a dedicated read-out node.

A–D) and each node reads the signals from 256 columns of the chip. Therefore the CCD is divided to four segments (Segment A–D). Photoelectrons generated in the imaging area are simultaneously transfered to the frame-store regions, and read by the nodes in order. The time required to transfer one pixel is $\sim$0.25 μs. The CCD chip is cooled to –90 °C by the Thermo-Electric Cooler (TEC) which is controlled by the Thermal Controller Electronics (TCE). For on-orbit calibration, each sensor has ^{55}Fe calibration sources. Two sources are located on the side wall of the housing and illuminate two corners (top of the Segment A and D) of the imaging area. Since the CCD is sensitive to optical and UV light, the XIS have optical blocking filters (OBF), made of aluminum and polyimide film, 20 mm above the imaging area (see the right panel of figure 4.6). The OBF has a low transmission coefficient for optical light ($\leq 5 \times 10^{-5}$), but is transparent to X-rays ($\geq$80%

Table 4.2:: Design parameters and performance of the XIS (Koyama et al. 2007).

Field of view	$18' \times 18'$
Energy range	0.2–12 keV
Format	1024×1024 pixels
Energy resolution	$\sim$130 eV (FWHM; @ 5.9 keV)
Readout noise	$\sim$2.5 electrons
Time resolution	8 s (normal) / 7.8 ms (P-sum)

above 0.7 keV).

The design parameters are summarized in table 4.2. Note that the XIS has two CCD clocking modes: normal mode and parallel-sum (P-sum) mode. Normal mode has imaging capability with time resolution of 8 sec. On the other hand, P-sum mode has good time resolution (7.8 msec), but it has no imaging capability. During all observations described in this thesis, the XIS were operated in the normal clocking mode.

Event Detection

When an X-ray photon is absorbed in a depletion layer of the CCD chip, it produces a charge cloud typically smaller than the pixel size of the CCD. Thus the charge does not occupy more than 2×2 pixels. In contrast, a charged particle excites free electrons along its track, producing a larger (than 2×2 pixels) charge cloud. In order to distinguish X-ray events from charged particle events, we use the Grade method (figure 4.8). An event is recognized when a pixel has a pulse-height (PH) between the lower and upper thresholds and the PH is a local maximum among adjacent pixels. Then the surrounding 3×3 pixels are compared to the split threshold, and the event is classified into the Grades given in figure 4.8. We regard the events of Grade 0, 2, 3, 4, and 6 as the X-ray events. On the other hand, all of the events which split over the 2×2 pixels region are classified into Grade 7 and regarded as background events, because they are usually formed by charged particle events.

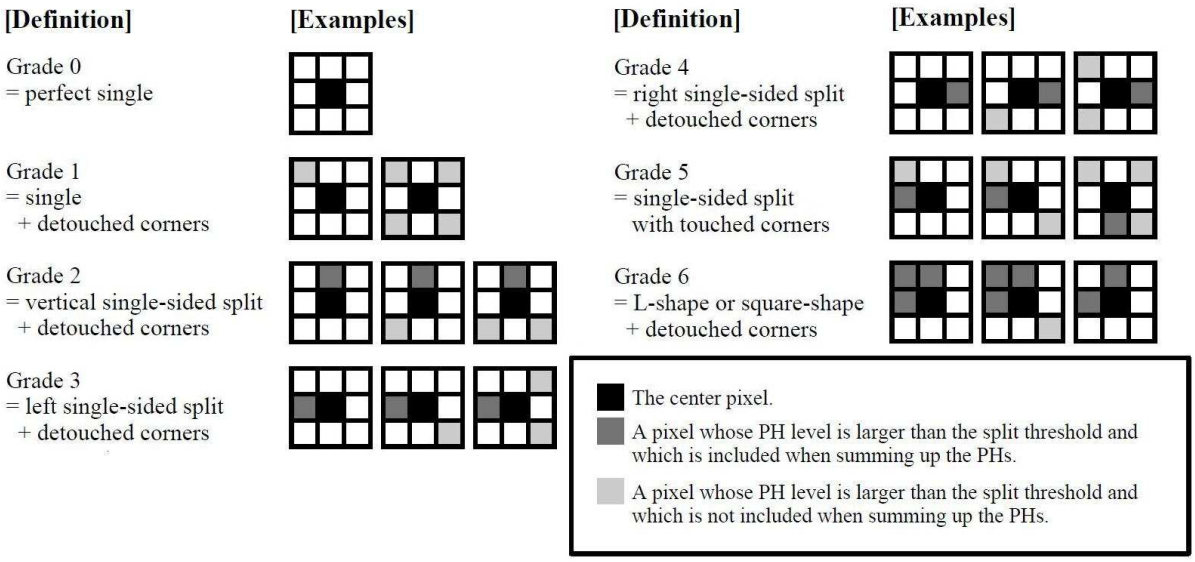

Fig. 4.8.—: Classification of the "Grade". Grade 0, 2, 3, 4, and 6 are regarded as X-ray events. "PH" indicates pulse-height which is proportional to the energy of incident X-ray.

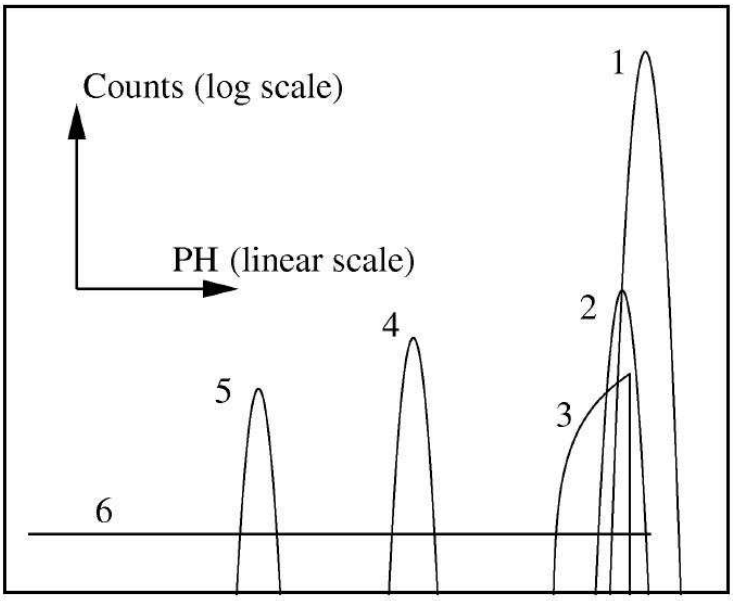

Fig. 4.9.—: Schematic picture of the response function (the XIS response to a monochrome X-ray). It consists of (1) main peak, (2) sub peak, (3) triangle component, (4) Si escape peak, (5) Si fluorescent peak, and (6) constant component. This figure is taken from Matsumoto et al. (2006)

4.3.2 Characteristics and Performances

Response Function

Even if incident X-rays are monochrome, the spectral shape is not a simple Gaussian but is more complicated as is shown schematically in figure 4.9. It consists of (1) main peak, (2) sub peak, (3) triangle component, (4) silicon escape peak, (5) silicon fluorescent peak, and (6) constant component. In the energy range below the Si K-edge (1.839 keV), components (4) and (5) are not seen. The physical interpretations these components are described in Matsumoto et al. (2006). This spectral response to monochrome X-rays is called "response function", which was calibrated by our ground experiments. The response function is included in the response matrix files (RMFs), which can be made using `xisrmfgen` software (Ishisaki et al. 2007).

Quantum Efficiency and Energy Resolution

The XIS consist of three Front-Illuminated (FI) CCDs and one Back-Illuminated (BI) CCD. The left panel of figure 4.10 shows the quantum efficiency (QE) of the FI and BI, which were modeled on the results of our ground calibration. Since the BI has no gate structure obstructing incident X-rays on its surface, it has much higher QE below $\sim$4 keV than the FI. However, the QE of the BI for hard X-rays is lower than that of the FIs, because the depletion layer of the BI is

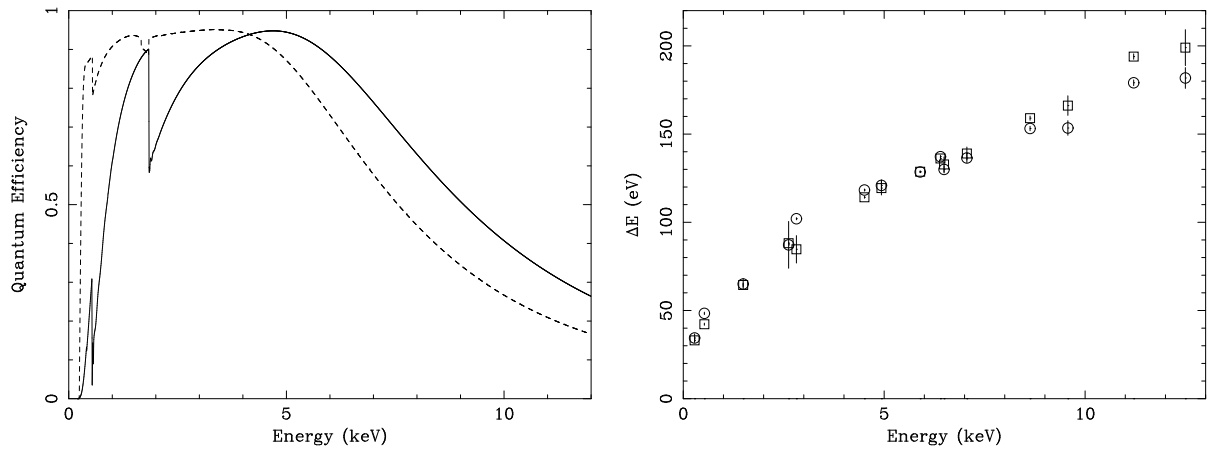

Fig. 4.10.—: Left: Quantum efficiency of the FI CCD (solid line) and the BI CCD (dash line), which were modeled based on the results of the ground calibration. Right: Energy resolution of the FI CCD (square) and the BI CCD (circle), which were also the results of the ground calibration.

thinner than that of the FIs (~ 75 μm and ~ 45 μm for the FI and BI, respectively). The energy resolution is comparable between the FI and BI, as shown in the right panel of figure 4.10. Both achieve a pre-flight energy resolution of $\sim$130 eV (FHWM of the main peak component) at 5.9 keV.

Non X-Ray Background

Figure 4.11 shows non X-ray background (NXB) spectra of the XIS and EPIC on board XMM-Newton, normalized by their solid angle of the field of view (FOV) and by their effective area. It hence represents surface brightness of the background, and gives a measure of the S/N ratio for diffuse objects. The NXB spectra of the XIS and EPIC are respectively extracted from the night Earth data and "CLOSED" data (taken with the filter wheel in the closed position). The background level of the EPIC-MOS is $\sim$5 times higher than that of the XIS-FI and is comparable to that of the XIS-BI above $\sim$6 keV, where the NXB is dominant in the background spectra. Although the background continuum level of the EPIC-pn is lower than that of EPIC-MOS, the NXB spectrum of the EPIC-pn has very strong emission lines (Ni, Cu, and Zn) above 7 keV. The intensity of Al-Kα line at 1.49 keV in the XIS spectra is also much weaker than that in the EPIC spectra. Therefore, it is proved that the XIS-FI has the lowest background level (the highest S/N ratio) for diffuse objects. Furthermore, the EPIC NXB frequently shows "background flare", and the NXB count rate varies by a factor of about 100. Since the orbit altitude of Suzaku is much lower than XMM-Newton and Chandra, Suzaku is less influenced by solar flares, and hence the background level of the XIS is very stable. Therefore, the XIS is very sensitive to diffuse dim sources especially in the hard X-ray band. The details of the XIS background properties can be found in Yamaguchi et al. (2006) and Tawa et al. (2008).

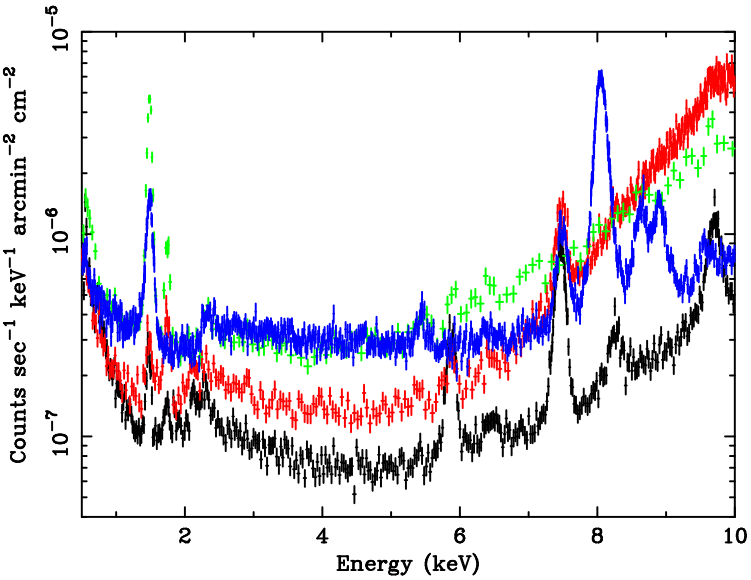

Fig. 4.11.—: Comparison of the NXB spectra normalized by the solid angle of the FOV and by the effective area between the Suzaku XIS and the XMM-Newton EPIC. The black, red, green, and blue represent the XIS-FI, XIS-BI, EPIC-MOS, and EPIC-pn, respectively.

Degradation of Performances

Since the launch, the energy resolution of the XIS is gradually degrading due to the radiation damage (Koyama et al. 2007). Figure 4.12 shows the on-orbit time histories of the energy resolution at 5.9 keV. The apparent linear trend (∼50 eV/yr) is due to charge loss caused by increasing of charge transfer inefficiency (CTI). The details of the CTI are described in Nakajima et al. (2008). The calibration results on the degradation of the energy resolution are reflected to the RMF (Ishisaki et al. 2007).

The low energy QE had been degraded by the contamination (due to out-gassing from the satellite) lied on the OBF (Koyama et al. 2007). The contamination rate is unexpectedly high, and the rate is different from sensor to sensor. Moreover, the thickness of the contamination varies with position on the OBF. We therefore need to include additional, time-varying low energy absorption. This is given as a function of both the observation date after the XIS door-open, and of detector coordinates (specifying the position on the OBF). The time history of the contamination is shown in the left panel of figure 4.13, which is measured by observing the SNR E 0102–72 and the isolated neutron star RX J1856.5–3754. Although the chemical composition for the contamination material is not conclusively determined, it is assumed that the contaminant contains C and O with the number ratio C/O ~ 6, from the overall spectral shape in the low energy absorption for the X-ray sources and the best guess for the out-gassing source in Suzaku. The off-axis absorption is determined utilizing the diffuse X-rays from the day Earth rim. The radial profile of the contamination is shown in the right panel of figure 4.13. These calibration results are reflected to the ARF (Ishisaki

et al. 2007). Note that, however, the calibration accuracy is relatively poor in large off-axis angle ($\gtrsim$ 8 arcmin) region. Furthermore, the calibration for the FI is less accurate than that for the BI (Koyama et al. 2007).

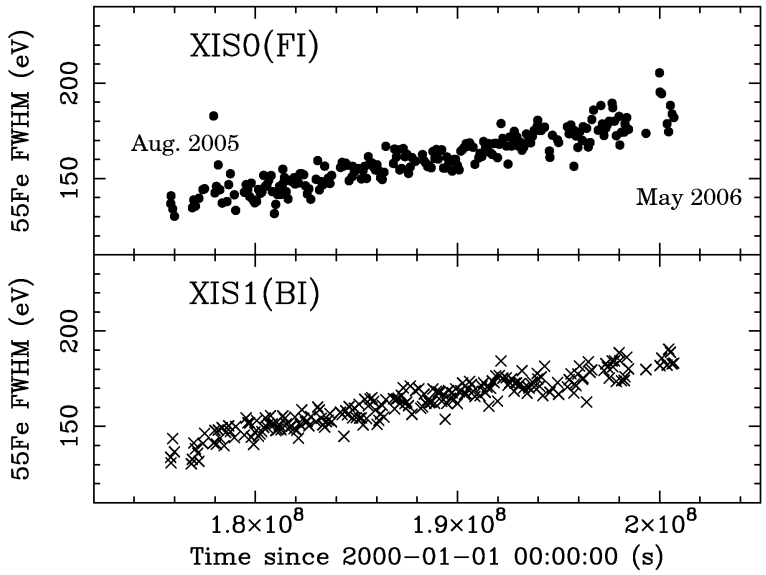

Fig. 4.12.—: Time history of the energy resolution (FWHM) measured with Mn-Kα line (5.9 keV) from the ^{55}Fe calibration sources. Top and bottom indicate the XIS0 and XIS1, respectively. This figure is taken from Koyama et al. (2007).

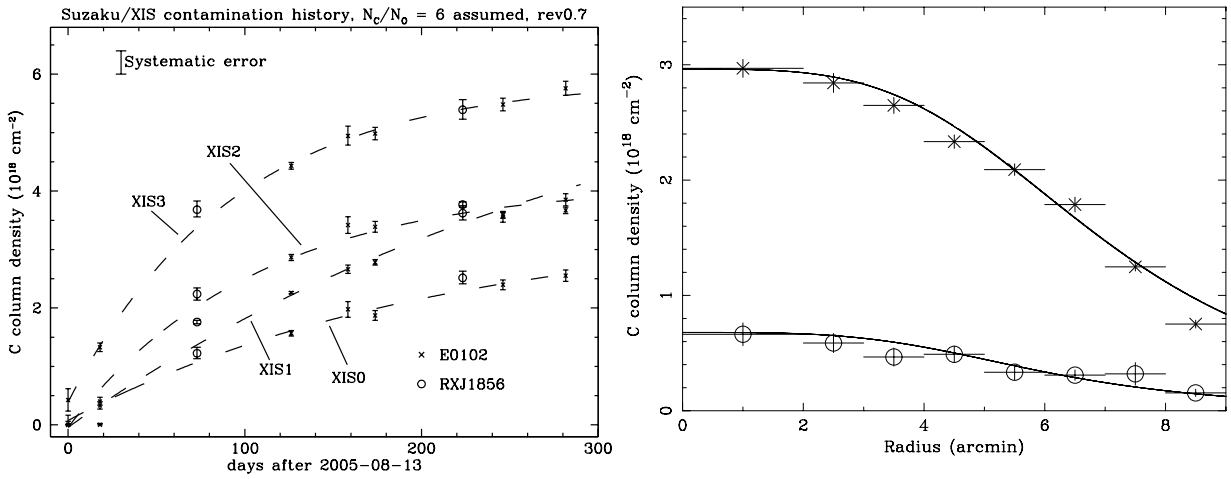

Fig. 4.13.—: Left: The time history of the contamination measured at the center of the OBF. Right: The radial profile of the contamination of the XIS-BI. Circle and cross represent the data for one month and five months after the door-open, respectively. Both figures are taken from Koyama et al. (2007).

4.4 HXD

The HXD was developed by the collaboration of the University of Tokyo, Aoyama Gakuin University, Hiroshima University, ISAS/JAXA, Kanazawa University, Saitama University, Stanford Linear Accelerator Center (SLAC), and RIKEN. It is a non-imaging, collimated hard X-ray scintillating instrument sensitive in the 10–600 keV band. Since the main goal of this thesis is the spectroscopy in the energy band below 10 keV, we do not use the data obtained with the HXD. In this section, therefore, we show only basic characteristics of this instrument.

The HXD sensor is a compound-eye detector instrument (figure 4.14), consisting of 16 main detectors (arranged as a 4×4 array) and the surrounding 20 crystal scintillators for active shielding. Each unit actually consists of two types of detectors: a GSO/BGO phoswich counter, and 2mm-thick PIN silicon diodes located inside the well, but in front of the GSO. The PIN diodes are mainly sensitive below ∼60 keV, while the GSO/BGO scintillator is sensitive above ∼30 keV. The characteristics of the HXD are summarized in table 4.3. The outer anti-coincidence scintillators can be used as a wide-field hard X-ray detector, which is referred as the Wide-band All-sky Monitor (WAM). This can be used to detect bright X-ray transients, γ-ray bursts, and solar flares.

Figure 4.15 shows the background counting rate as a function of energy for the 10–500 keV region. The background rate of the HXD on board Suzaku is the lowest among the existing missions for most X-ray energies. The sensitivity in this energy region is essentially limited by the accuracy of background estimation. At present, the background model for the HXD-PIN can be reproduced with an accuracy of 5% of the background level (Kokubun et al. 2007).

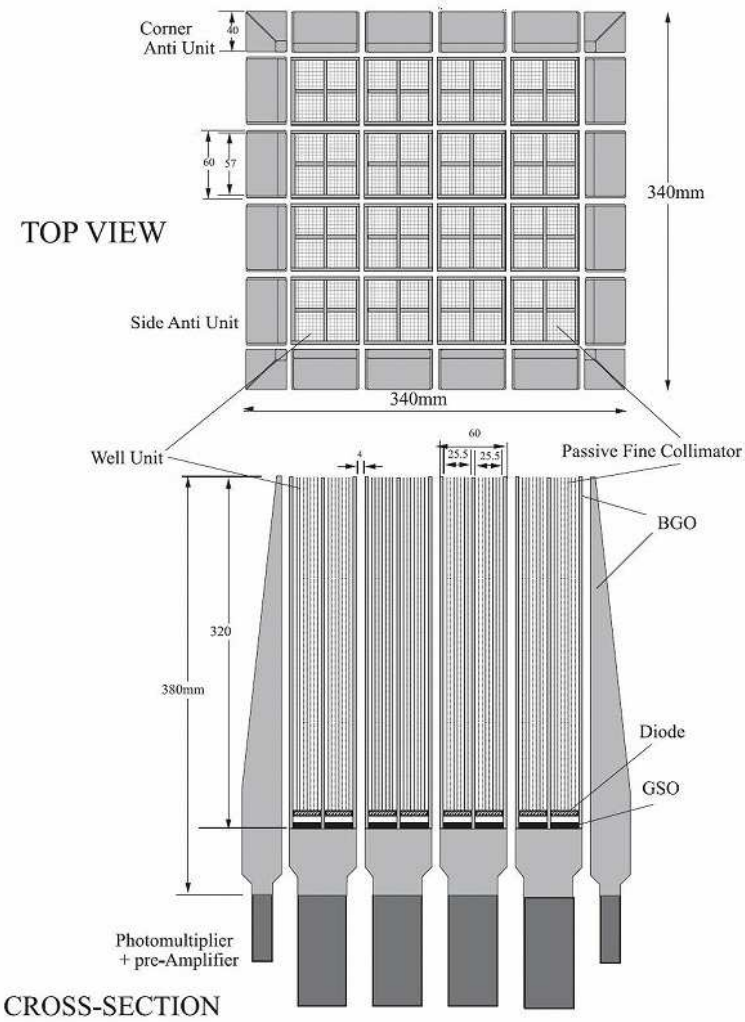

Fig. 4.14.—: Schematic view of HXD. This picture is taken from Takahashi et al. (2007).

Table 4.3:: Performance of the HXD (Takahashi et al. 2007).

Field of view	$4.^\circ5 \times 4.^\circ5$ ($\gtrsim$ 100 keV) / $34' \times 34'$ ($\lesssim$ 100 keV)
Bandpass	10–70 keV (PIN) / 40–600 keV (GSO)
Energy resolution (FWHM)	$\sim$3.0 keV (PIN) / $7.6E_{\rm MeV}^{-1/2}$ % (GSO)
Effective area	$\sim$160 cm^2 (@ 20 keV) / $\sim$260 cm^2 (@ 100 keV)
Time resolution	61 μs or 31 μs

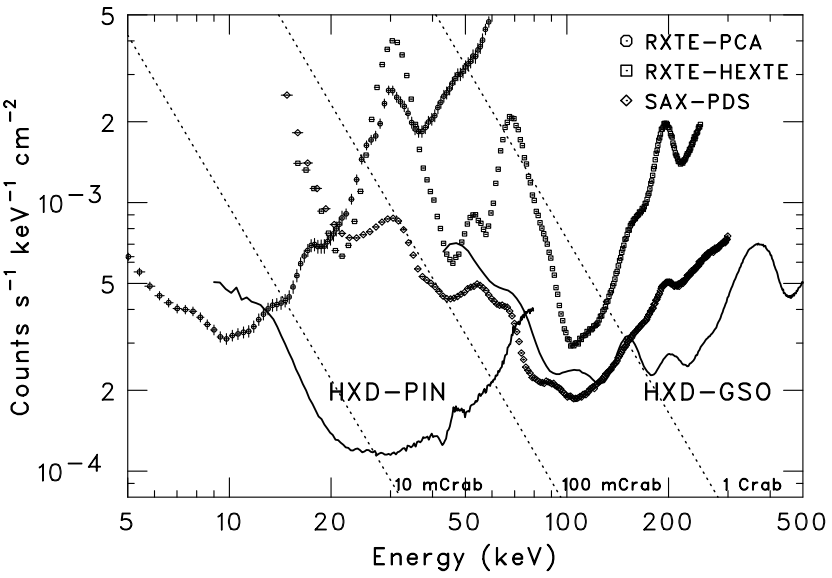

Fig. 4.15.—: In-orbit detector background of the PIN/GSO compared with those of the RXTE and BeppoSAX. The dotted lies indicate 1 Crab, 100 mCrab, and 10 mCrab intensities. This picture is taken from Kokubun et al. (2007).

Chapter 5

SN 1006

SN 1006 is famous as the prototype of non-thermal SNRs, owing to the first discovery of synchrotron X-rays from the shell of the remnant (Koyama et al. 1995). However, its thermal emission from shock heated plasma also has a very important aspect. As explained below, the evolutional state of SN 1006 is probably younger than any other historical Galactic SNRs, due to the extremely low ISM density around SN 1006. Thermal X-ray emission from a young SNR is dominated by the radiation from ejecta, as described in chapter 3. Therefore, a young SNR is well-suited for investigation the abundances of synthesized elements and thermal evolution of the ejecta in a very early phase of SNR evolution. For this reason, we choose the 'youngest' SNR, SN 1006, as the main target of this thesis. We summarize, in this chapter, the results of Suzaku observation and analysis on SN 1006 (mainly following Yamaguchi et al. 2008a). Unless otherwise stated, figures in this chapter are taken from Yamaguchi et al. (2008a).

5.1 Previous Results

SN 1006 (G327.6+14.6) is the remnant of the historical SN explosion on May 1, A.D. 1006, which was observed and recorded in all over the world. The SN was very bright, was compared with the Moon, and remained visible for perhaps several years. The records survive from Japan, China, Korea, Iraq, Syria, Egypt, Italy, Switzerland, France, and possibly Spain. Its remnant was first cataloged by Bolton et al. (1964) as a radio source and identified (as the remnant of SN 1006) by Gardner & Milne (1965). The energy index in radio band is measured by Allen et al. (2001) to be $\alpha = 0.57$. The distance to SN 1006 is determined to be 2.2 kpc by optical observations (Winkler et al. 2003); we assume this value here.

In X-ray band, SN 1006 was first observed by Einstein satellite (Becker et al. 1980). Using ASCA, Koyama et al. (1995) discovered synchrotron X-rays from shells of the SNR, that indicates the existence of high energy electrons up to $\sim$100 TeV. The Chandra results of the small-scale structure have been successfully explained by a diffusive shock acceleration model (DSA); the first-

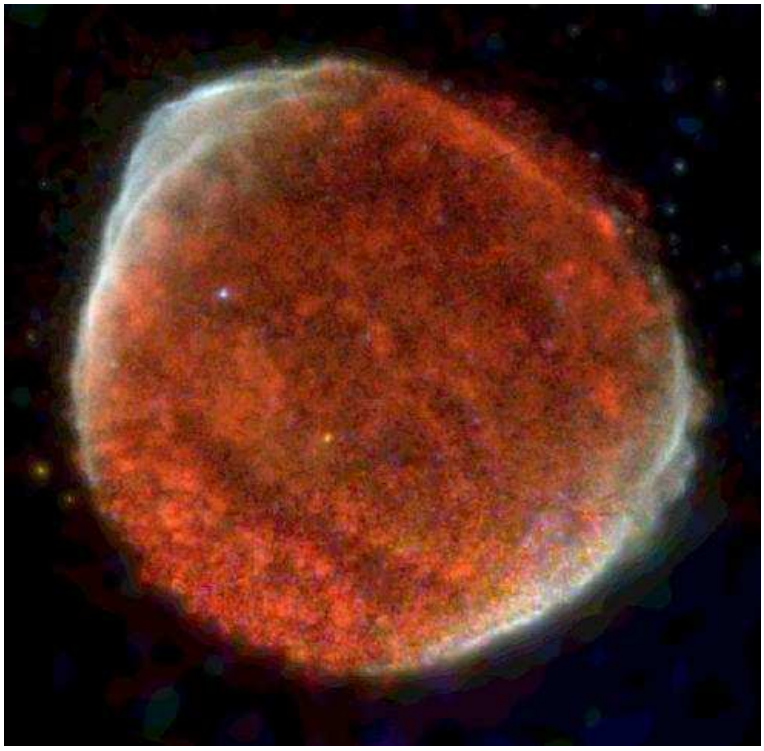

Fig. 5.1.—: XMM-Newton image of SN 1006, taken from Rothenflug et al. (2004). Red, green, and blue are 0.5–0.8 keV, 0.8–2.0 keV, and 2.0–4.5 keV, respectively. The areas dominated by non-thermal emission appear white. North is up and east is to the left.

order Fermi mechanism is working at the shock front of SNRs (Bamba et al. 2003; Yamazaki et al. 2004). Rothenflug et al. (2004) observed whole region of the remnant with XMM-Newton (figure 5.1), and concluded that the anisotropic morphology of the non-thermal emission is due to the ambient magnetic field running southwest to northeast along the Galactic plane. Although the detection of inverse Compton TeV γ-rays with CANGAROO was reported by Tanimori et al. (1998), this result had been denied by HESS observatory (Ksenofontov et al. 2005).

Based on the historical record, SN 1006 is widely regarded to be one of the Galactic type Ia SNRs (Schaefer 1996). As explained in chapter 2, The current SN models predict that Fe production in Type Ia SNe is far larger than that of core-collapse SNe (e.g., Nomoto et al. 1984; Iwamoto et al. 1999). Therefore, measuring the Fe abundance is one of the essential clues to classify the SN type of any specific remnant. The K-shell X-ray emission lines from ionized Fe offer the most direct information for abundance determination. In fact, strong Fe-Kα lines had been observed from Tycho's SNR (e.g., Hwang et al. 1998; Decourchelle et al. 2001) and many of the other Type Ia SNRs.

In SN 1006, Vink et al. (2000b) suggested the possible presence of an Fe-K emission line at 6.3$\pm$0.2 keV from the BeppoSAX MECS spectrum. However, the detection was not clear, because

the energy resolution of the MECS (a gas scintillation counter) was relatively poor (FWHM∼500 eV @6 keV). Other recent X-ray missions, Chandra and XMM-Newton, have not succeeded in detecting an Fe-K line. Cold Fe in the interior of SN 1006 is known to exist based on ultraviolet (UV) absorption studies (e.g., Wu et al. 1993; Hamilton et al. 1997; Winkler et al. 2005). Figure 5.2 indicates the positions of background UV sources (with circle mark) on the Hα image of SN 1006. As shown in figure 5.3, blue and red-shifted Fe II absorption lines were detected in the spectra of the background stars, labeled 'Q2' and 'SM star' in figure 5.2, and interpreted as being due to unshocked Fe in the interior of the remnant. These results show that portions of the Fe-rich ejecta are still expanding freely, and have not yet been overrun by the reverse shock. However the amount of Fe inferred in these studies (< 0.16 M$_\odot$) is much less than the amount (0.6–0.8 M$_\odot$) predicted to be produced in the thermonuclear disintegration of a ∼1.4 M$_\odot$ white dwarf.

In the early phases of supernova remnant evolution, even the shock-heated plasma is far from thermal equilibrium in terms of either the ionization or particle (electron and ion) temperatures, as explained in chapter 3. The thermal X-ray spectrum of SN 1006 suggests an ionization timescale of $\tau = n_e t \sim 2 \times 10^9$ cm^{-3} s (Vink et al. 2000b), which is far from the full ionization equilibrium, and lower than nearly all other Galactic SNRs. Moreover, the electron temperature just behind the northwest (NW) rim of the remnant has been estimated to be $kT_e \sim 0.7$ keV (Long et al. 2003) or ~ 1.5 keV (Vink et al. 2003), which are much lower than the ion temperature expected from the shock velocity of the NW rim (∼2980 km s^{-1}: Ghavamian et al. 2002). Therefore, non-equilibration of ion and electron temperatures is present in SN 1006 as well.

The extreme non-equilibrium state and high shock velocity are likely due to the low density of the ambient gas, because SN 1006 ($b = +14.6$) is further from the Galactic plane than other Galactic SNRs, such as Cas A ($b = -2.1$) and Tycho's SNR ($b = +1.4$). Although Kepler's SNR ($b = 6.8$) is nearly as far above the plane as SN1006 (when their respective distances are included), Kepler appears to be evolving into a dense circumstellar medium. Therefore, the evolutionary state of SN 1006 may be the lowest of these youngest Galactic SNRs, even though the real age is ∼3 times older than the others.

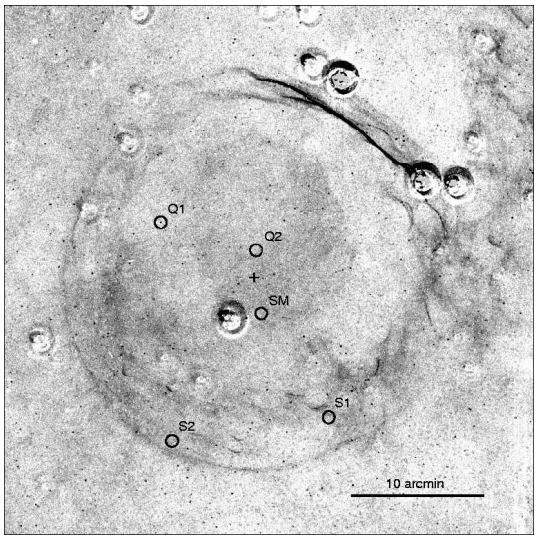

Fig. 5.2.—: Background UV sources are marked on Hα image of SN 1006, which shows the faint non-radiative filaments that delineate the primary shock around most of the shell (Winkler et al. 2003). The cross indicates the geometric center of the optical shell. This image is taken from Winkler et al. (2005).

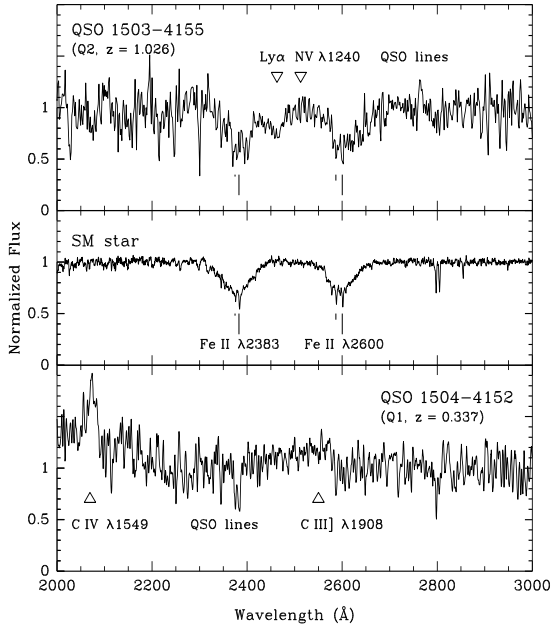

Fig. 5.3.—: Top: Normalized (to the continuum level) UV spectra of Q2 (labeled in figure 5.2) in the wavelength region of prominent Fe II lines. It shows clear evidence for broad absorption features. Middle: Same to top but the spectra of SM star. Similar absorption profile is seen. Bottom: the Q1 spectrum. It shows no evidence for broad Fe II lines; the narrow lines are probably of interstellar origin. This figure is taken from Winkler et al. (2005).

Table 5.1:: Log of Suzaku observations on SN 1006 and North Ecliptic Pole.

Region	Obs. ID	Date	Exposure (ks)
NE	100019020	2005/09/09	43
SW	100019030	2005/09/10	31
	100019050	2006/01/26	31
SE	500016010	2006/01/30	52
NW	500017010	2006/01/31	53
NEP*	500026010	2006/02/10	82

*North Ecliptic Pole, used as background data.

5.2 Suzaku Observation

Four pointings were made of SN 1006 with Suzaku during the performance verification (PV) phase. The observation ID, date, and exposure time are listed in table 5.1. During all of these observations, the XIS were operated in the normal full-frame clocking mode with the editing mode of 3×3 or 5×5. We employed the cleaned revision 0.7 data, and used the HEADAS software version 6.0.4 and XSPEC version 11.3.2 for the data reduction and analysis. The X-ray data taken during low cut-off rigidity ($\leq$ 6 GV) were excluded so as to minimize any possible uncertainty in the non X-ray background (NXB). The total effective exposure times after these screening were $\sim$50 ks, for each of the pointings. The response matrix files (RMF) and ancillary response files (ARF) were made using `xisrmfgen` and `xissimarfgen` (Ishisaki et al. 2007) version 2006-10-17.

5.3 Overall Structure

5.3.1 Thin-Thermal Plasma Map

The field of view (FOV) of the XIS is $\sim 18' \times 18'$, and hence a four-point mosaic can completely cover SN 1006 (about $30'$ diameter). Since we intended to study the thermal plasma, we searched for the region of the remnant with the most prominent thermal emission. We hence made a mosaic image in the O VII Kα line band (0.55–0.6 keV), because this line is a major component of the thermal plasma in SN 1006. The result is shown in figure 5.4. We can see bright emission in this band in the northeast (NE) and southwest (SW) regions of the remnant. However, these are dominated by non-thermal emission (Koyama et al. 1995), from which it is difficult to extract thermal spectra. Other regions are dominated by thermal emission. In particular, as shown in figure 5.4, the southeast quadrant (here SN 1006 SE) is brighter than the NW. Therefore, our study concentrated on this region. The spectral results of non-thermal rims (NE and SW) are reported by Bamba et al. (2008). The FOV of the XIS on SN 1006 SE is outlined by the black solid square in figure 5.4.

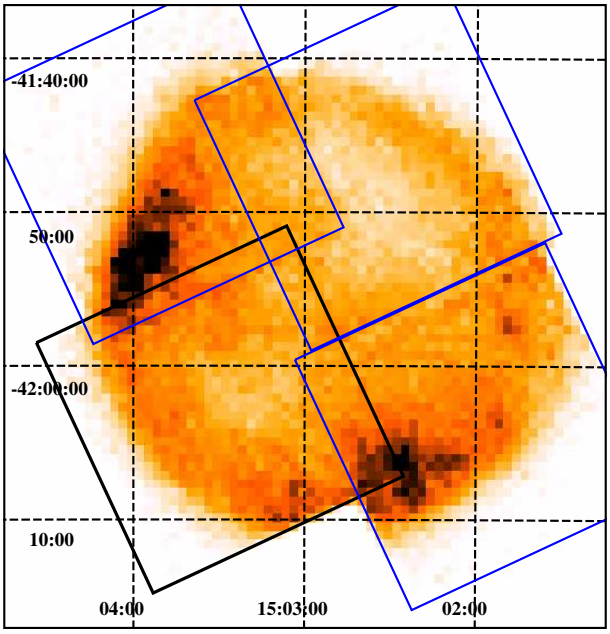

Fig. 5.4.—: XIS-BI mosaic image of SN 1006 in the 0.55–0.6 keV band. Exposure and vignetting effects are corrected. The coordinates (R.A. and Dec) are referred to epoch J2000.0. The black square shows the FOV of the XIS on the SE region of SN 1006 where this chapter is concentrated. The blue squares show the FOVs on the other three quadrants (NE, NW, and SW).

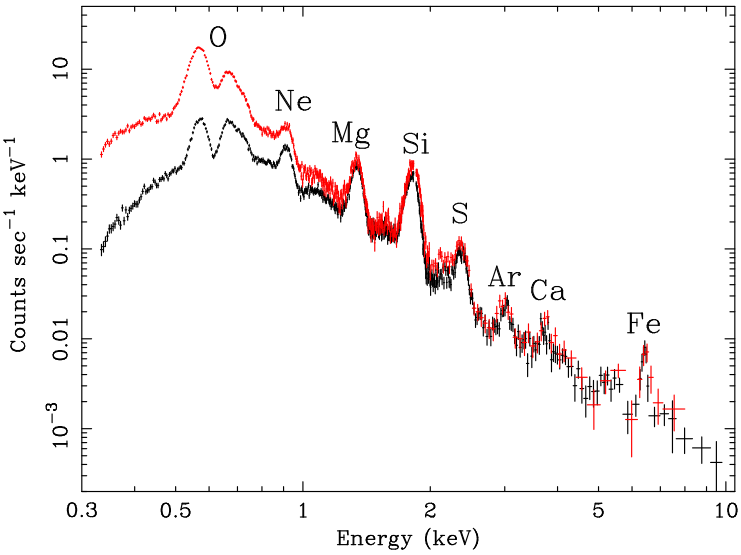

Fig. 5.5.—: Background-subtracted XIS spectra extracted from the whole SE quadrant (SN 1006 SE). The black and red points represent the FI and BI spectra, respectively.

5.3.2 Spectrum of the SN 1006 SE Region

We extracted the spectrum of the entire SN 1006 SE region, excluding the two corners in the FOV that contain calibration source emission. For the background, we used the North Ecliptic Pole (NEP) data. Although we have been monitoring and correcting the increase of the Charge-Transfer Inefficiency (CTI) for the XIS (section 4.3; Koyama et al. 2007), recovery of the energy resolution cannot be made. However, we can ignore the difference of the spectral resolution between the SN 1006 SE and NEP observations, because the latter observation was made only ten days after the former (see table 5.1). To minimize the uncertainty due to the background subtraction, in particular that of NXB, we applied the same data-screening criteria to both the SN 1006 SE and NEP observations, and took background spectra from the same detector coordinates as the source regions after excluding point-like sources detected in the NEP data. The background-subtracted spectra are shown in figure 5.5. Since the data from the three FIs are nearly identical, we merged those individual spectrum to improve the photon statistics.

As shown in figure 5.5, we found clear K-shell (Kα) lines from Ar, Ca, and Fe, for the first time. With a power-law plus Gaussian-line fit, we determined the line center energy of the Fe-Kα to be $\sim$6.43 keV. This energy constrains the Fe ionization state to be approximately Ar-like (Fe IX) and Ne-like (Fe XVII) . The lack of Fe-L emissions (which are generally seen in 0.7–1.5 keV band) also indicates that Fe is below the Fe XVII state.

5.3.3 Iron Line Map

We show in figure 5.6 an image in a relatively narrow band (6.33–6.53 keV) that contains the Fe-Kα line. Data from the observation of the NW quadrant are included. In the other two regions, NE and SW, the non-thermal continuum flux at 6.33–6.53 keV is very high and therefore we cannot extract reliable information on the Fe-Kα flux. We do not show the images of these regions.

We can see that the Fe-Kα flux is enhanced at the southern part of the remnant (outlined in red with a ellipse), except for the NE and SW quadrants where the non-thermal emission is dominant. The mean surface brightness at 6.33–6.55 keV within the elliptical region is 8.5 ($\pm$ 0.5) $\times$ 10^{-9} photons cm^{-2} s^{-1} arcmin^{-2}, while that outside it (only in the SE and NW quadrants) is 4.6 ($\pm$ 0.3) $\times 10^{-9}$ photons cm^{-2} s^{-1} arcmin^{-2}. In order to study the thin-thermal spectrum with the best S/N ratio for Fe-K line, we extracted the X-ray spectrum from within the elliptical region, excluding the corner of the calibration sources. The background subtraction was made in the same way as that of the full-field spectrum. The results are given in figure 5.11. Hereafter, all detailed analyses are made using this spectrum.

5.3.4 Energy and Width of the Emission Lines

In order to study the line features, we fitted the spectra extracted from the elliptical region with a phenomenological model; a power-law for the continuum and Gaussians for the emission

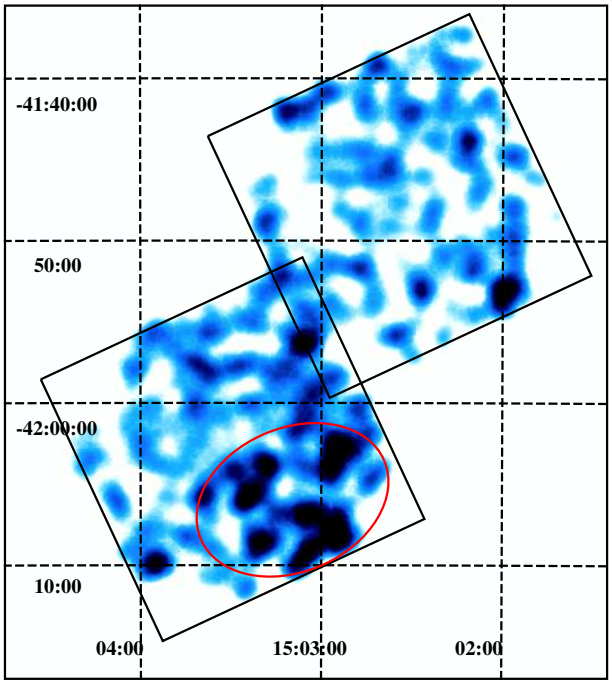

Fig. 5.6.—: XIS intensity map at the Fe-Kα line energies (6.33–6.53 keV). Exposure and vignetting effects are corrected. The data from the three FIs are combined. Two corners of the calibration sources are removed. The two black squares indicate FOVs of the XIS (on SN 1006 SE and NW). Since the non-thermal continuum flux at 6.33–6.53 keV is very high in the regions of NE and SW, we cannot extract reliable information of the Fe-Kα flux, and hence we do not show the images of these regions. The red ellipse shows the region where we extracted the spectra for a detailed analysis.

Table 5.2:: The center energies and widths of the emission lines.

Line	Center energy* (eV)	Width† (eV)
Mg-Kα	1338 (1337–1340)	< 5.4
Si-Kα	1815 (1813–1816)	40 (38–42)
S-Kα	2361 (2355–2365)	60 (54–65)
Ar-Kα	3010 (2991–3023)	< 50
Ca-Kα	3692 (3668–3724)	< 57
Fe-Kα	6430 (6409–6453)	< 60

* Errors (statistical only) are given in the parentheses (see text).

†One standard deviation (1σ).

lines. The best-fit central energies and widths for the emission lines are shown in table 5.2. Since the absolute energy calibration error is ±0.2% above 1 keV (Koyama et al. 2007), the relevant elements are uniquely identified from the best-fit central energy. These are also listed in table 5.2. Except for Mg, the central energies are significantly lower than that of the respective He-like Kα lines (see table 3.1). We also note that the widths of the Gaussians identified with Si-Kα and S-Kα are significantly broader than the instrumental energy resolution at those energies. Figure 5.9a would help to compare the widths of the data with those of narrow lines. In subsection 5.4.3, we discuss this matter in detail.

5.4 Spectral Structure in the Narrow Bands

In order to study the plasma characteristics in relation to the various elements, we at first divided the spectrum into three representative energy bands: the 0.4–1.1 keV band for the O and Ne (light elements) lines, the 1.2–2.8 keV band for the Mg, Si, and S (medium elements) lines, and the 5–10 keV band for the Fe (heavy element) line. With the fitting to these individual band spectra, we constrained the plasmas including light, medium, and heavy elements separately.

5.4.1 The 5–10 keV Band Spectra

We fitted the 5–10 keV spectrum with a solar abundance (Anders and Grevese 1989) VNEI model. Since the NEIvers 2.0 plasma code does not include K-shell emission lines for ions below the He-like state, we reverted to the NEIvers 1.1 code. If we fix the Fe abundance to be solar,

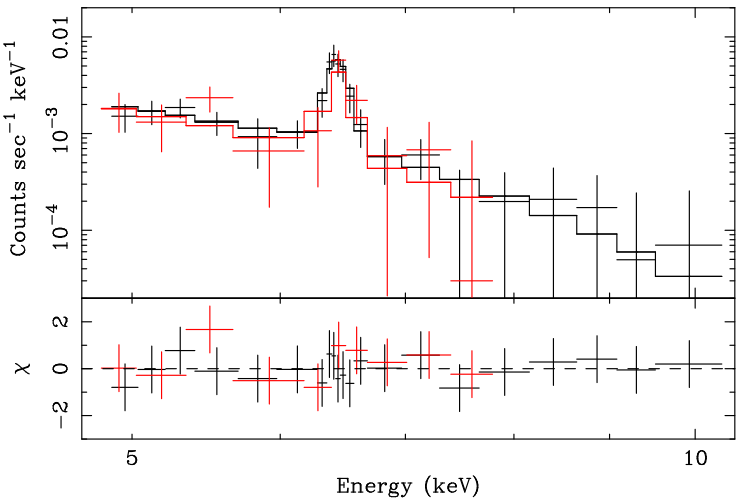

Fig. 5.7.—: XIS spectra in the 5–10 keV band with the VNEI model. The black and red data points represent the FI and BI spectra, respectively. In the BI spectrum, the energy band above 8 keV is ignored.

then the model cannot reproduce the Fe-Kα profile or flux, although the χ^2/d.o.f. of 25/28 is acceptable. Allowing the Fe abundance to be free results in a greatly improved best-fit χ^2/d.o.f. of 10/27. The best-fit kT_e, n_et, and Fe abundance are 3.8 (1.7–26) keV, 6.1 (2.2–10) $\times 10^9$ cm^{-3} s, and 6.5 (>1.9) solar, respectively. The Fe abundance is significantly enhanced relative to solar, even if the continuum flux in this band is assumed to be composed of pure thermal emission. The best-fit spectrum is shown in figure 5.7.

5.4.2 The 0.4–1.1 keV Band Spectra

Figure 5.8 shows the 0.4–1.1 keV band spectra. This energy band includes Kα lines of the light elements, with dominant emission from the oxygen K-shell line series. The spectra were fitted with a VNEI model, allowing the abundances of C, N, O, and Ne to be free parameters. Also, we let the abundances of Ca and Fe to be free, because the L-shell lines of these elements fall into this energy band (0.4–1.1 keV). Interstellar absorption was fixed to a hydrogen column density of 6.8×10^{20} cm^{-2} (Dubner et al. 2002). In the initial fits, we found a significant inconsistency between the FI and BI spectra near the energy of the O-edge (0.54 keV). This may be due to incomplete calibration information for the contamination layer on the optical blocking filter (OBF) of the XIS. Since the calibration of the OBF contamination for the BI is more accurate than that for the FI (see section 4.3), we decided to retain the BI data across this energy band and ignore the 0.5–0.63 keV band in the FI spectrum. The results are shown in figure 5.8a, with the best-fit temperature and ionization parameter of $kT_e = 0.58$ (0.56–0.59) keV and $n_et = 6.7$ (6.6–6.8) $\times 10^9$ cm^{-3} s.

In figure 5.8a, we find an apparent disagreement between the data and model in the ∼0.7–0.85 keV energy band. Usually, this energy band is dominated by the iron L-shell line transitions of $3s - 2p$ (∼730 eV) and $3d - 2p$ (∼830 eV) from Fe XVII. Although the fluxes of these two lines in NEI models are nearly equal over a wide range of plasma conditions, extrapolation to the extremely low ionization states that we see here in SN 1006 is quite uncertain. In particular, for the young Type Ia SNR E0509–67.5, Warren and Hughes (2004) found that the Fe L-shell emission was dominated by an emission from a line feature near 0.73 keV, which was not sufficiently strong in the spectral models and had to be included as a separate Gaussian component. This 0.73 keV data excess (compared from model) is confirmed in a Suzaku spectrum of E0509–67.5 (chapter 6). Based on the strength of other Fe-L emission lines and the weakness of O emission in E0509–67.5 the additional line feature at 0.73 keV was confidently associated with Fe-L emission.

Although we cannot eliminate the possibility that the residual comes from faint Fe-L emission, here we consider a different explanation. The best-fit spectral model of the oxygen lines are shown in figure 5.8b, in which the black and red solid lines are K-shell transitions from O VII and O VIII, respectively. In most astrophysical plasmas, the best-fit temperature of ∼0.6 keV gives weak K-shell lines of O VII compared to those of O VIII. On the other hand, in lower temperature plasmas (e.g., $kT_e \sim 0.1 - 0.2$ keV) where the O VII Kα line is dominant, the line fluxes decrease rapidly along the K-shell transition series (K$\alpha, \beta, \gamma, \delta, \epsilon, \zeta$, etc.). Therefore, K-shell lines in the higher transitions can be safely ignored, and hence conventional NEI codes do not include O VII K-shell transition lines

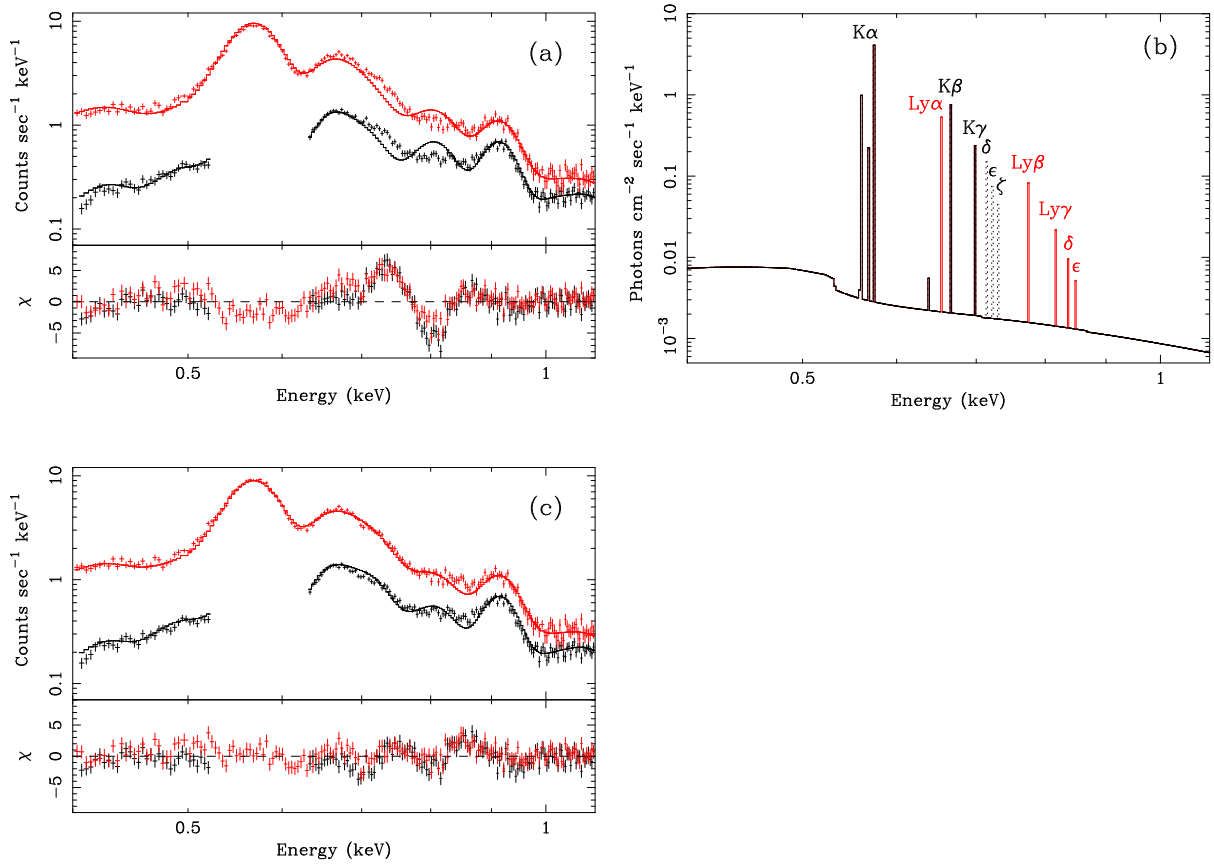

Fig. 5.8.—: (a) XIS spectra in the 0.4–1.1 keV band fitted with a VNEI model. The black and red data points represent the FI and BI spectra, respectively. (b) Spectrum in photon space corresponding to the model used in (a), but only showing O lines. It is binned every 2 eV. The black and red lines represent O VII series and O VII series, respectively. The dotted lines are additional transitions of Kδ (714 eV), Kϵ (723 eV), and Kζ (730 eV) of O VII added as separate Gaussians (see text). (c) Same spectra as (a), but for fits including Gaussians representing Kδ (714 eV), Kϵ (723 eV), and Kζ (730 eV) of O VII (see text). The residuals in the energy band 0.7–0.85 keV seen in (a) are largely removed.

higher than Kδ. This is the reason that no oxygen line in the ∼0.7–0.85 keV band is present in the best-fit model (figure 5.8b). In SN 1006, however, the ionization timescale is low, while kT_e is moderate, so the fluxes of higher level K-shell transitions from O VII may be relatively strong and cannot be ignored. To account for them we added Gaussians at 714 eV, 723 eV, and 730 eV to represent the O VII Kδ, Kϵ, and Kζ lines, respectively. At a plasma temperature of 0.6 keV, the flux ratio of O VIII Lyϵ to Lyδ predicted by the NEIvers 1.1 code is ∼0.5 (see figure 5.8b). In the absence of a detailed calculation we merely assumed that the flux ratio of the O VII lines follow the same pattern, namely Kϵ/Kδ = Kζ/Kϵ = 0.5. The best-fit results with these additional lines, see figure 5.8c, are a reasonably good fit. The additional artificial lines are also shown as the dotted lines in figure 5.8b. The temperature and ionization parameter are almost the same as those obtained without the additional higher K-shell transitions of O VII.

The best-fit intensity ratio of O VII Kβ to O VIII Lyα is ∼1.4, which is consistent with the result of the XMM-Newton/RGS observation of the X-ray knot localized at the NW rim of SN 1006 (Vink et al. 2003; O VII Kβ/O VIII Lyα ∼ 1.6). This agreement may justify our approach to include the K-lines manually. Also, this suggests that the O VII K-shell line series are key spectral components for all over the SN 1006 plasma.

5.4.3 The 1.2–2.8 keV Band Spectra

This band includes K-shell lines of intermediate-mass elements (Mg, Si, and S). As shown in table 5.2, we can see significant broadening of the Si and S Kα lines. Therefore, the 1.2–2.8 keV band spectra cannot be reproduced with a single-component plasma model. In fact, we found significant disagreement between the data and model around the Si-Kα and S-Kα lines (figure 5.9a) in the one-component VNEI fits. The lack of data in the 1.83–1.85 keV band is due to current calibration errors of the XIS; there is a small gap in energy (∼10 eV) at the Si K-edge, which is not implemented in the current response function. The apparent line broadening of the Si Kα line, however, is much larger (∼40 eV) than this gap. Therefore, the disagreement is not due to a calibration error, but is real.

If the intrinsic broadening of the Si-Kα line (~ 40 eV; see table 5.2) is due to thermal Doppler broadening, the ion (silicon) temperature must be ~ 13 MeV, which requires a shock velocity of $\sim 1.5 \times 10^4$ km s^{-1}, (derived from equation 3.36). Ghavamian et al. (2002) determined the shock velocity (from measurements of the Hα line width) to be ∼2900 km s^{-1} in the NW portion of SN 1006. This region is where the blast wave is interacting with significant amounts of interstellar matter, compared to other parts of the rim. In fact, the average size of the remnant (∼15.′5 radius) and the well-known age and distance allow us to determine a mean expansion speed for SN 1006 to be ∼10^4 km s^{-1}. The true current blast wave speed in SN 1006 is almost surely bracketed by these two values. Furthermore, the reverse shock, which is likely to be the heating source for the Si that we see, typically moves into the ejecta at only a fraction of the blast wave speed. Therefore, we consider it unlikely that the line broadening is due to thermal Doppler broadening.

Another possible explanation proposes that the emission consists of several thermal plasma

components. We fitted the spectra with 2-VNEI models, in which we allowed for different kT_e values, but the same n_et between components. However, no combination of parameters would fit the data, even if we let the abundances of Mg, Si, and S be free parameters. Not only 2-VNEI, but also 2-VPSHOCK models failed to fit the data when the two components were forced to have the same ionization timescale. All of the models that we tried, but rejected, are summarized in table 5.3. The addition of a power-law component to these models also did not help to improve the fittings.

Next we tried two-component VNEI models with the same electron temperature, but different n_et values. The best-fit reduced χ^2/d.o.f. was greatly improved to 401/346 (see table 5.3, for comparison). Models with different electron temperature and ionization timescale (2-kT_e and 2-n_et) gave no significant improvement of the reduced χ^2. We thus conclude that a 2-component VNEI model with different n_et values is necessary to fit the medium element plasma band. The best-fit parameters and spectra are given in table 5.4 and figure 5.9b, respectively.

Table 5.3:: Best-fit parameters and χ^2 values of the spectral fitting in the 1.2–2.8 keV band with the various models.

Model	kT_{e1} (keV)	kT_{e2} (keV)	n_et (cm^{-3} s)	χ^2/d.o.f.
1-VNEI	1.5	–	4.5×10^9	848/351
2-VNEI	0.18	20	8.4×10^9	706/346
1-VPSHOCK	1.6	–	8.3×10^9	726/351
2-VPSHOCK	0.36	12	1.0×10^{10}	597/346

Table 5.4:: Best-fit parameters of the spectral fitting in the 1.2–2.8 keV band with 2-component VNEI model with different n_et values.

Parameter	Component 1	Component 2
$N_{\rm H}$ (cm^{-2})	6.8×10^{20} (fixed)	
kT_e (keV)	1.1 (1.0–1.2)	
Mg	4.2 (3.5–5.2)	6.1 (3.5–13)
Si	19 (15–24)	15 (13–24)
S	24 (19–34)	23 (17–31)
n_et (cm^{-3} s)	1.3 (1.1–1.7) $\times10^{10}$	7.9 (6.2–9.8) $\times10^8$
$n_{\rm H}n_eV$ (cm^{-3})	2.8 (2.3–3.4) $\times10^{55}$	1.9 (1.6–2.3) $\times10^{56}$
χ^2/d.o.f.	401/346 = 1.16	

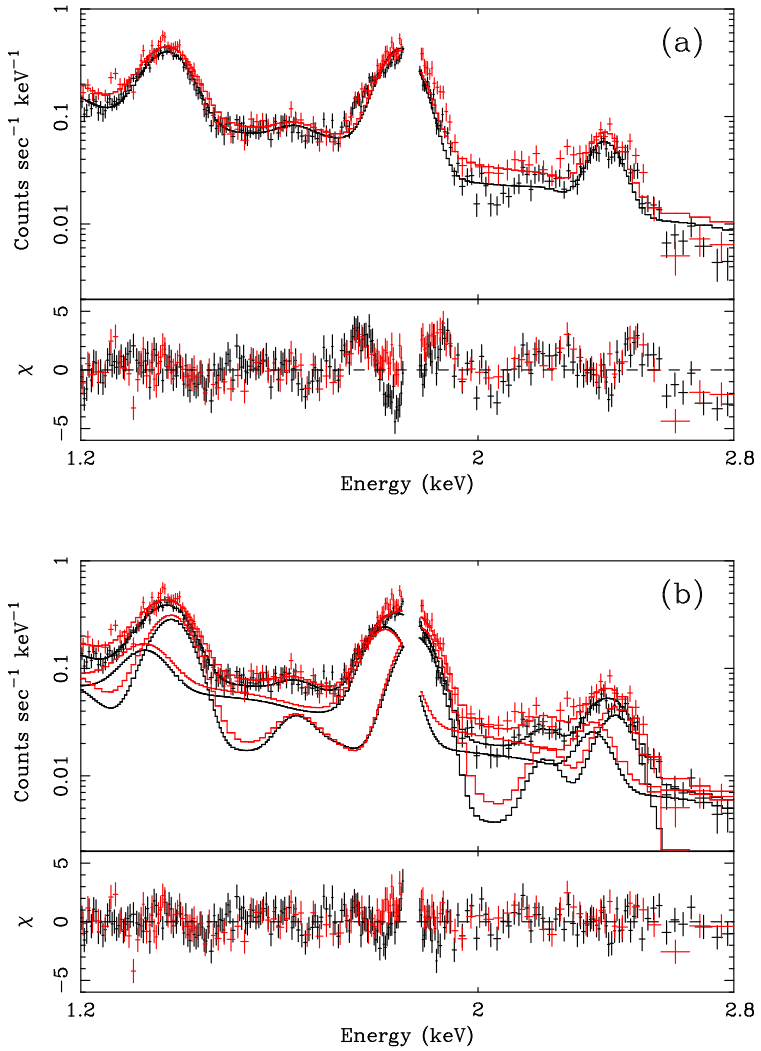

Fig. 5.9.—: (a) XIS spectra in the 1.2–2.8 keV band fitted with the one-component VNEI model. The black and red represent the FI and BI, respectively. (b) Same to (a), but fitted with the two-component VNEI.

5.5 Model Fit of the Full Band Spectra

In section 5.4, we discuss how we separately derived spectral parameters for the three-energy bands that represent typical plasma conditions for the main light elements (O and Ne), medium elements (Mg, Si, and S), and heavy element (Fe). A summary is given in table 5.5. We used these parameters as the initial values to search for plasma parameters in the full energy band of 0.3–10 keV; the resulting overall best-fit parameters must be consistent with the data over the entire XIS energy band.

Based on table 5.5, we assume that the model that describes the full spectral range must consist of, at least, three plasma components: (1) high-kT_e ($\sim$1 keV) with high-n_et ($\sim 10^{10}$ cm^{-3} s), (2) similarly high-kT_e with low-n_et ($\sim 10^9$ cm^{-3} s), and (3) low-kT_e (~ 0.6 keV) with medium-n_et ($\sim 7\times10^9$ cm^{-3} s). First, we consider whether or not the full band spectra can be well reproduced with only these components. We also consider a broader range of kT_e and n_et values for the Fe-K emission.

As shown in table 5.4, components (1) and (2) are significantly enhanced in Mg, Si, and S (relative to solar). In the present spectral fits, we made the assumption that these components are composed purely of metals without any admixture of hydrogen or helium. This assumption arose because hydrogen and helium emit only continuum emission in the X-ray band. Given the complexity of our spectral model, it is just not possible with the XIS data to obtain reliable estimates for the level of continuum emission from the three plasma components separately. As a further assumption, we fixed the abundance of component (3) to the solar value. (Anticipating the results given below, we found that most of the continuum emission above 1 keV actually comes from a hard power-law like spectral component.) Operationally, we fixed the oxygen abundance in both the pure-metal components (i.e., nos. 1 and 2) to a large value (1×10^4), and fitted for the abundances of other elements relative to oxygen. The C and Ni abundances were assumed to be the same as Ne and Fe, respectively. The emission measure (EM) in the plasma code is defined (in XSPEC) as $n_{\rm H}n_eV$, even if the plasma is dominated by heavy elements. However, the oxygen density can be calculated as $n_{\rm O} = (8.51\times10^{-4}n_{\rm H})\times10^4$, where the numerical value is the solar abundance of oxygen from Anders and Grevesse (1989). Details of this method can be found in Vink et al. (1996).

Table 5.5:: Plasma components determined from the narrow band spectra.

Band (keV)	Major elements	kT_e (keV)	n_et (cm^{-3} s)	Component*
0.4–1.1	O, Ne	0.58 (0.56–0.59)	6.7 (6.6–6.8)$\times10^9$	(3)
1.2–2.8	Mg, Si, S	1.1 (1.0–1.2)	1.3 (1.1–1.7)$\times10^{10}$	(1)
		1.1 (1.0–1.2)	7.9 (6.2–9.8)$\times10^8$	(2)
5.0–10	Fe	3.8 (1.7–26)	6.1 (2.2–10)$\times10^9$	

*The plasma component identifications described in text.

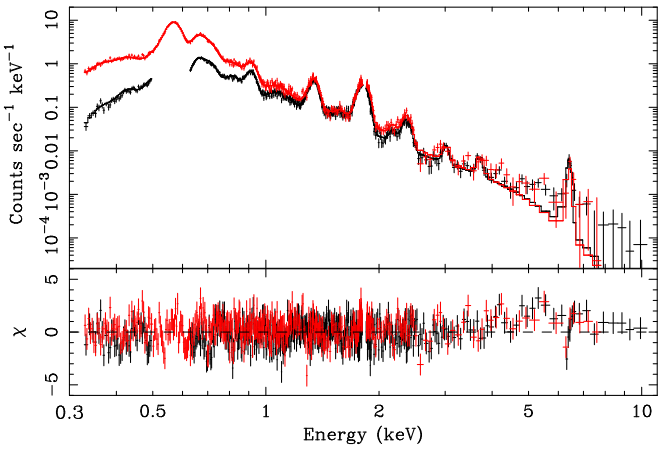

Fig. 5.10.—: XIS spectra in the 0.33–10 keV band fitted with the three-component plasma model (see text). The black and red points represent the FI and BI data, respectively. The model fails to describe the continuum emission above ∼4 keV.

Since the NEIvers 1.1 spectral model does not include K-shell emission lines from Ar and low ionization states of Ca, we added Gaussians at the energies of their Kα transitions: 3.02 keV (Ar) and 3.69 keV (Ca) (see table 5.2), For component (1) we additionally freely varied the Ca abundance, which effectively allowed for the Ca L-shell lines to contribute at low energies ($<$ 0.5 keV). For component (2), we tied the Ca abundance to that of Fe, which was allowed to vary freely. We also added Gaussians for the upper-level oxygen transitions at 0.714, 0.723, and 0.730 keV with the same reason as described in subsection 5.4.2.

We fitted the FI data in the energy band from 0.33 to 10 keV (0.33 to 8 keV for the BI data). We ignored the band below the C-edge at 0.28 keV, because of the large uncertainty in calibration due to contamination on the OBF (see section 4.3). Energies of 0.5–0.63 keV (only for FI) and 1.83–1.85 keV were also ignored for the same reasons as noted in subsections 5.4.2 and 5.4.3. Since the absolute gain of the XIS has an uncertainty of ±5 eV (Koyama et al. 2007), we allowed for a small offset in the photon-energy to the pulse-height gain relationship.

With this model and assumptions, the best-fit χ^2/d.o.f. obtained was 1081/833. The fitted spectra are shown in figure 5.10. All line features are well fitted, even Fe-K, suggesting that including additional thermal components would not be justified. However, there is a systematic data excess in the continuum at energies $\gtrsim$ 4 keV. We include a power-law component to this model, since we cannot reject the possibility that there is a non-thermal component here that is similar to the bright NE and SW rims (albeit much less intense). The fit with the additional power-law was significantly improved with χ^2/d.o.f. = 996/831. The best-fit parameters are given in table 5.6. As already noted, the gain may have an uncertainty of ±5 eV. The fitting process requires a gain offset of 4.8 eV for both FI and BI, within the allowable range. The best-fit model in the full energy band is shown in figure 5.11.

Table 5.6:: Best-fit parameters of the broadband spectral fitting.

Component	Parameter		Value
Absorption	$N_{\rm H}$ ($\rm cm^{-2}$)		6.8×10^{20} (fixed)
VNEI 1 (Ejecta 1)	kT_e (keV)		1.2 (1.1–1.4)
	Abundance (10^4 solar)	C	0.19* (0.08–0.30)
		N	0 (fixed)
		O	1.0 (fixed)
		Ne	0.19* (0.08–0.30)
		Mg	4.1 (3.7–4.7)
		Si	17 (15–20)
		S	23 (20–27)
		Ca	11 (9.6–13)
		Fe	0.68† (0.62–0.76)
		Ni	0.68† (0.62–0.76)
	n_et ($\rm cm^{-3}$ s)		1.4 (1.2–1.6) $\times10^{10}$
	$n_{\rm H}n_eV$ ($\rm cm^{-3}$)		2.7 (2.4–3.0) $\times10^{51}$
VNEI 2 (Ejecta 2)	kT_e (keV)		1.9 (1.5–2.6)
	Abundance (10^4 solar)	C	0.33‡ (0.23–0.45)
		N	0 (fixed)
		O	1.0 (fixed)
		Ne	0.33‡ (0.23–0.45)
		Mg	3.0 (2.2–3.9)
		Si	10 (8.6–12)
		S	12 (9.1–16)
		Ca	18§ (5.1–44)
		Fe	18§ (5.1–44)
		Ni	18§ (5.1–44)
	n_et ($\rm cm^{-3}$ s)		7.7 (6.7–9.2) $\times10^{8}$
	$n_{\rm H}n_eV$ ($\rm cm^{-3}$)		1.8 (1.3–2.5) $\times10^{52}$
NEI (ISM)	kT_e (keV)		0.51 (0.31–0.55)
	n_et ($\rm cm^{-3}$ s)		5.8 (5.7–6.1) $\times10^{9}$
	$n_{\rm H}n_eV$ ($\rm cm^{-3}$)		1.1 (1.0–1.2) $\times10^{56}$
Power-law	Γ		2.9 (2.8–3.0)
	Norm‖ (photons $\rm cm^{-2}$ $\rm s^{-1}$)		6.3 (5.5–7.2) $\times10^{-4}$
Gaussian lines to complement the incomplete VNEI code (see text)			
Line	Center Energy(keV)(fixed)		Norm (photons $\rm cm^{-2}s^{-1}$)
O VII-Kδ	0.714		6.4 (6.1–6.6) $\times10^{-4}$
O VII-Kϵ	0.723		3.2 $\times10^{-4}$ #
O VII-Kζ	0.730		1.6 $\times10^{-4}$ **
Ar-K	3.01		5.7 (4.4–7.0) $\times10^{-6}$
Ca-K	3.69		2.4 (1.3–3.5) $\times10^{-6}$
Gain	Offset (eV)		–4.8
χ^2/d.o.f.			996/831 = 1.20

*, †, ‡ and § represent linked parameters.

‖The differential flux at 1 keV.

#Fixed to 50% of the normalization of O VII-Kδ.

**Fixed to 50% of the normalization of O VII-Kϵ.

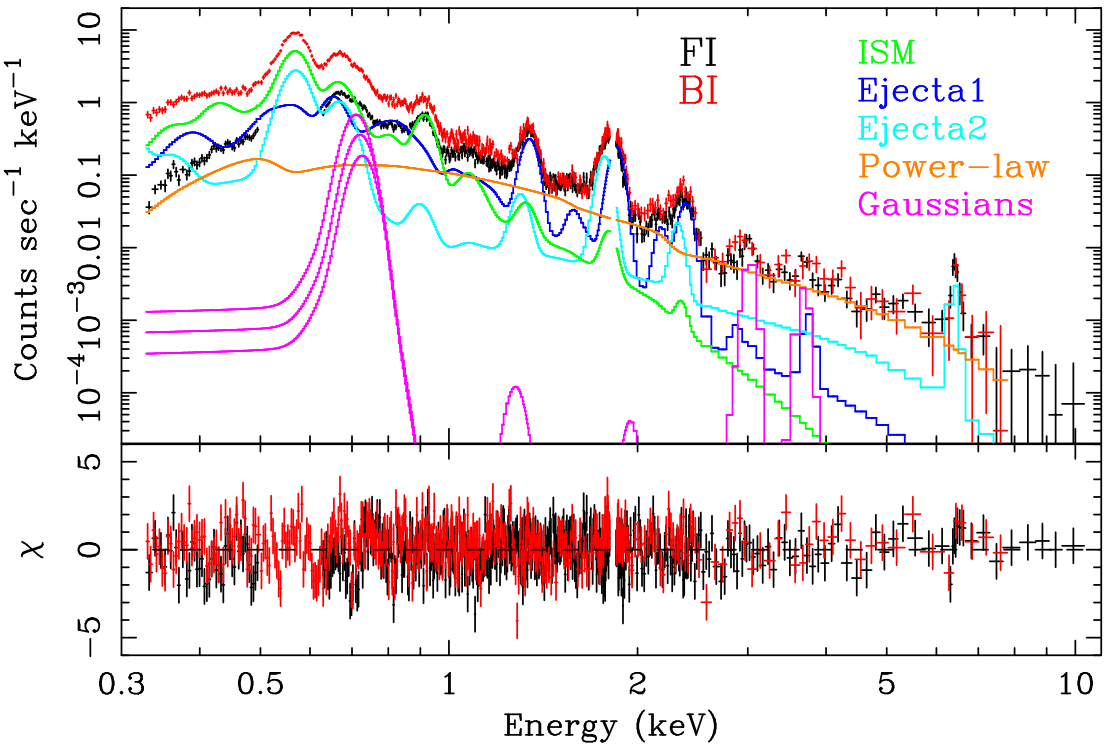

Fig. 5.11.—: XIS spectra in the 0.33-10 keV band which were extracted from the red elliptical region shown in figure 5.6. The black and red data points represent the FI and BI spectra, respectively. The solid lines, colored green, blue, light blue, orange, and magenta show the components of the ISM, Ejecta 1, Ejecta 2, Power-law, and additional Gaussians of the best-fit model for the BI spectrum. Note that the Gaussian like structures (magenta) at ∼1.2 keV and ∼1.9 keV are Si escape peaks (see figure 4.9 in section 4.3) of the added Gaussians at 3.02 keV and 3.69 keV due to the XIS response.

5.6 Discussion for SN 1006

In section 5.5, we analyzed the full energy band spectrum extracted from the elliptical region shown in figure 5.6, and found that it could be described adequately with a parameterized model including three thermal plasmas in non-equilibrium ionization (VNEI 1, VNEI 2, and NEI, in table 5.6) and one power-law component (Power-law, in table 5.6). Two of the plasmas, VNEI 1 and VNEI 2, were assumed to have non-solar abundances, and the other, NEI, was assumed to have solar composition. In the following we discuss the implications of our spectral results.

5.6.1 Origin of the Plasmas

The NEI model, assumed to have solar abundances, produces most of the observed low-energy X-rays, particularly the Kα lines from O VII, O VIII, and Ne IX (see figure 5.11). This component is rather uniformly extended over the entire remnant, as can be seen in the O VII line band map (figure 5.4). We associate this component with the swept-up ISM.

The other plasmas, VNEI 1 and VNEI 2, with their non-solar elemental abundance ratios, are plausibly of ejecta origin. Since VNEI 1 has a larger ionization parameter than the other plasmas, we suggest that this plasma was heated by reverse shock in the early stage of remnant evolution (here Ejecta 1). On the other hand, VNEI 2 has an extremely low ionization parameter, and hence should have been heated much more recently (here Ejecta 2). We have firmly detected Fe-Kα emission for the first time. The low ionization state of Fe, plus its overabundance in the Ejecta 2 component, is generally consistent with the Type Ia origin of SN 1006.

5.6.2 Relative Abundance in the Ejecta

We compare our best-fit relative abundances with the predicted nucleosynthesis yield of the widely-used W7 Type Ia SN model (section 2.3; Nomoto et al. 1984). For Ejecta 1, although the abundances of C, Ne, Mg, Si, and S relative to O are broadly consistent with the W7 model, Ca and Fe fall far below their predicted values, as shown in figure 5.12a. In the case of Ejecta 2, on the other hand, the heavy elements, albeit with large errors, are broadly consistent with the abundance pattern from the W7 model, as shown in figure 5.12b. These results, along with the difference in the ionization timescale between the components just mentioned, are consistent with a layed composition of the ejecta with the higher-Z elements more concentrated toward the center of SN 1006.

For this simple interpretation, one expects the Fe line emission from the low-ionization timescale component to be spatially located interior to the Mg and Si emission from the high-ionization component, i.e., near the center of SN 1006. As shown in figure 5.6, though, the Fe flux appears to peak close to the southeastern rim. In summary, our two-component spectral model for the ejecta is a highly simplified view of what is surely a complex multi-$n_e t$ and multi-kT_e structure that varies throughout the interior of the SNR. A longer observation, particularly of the inner

regions of SN 1006, will help to improve the statistical accuracy of the Fe-K line flux.

5.6.3 ISM Density and Ion Temperature

The plasma parameters given in table 5.6 were derived from the southeast solid ellipse of figure 5.6, which is $\pi \times 6.'1 \times 4.'4 = 84$ arcmin^2 in area. This corresponds to 3.3×10^{38} cm^2, from which we estimated the emission volume to be $V = (3.3 \times 10^{38})^{3/2} = 6.0 \times 10^{57}$ cm^3. Therefore, the EM of the heated ISM derived from the spectral fits corresponds to an electron density of $n_e = 0.15\ f^{-0.5}$ cm^{-3}, where f is the filling factor. Since the age of SN 1006 is ∼1000 yr, the ionization timescale can be roughly estimated as $n_e t \sim 4.7 \times 10^9$ cm^{-3} s, which is almost consistent with the best-fit value of the ionization parameter of the NEI (ISM) component. Such a low ionization age suggests that the temperatures of the ions and electrons may also be far from equilibrium. According to equation 3.39, under the assumption that the initial ratio between kT_e and $kT_{\rm H}$ just at the shock front is the ratio of the electron and proton masses, the proton temperature is estimated to be,

$$kT_{\rm H} = 7.8 \left(\frac{n_e t}{5.8 \times 10^9\ {\rm cm^{-3}s}} \right)^{-1} \left(\frac{kT_e}{0.51\ {\rm keV}} \right)^{5/2}\ [{\rm keV}]\ .$$

This result is consistent with that of the Hα observation of $T_e/T_{\rm H} \leq 0.07$ (Ghavamian et al. 2002). The extreme non-equilibrium state of the plasma is due to the low density of the ambient medium. According to equations (2) and (5) of Ferrière (2001), the density of H I and H II at the Z-height of SN 1006 ($Z = 550$ pc) is ∼0.03 cm^{-3}. This is consistent with our estimate of the ambient density of $n_{\rm H}/4 \sim 0.03$ cm^{-3}. Recently, Acero et al. (2007) obtained the gas density around the SE rim to be ~ 0.05 cm^{-3} using XMM-Newton data, which is consistent with our result.

5.6.4 The Power-Law Component

The low density of the ambient medium will allow the velocity of the shock front to remain high for a relatively long time. This may be one reason why this remnant shows such efficient particle acceleration up to very high energies ($\sim 10^{14}$ eV), observed as power-law (synchrotron) emission from the NE and SW rims (Koyama et al. 1995). The photon index from these rims is $\Gamma \sim$ 2.7–2.9. Now here, away from the bright rims, we also detect a power-law component in the hard energy band (the Power-law, in table 5.6) with a best-fit index of Γ ∼2.8–3.0, which is consistent with the NE and SW bright rim emission. Since the power-law emissions from the rims are most likely to be synchrotron X-rays, the power-law component newly found from the ellipse in figure 5.6 is also likely to be synchrotron X-ray emission. The surface brightness is estimated to be $\sim 6 \times 10^{-15}$ ergs cm^{-2} s^{-1} arcmin^{-2} in the 2–10 keV band. This value is ∼ 50-times lower than the peak emission at the NE and SW rims. If similar to the NE rim, the power-law component should show thin filamentary structures (Bamba et al. 2003). However, XMM-Newton (Rothenflug et al. 2004) and Chandra (Hughes et al., in preparation) observations found little evidence for filamentary X-ray rims along the SE rim.

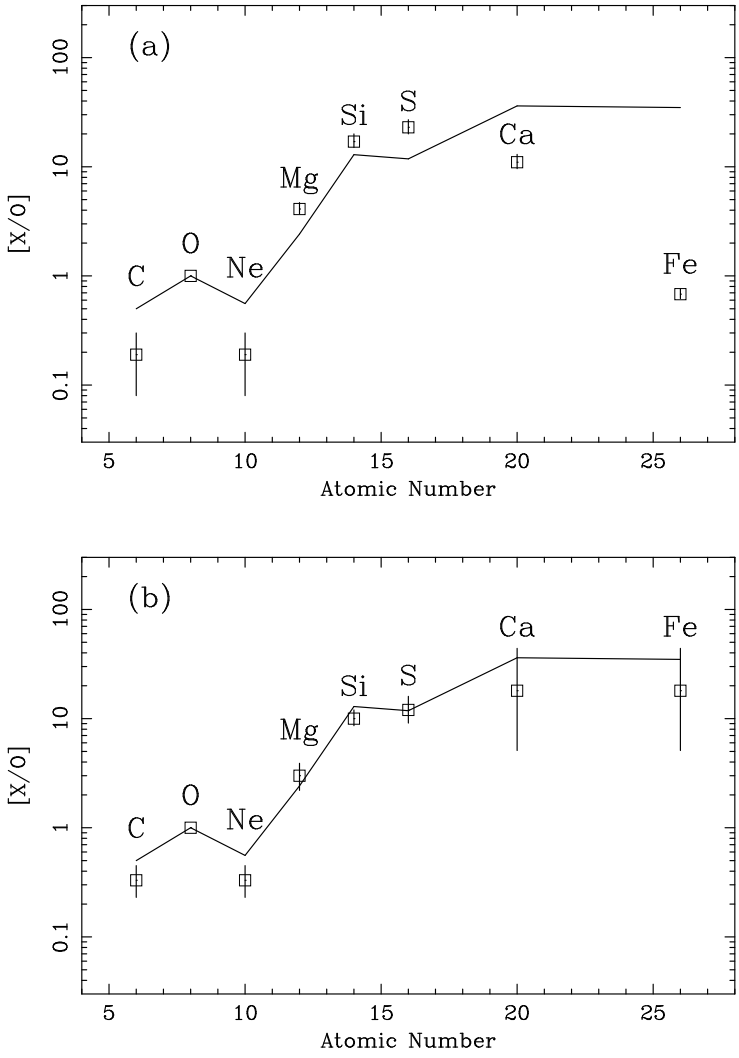

Fig. 5.12.—: Metal abundances as a function of atomic number derived from the spectral fitting. The data points of (a) and (b) represent those of Ejecta 1 and Ejecta 2, respectively. The solid lines show the abundance relative to oxygen calculated in the W7 model for a Type Ia supernova by Nomoto et al. (1984).

5.6.5 Summary for SN 1006

We have analyzed high-quality spectra obtained with Suzaku of a region in the southern part of SN 1006, selected because it is bright in Fe-Kα. The results and interpretations are summarized as follows:

1. The spectrum can be described by a model with at least three NEI thermal plasmas and one power-law component.

2. The fits yield different ionization parameters of $n_e t \sim 8 \times 10^8$ cm^{-3} s (low), $\sim 6 \times 10^9$ cm^{-3} s (medium), $n_e t \sim 10^{10}$ cm^{-3} s (high).

3. The low-$n_e t$ plasma are highly overabundant in heavy elements, in which we found Kα lines from Fe, for the first time. The abundance pattern is consistent with that of Type Ia SN ejecta.

4. The abundance of the medium-$n_e t$ plasma is assumed to be solar, and we associate this component with the shocked ISM. Although oxygen is not overabundant, Kα lines of O VII and O VIII from this plasma appear to dominate the thermal emission from SN 1006.

5. The high-$n_e t$ plasma is overabundant in medium elements, like Mg, Si, and S, but heavy element like Fe. Our interpretation is that this plasma also has an ejecta origin, and the composition is dominated by lower atomic number species.

6. Temperature equilibrium between ions and electrons has not yet been achieved. The proton temperature of the shocked ISM is $\sim$15-times higher than the electron temperature.

7. The spectrum from this region contains a power-law component. The photon index, $\Gamma \sim 2.9$, is similar to that of the northeast and southwest bright rims, suggesting that this component is also of synchrotron origin.

Chapter 6

E0509–67.5

E0509–67.5 is probably the youngest Type Ia SNR in the Large Magellanic Cloud (LMC). (SN 1987A is younger, but is a core-collapse type.) Therefore, X-rays from E0509–67.5 are dominated by the radiation from the ejecta, similarly to SN 1006. Since the LMC is a face-on galaxy and is located in the high Galactic latitude region, the X-rays can be observed without almost suffering from the interstellar absorption. Furthermore, the distance to the LMC is well-known to be 51 kpc (Feast et al. 2002), and hence the amounts of synthesized elements in the SNR ejecta can be investigated with a high reliability. In this chapter, we summarize the results of Suzaku observation on E0509–67.5, and discuss the nucleosynthesis of its progenitor.

6.1 Previous Results

E0509–67.5 was discovered by an X-ray survey of the LMC with the Einstein Observatory (Long et al. 1981). With an Hα observation, the remnant was found to have a very circular shell-like structure (Tuohy et al. 1982), as shown in figure 6.1. It shows no detectable emission in O III and Si II, indicating a Balmer-dominated remnant (Smith et al. 1991; 1994). Hα studies also found it has a very fast shock velocity of $\gtrsim 2000$ km s^{-1}, and a young age of $\lesssim 1500$ yr (Smith et al. 1991). Radio observations obtained a spectral index of $\alpha = 0.46$ (Mathewson et al. 1983) and a differential flux of 0.066 Jy at 1 GHz (Hendrick & Reynolds 2001), of which the origin is suggested to be synchrotron emission.

In X-rays, ASCA found, for the first time, its spectrum has strong K-shell emissions of Si and S, and L-shell emissions of Fe, with much weaker O, Ne, and Mg K-shell emission (Hughes et al. 1995). This fact strongly suggests that E0509–67.5 has a Type Ia SN origin. With a great spatial resolution, Chandra revealed the clear shell-like structure in the X-ray image (figure 6.2), and obtained its inner and outer radii to be 12.8 arcsec and 15.2 arcsec, respectively (Warren & Hughes 2004). Furthermore, they concluded that the age is less than 860 yr, if the constant-density ejecta profile is assumed. The most serious issue raised by the Chandra observation is that the

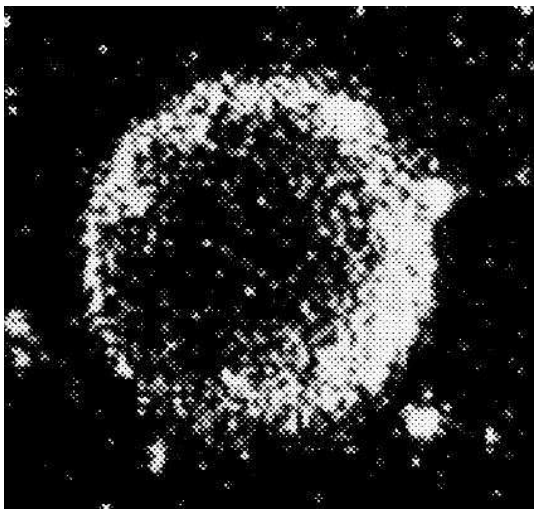

Fig. 6.1.—: Hα image of E0509–67.5, taken from Tuohy et al. (1982). North is up and east is to the left.

ionization age of Fe is higher than those of other elements. This picture is not similar to the Suzaku result on SN 1006 which we derived in chapter 5. However, the efficiency and energy resolution of Chandra is relatively poor, especially in the energy band of Fe-K emission. Therefore, it is possible that the ionization age was not measured exactly. We hence observed E0509–67.5 to perform an accurate plasma diagnosis.

The density of the ambient gas is known to be very low ($\lesssim 0.02$ cm^{-3}: Tuohy et al. 1982; $\lesssim 0.05$ cm^{-3}: Warren & Hughes 2004), similarly to SN 1006. Therefore E0509–67.5 is also suited to the study of the X-ray spectral property in the very early phase of SNR evolution.

6.2 Suzaku Observation

The Suzaku observation of the SNR E0509–67.5 was made on 2006 August 18 (Observation ID = 501041010) with the targeted position at (RA, Dec) = (05:09:33, –67:30:54). The XIS were operated in the normal full-frame clocking mode. We employed the cleaned revision 1.2 data (almost consistent with the revision 0.7 data used in the analysis of SN 1006), and used the HEADAS software version 6.0.4 and XSPEC version 11.3.2 for the data reduction and analysis. The X-ray data taken during low cut-off rigidity (≤ 6 GV) were excluded to minimize positional dependence of the NXB. After the screening, the effective exposure time was obtained to be $\sim$45 ksec. The response matrix files (RMF) and ancillary response files (ARF) were made using `xisrmfgen` and `xissimarfgen` (Ishisaki et al. 2007) version 2006-10-17.

Figure 6.3 shows the XIS image in 0.5–5.0 keV band. Since the diameter of the SNR ($\sim 30''$) is much smaller than the angular resolution of the XRT, ($\sim 2'$: Serlemitsos et al. 2007), the SNR can be regarded as a point-like source spread by the effect of the PSF (see section 4.2).

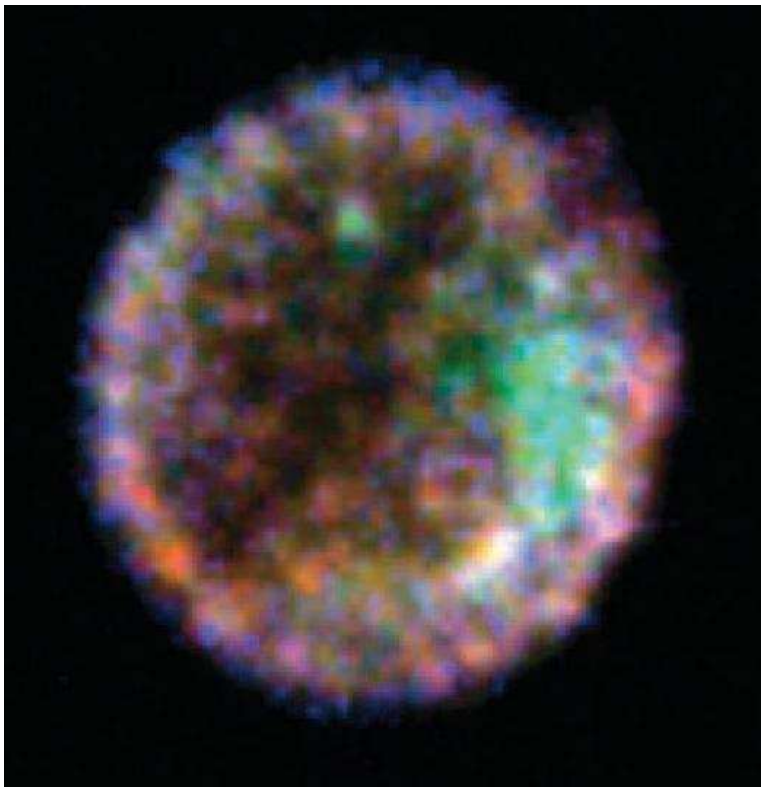

Fig. 6.2.—: Chandra image of E0509–67.5, taken from Warren & Hughes (2004). Red, green, and blue contain emission from 0.2–0.69 keV, 0.69–1.5 keV, and 1.5–7 keV, respectively. North is up and east is to the left.

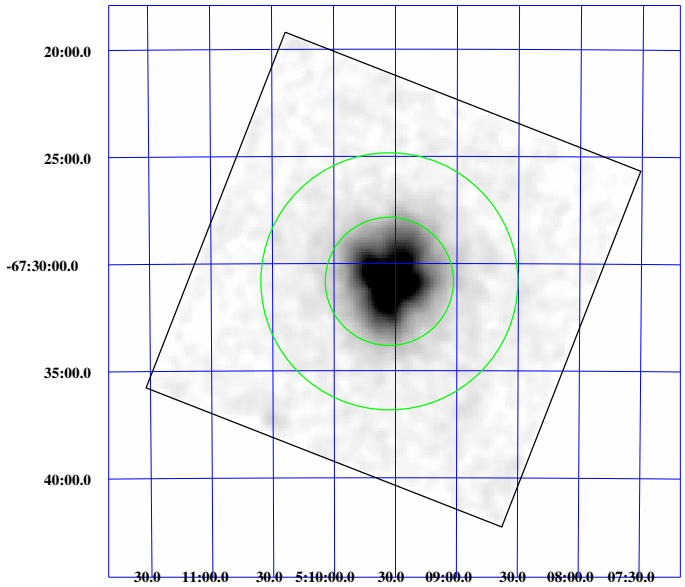

Fig. 6.3.—: XIS 0.5–5.0 keV image. The coordinates (RA, Dec) refer to epoch J2000.0. The field of view of the XIS is indicated by the black square, where the data from the four XIS are combined. The green circle and annulus are the source and background regions, respectively.

6.3 Spectral Structure in the Narrow Bands

We extracted XIS spectra from a circular region of $3'$ radius centered on E0509–67.5 shown in figure 6.3. The X-ray flux in this region is $\sim$95% of the total flux of the source (see the right panel of figure 4.5 in section 4.2). The background spectra were extracted from the annular region around the source with inner and outer radii of $3'$ and $6'$, respectively. The background region is also shown in figure 6.3. Since the data from the three FIs are nearly identical, we merged the individual spectrum to improve the photon statistics. The background-subtracted full-band spectra are shown in figure 6.6.

At first, we divide the spectra into narrow energy bands and study the plasma characteristics in relation to the various elements.

6.3.1 The 4–10 keV Band Spectrum

In order to determine the center energy of an Fe-Kα line, we first fitted the 4–10 keV spectra with a power-law (for the continuum) and a Gaussian (for the emission line). The best-fit centroid of the Fe-K line was obtained to be 6436 (6406–6466) eV.

We then fitted the spectra with a solar abundance (Anders & Grevese 1989) VNEI model. If

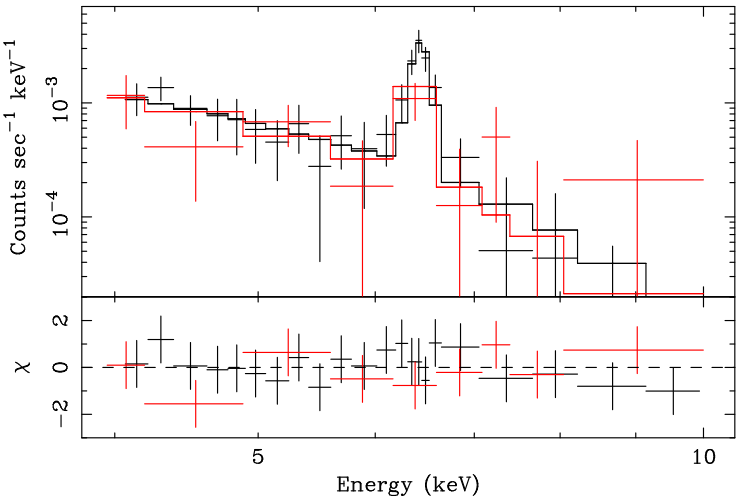

Fig. 6.4.—: XIS spectra in the 4–10 keV band fitted with the VNEI model. Black and red data points represent the FI and BI spectra, respectively.

we fix the Fe abundance to be solar, the model cannot reproduce the Fe-Kα profile and returns an unacceptable χ^2/d.o.f. of 52/28. Allowing the Fe abundance to be free, the fit was greatly improved with best-fit χ^2/d.o.f. of 14/27. The best-fit kT_e, n_et, and Fe abundance are 3.2 (2.5–9.0) keV, 7.1 (1.5–13) $\times 10^9$ cm^{-3} s, and 18 (>7.1) solar, respectively. Since the Fe abundance is significantly enhanced relative to the solar value, we can conclude the Fe-K emission originates from the ejecta heated by a reverse shock. The best-fit spectrum is shown in figure 6.4.

6.3.2 The 1.1–4.0 keV Band Spectrum

We can see, in the 1.1–4.0 keV band spectra, strong Kα lines of Si and S as well as Kβ of these elements and Kα of Mg, Ar, and Ca. We ignored the data in 1.83–1.85 keV because of the same reason as noted in subsection 5.4.3 (calibration issue). First, we fitted the 1.1–4.0 keV spectra with one-component VNEI model. Since K-shell emission lines from Ar are not included in the NEIvers 1.1 spectral code, we added a Gaussian at ~ 3.1 keV. (The center energy of the line was fixed but tuned to obtain a best-fit.) In this narrow band fitting, interstellar absorption was fixed to a hydrogen column density of 6.5×10^{20} cm^{-2}, which is close to the value obtained by Warren & Hughes (2004). Then, the best-fit χ^2/d.o.f. obtained was an unacceptable value of 920/350. Although we tried to fit the spectra with one-component VPSHOCK model, this model also failed to fit with χ^2/d.o.f. value of 696/350. The results of the VNEI and VPSHOCK fits are summarized in table 6.1, while the spectra fitted with the one-component VNEI are shown in figure 6.5a.

The most remarkable disagreement between the data and model (in figure 6.5a) is found in the center energy of the S-Kα line (around ~ 2.45 keV); the center energy predicted by the model is significantly lower than that of the data. In the 1.1–4.0 keV band, the most prominent emission

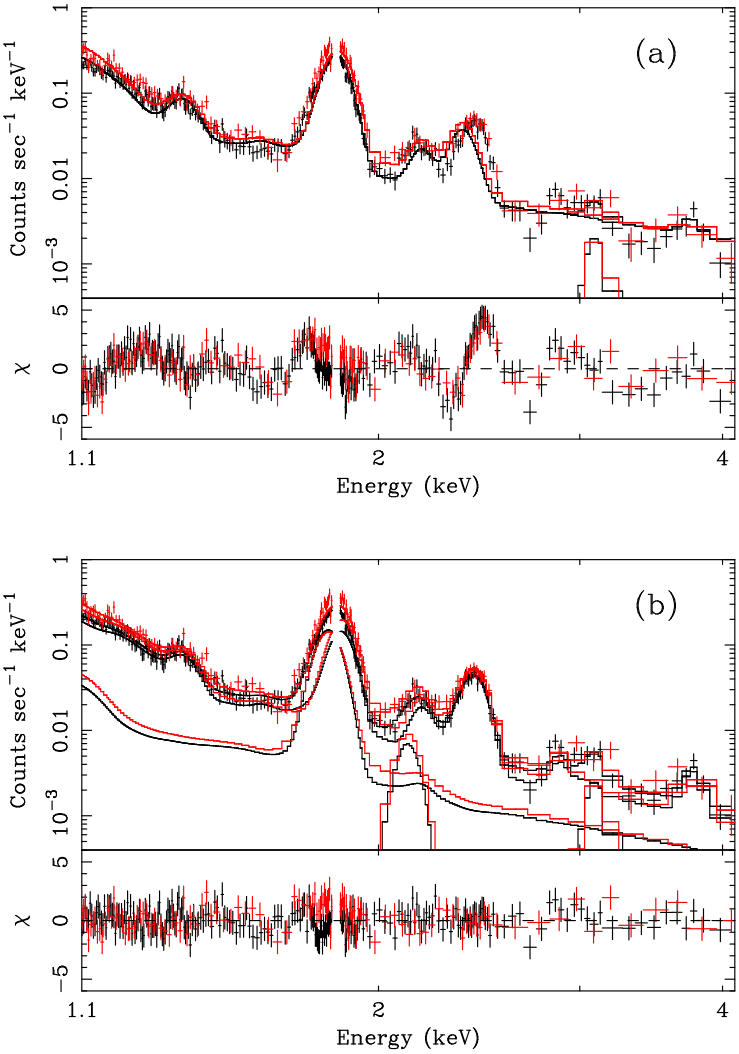

Fig. 6.5.—: (a) The XIS spectra in the 1.1–4.0 keV band fitted with the one-component VNEI model. The black and red data points represent the FI and BI spectra, respectively. A Gaussian at 3.1 keV is added in order to represent the Ar-K line which is not included in the VNEI model. (b) The same to (a) but fitted with the two-component VNEI model. A Gaussian at 2.12 keV is also added to represent the Kβ emission line from low-ionized Si.

Table 6.1:: Best-fit parameters of the spectral fittings in the 1.1–4.0 keV band with one-component VNEI and VPSHOCK models.

Parameter	VNEI	VPSHOCK
kT_e (keV)	2.2	1.6
Mg	0.51	0.40
Si	14	10
S	6.7	8.5
Ca	5.3	8.5
$n_e t$ (cm^{-3} s)	7.6×10^9	1.7×10^{10}
χ^2/d.o.f.	920/350 = 2.63	696/350 = 1.99

Table 6.2:: Best-fit parameters of the spectral fitting in the 1.1–4.0 keV band with 2-component VNEI model with different $n_e t$ values.

Parameter	Component 1	Component 2
$N_{\rm H}$ (cm^{-2})	6.5×10^{20} (fixed)	
kT_e (keV)	1.6 (1.5–1.7)	
Mg	0.37 (0.32–0.40)	0 (fixed)
Si	5.2 (4.9–5.5)	25 (24–27)
S	14 (13–15)	0 (fixed)
Ca	6.7 (4.5–9.3)	0 (fixed)
$n_e t$ (cm^{-3} s)	1.7 (1.6–1.8) $\times10^{10}$	4.0 (3.7–4.2) $\times10^{9}$
$n_{\rm H} n_e V$ (cm^{-3})	1.40 (1.37–1.44) $\times10^{58}$	5.96 (5.68–6.30) $\times10^{57}$
Gaussian lines to compensate for the incompleteness of the VNEI code		
Line	Center Energy(keV)	Norm (photons cm^{-2}s^{-1})
Si-Kβ*	2.12	3.4 (2.3–4.6) $\times10^{-6}$
Ar-Kα	3.10	1.7 (1.0–2.4) $\times10^{-6}$
χ^2/d.o.f.	328/346 = 0.95	

*Kβ line from low-ionized Si (lower than He-like).

line is Si-Kα, and hence the best fit value of $n_e t$ is mainly determined by the center energy of this line. Therefore, this disagreement suggests that the mean ionization age ($n_e t$) of Si is lower than that of S.

In subsection 5.4.3, we have shown the middle band (1.2–2.8 keV) spectrum of SN 1006 can be well fitted with the two-component VNEI model which has the common electron temperature but different $n_e t$ values. Here, we applied the same method and tried to fit with a two-component VNEI model. Then, the fitting was greatly improved with acceptable χ^2/d.o.f. value of 354/344. Although the good fit was obtained with this two-component model, we found a data excess still

remaining around the energy of 2.12 keV. We considered this excess is due to a Kβ emission from low-ionized Si, because the NEIvers 1.1 spectral code lacks the Kβ emission line from Si whose ionization state is lower than He-like. Therefore, we added a Gaussian at 2.12 keV (the best-fit center energy was fine-tuned) and fitted again. The best-fit parameters and spectra are given in table 6.2 and figure 6.5b, respectively. Note that although we first treated the abundances of Mg, Si, S, and Ca in both components as free parameters, all of them in the lower-n_et component (Component 2, in table 6.2) did not need significant values, except the Si abundance. Therefore, we finally fixed the abundance of Mg, S, and Ca of the lower-n_et component to 0. The χ^2/d.o.f. value (328/346) was significantly reduced from the result without the additional Gaussian at 2.12 keV. Moreover the intensity ratio of the 2.12 keV Gaussian to the Si-Kα in the lower-n_et component is $\sim 7\%$ (see figure 6.5b), which is a suitable value for the Kβ/Kα ratio for the Si in the low ionization state.

6.4 Broadband Spectrum

In section 6.3, we separately derived spectral parameters for the energy bands including K-shell emissions of intermediate-mass elements (Mg, Si, S, Ar, and Ca) and heavy element (Fe). The summary is listed in table 6.3. We did not try to fit the O-Ne band spectrum in the previous section, because the E0509–67.5 spectrum shows very weak K-shell lines from light elements (O and Ne) differently from the spectrum of SN 1006. We use these parameters as the initial values to search for the plasma parameters in the entire XIS energy band of 0.4–10 keV.

Based on table 6.3, we assume the model that describes the full spectral range must consist of, at least, two plasma components with (1) high-n_et ($\sim 2\times10^{10}$ cm^{-3} s) and (2) low-n_et ($\sim 4\times10^{9}$ cm^{-3} s). As shown in table 6.2, the component (1) is significantly enhanced in Si, S, and Ca, relative to solar. This fact suggests that these elements originate from the ejecta of the SNR. Therefore we make an assumption that this component is composed purely of metals without hydrogen and helium. We fixed the oxygen abundance of the component (1) to a large value (1×10^4) and determined the abundances of other elements relative to oxygen with a fitting. The C and Ni abundances were assumed to be the same as Ne and Fe, respectively. As already noted in section 5.5, the emission measure (EM) in the plasma code is defined (in XSPEC) as

Table 6.3:: Plasma components determined from the narrow band spectra.

Band (keV)	Major elements	kT_e (keV)	n_et (cm^{-3} s)	Component*
1.1–4.0	Mg, Si, S, Ca	1.6 (1.5–1.7)	1.7 (1.6–1.8)$\times10^{10}$	(1)
	Si	1.6 (1.5–1.7)	4.0 (3.7–4.2)$\times10^{9}$	(2)
4–10	Fe	3.2 (2.5–9.0)	7.1 (1.5–13)$\times10^{9}$	(2)

*The plasma component identifications described in text.

$n_{\rm H} n_e V$ even if the plasma is dominated by heavy elements. The oxygen density can be calculated as $n_{\rm O} = (8.51 \times 10^{-4} n_{\rm H}) \times 10^4$, where the numerical value is the solar abundance of oxygen from Anders & Grevesse (1989). The component (2), on the other hand, is enhanced in Si and Fe only. Therefore, we assume that this component is composed purely of Si, Fe, and Ni without any other heavy elements as well as hydrogen and helium. (Although there are no apparent feature of Ni K- and L-shell lines, we make the same assumption to component (1); the Ni abundance is equal to the Fe.) We thus fixed the Si abundance of the component (2) to 1×10^6 and fitted for the abundance of Fe (and Ni) relative to Si. The abundances of the other elements are fixed to 0.

Warren & Hughes (2004) concluded the continuum flux is not dominated by hydrogen thermal bremsstrahlung radiation but non-thermal synchrotron emission, since an ambient density ($n_{\rm H} \lesssim 0.05$ cm^{-3}) derived from the dynamical state of the remnant is too low to contribute to the continuum flux. We, here, follow their conclusion, and hence included a power-law component for the continuum and fitted the spectra in the energy band from 0.4 to 10 keV. With the same reasons as noted in subsection 6.3.2, we added Gaussians at 2.12 keV (for Si-Kβ) and 3.10 keV (for Ar-Kα).

With this model, the best-fit χ^2/d.o.f. was obtained to be an unacceptable value of 1131/719. We found the most remarkable disagreement between the data and model around 0.73 keV. In subsection 5.4.2, we found in the SN 1006 spectrum the disagreement at this energy as well, and pointed out this was plausibly due to the higher K-shell transitions of O VII (i.e., Kδ, ϵ, ζ, etc.), which were not included the spectral code we used. In the case of the E0509–67.5 spectrum, however, the same explanation cannot be applied because of the weak intensity of O VII series. Therefore we concluded this disagreement is purely due to Fe L-shell emission and added a single Gaussian at 0.73 keV (the best-fit energy is fine-tuned) in order to compensate for the incompleteness of the spectral code. Warren & Hughes (2004) also found the 0.73 keV enhancement in the Chandra ACIS spectrum of E0509–67.5 and pointed out the necessity of adding a separate Gaussian component. Then, the fit with the additional Gaussian was significantly improved with χ^2/d.o.f. = 789/718. The best-fit parameters and the full band spectra fitted with the best-fit model are given in table 6.4 and figure 6.6, respectively.

Table 6.4:: Best-fit parameters of the broadband spectral fitting.

Component	Parameter		Value
Absorption	$N_{\rm H}$ (cm^{-2})		5.8 (4.6–7.6) $\times 10^{20}$
VNEI 1 (Ejecta 1)	kT_e (keV)		3.7 (2.6–4.2)
	Abundance (10^4 solar)	C	1.4* (1.2–1.5)
		N	0 (fixed)
		O	1.0 (fixed)
		Ne	1.4* (1.2–1.5)
		Mg	0.92 (0.77–1.1)
		Si	17 (16–19)
		S	35 (33–40)
		Ca	16 (13–20)
		Fe	2.0† (1.8–2.1)
		Ni	2.0† (1.8–2.1)
	$n_e t$ (cm^{-3} s)		1.4 (1.3–1.5) $\times 10^{10}$
	$n_{\rm H} n_e V$ (cm^{-3})		3.65 (3.48–3.84) $\times 10^{53}$
VNEI 2 (Ejecta 2)	kT_e (keV)		3.5 (3.3–3.8)
	Abundance (10^4 solar)	Si	100 (fixed)
		Fe	62‡ (52–85)
		Ni	62‡ (52–85)
	$n_e t$ (cm^{-3} s)		3.5 (3.1–3.6) $\times 10^{9}$
	$n_{\rm H} n_e V$ (cm^{-3})		1.45 (1.36–1.51) $\times 10^{53}$
Power-law	Γ		3.7 (3.5–3.8)
	Norm§ (photons cm^{-2} s^{-1})		3.7 (3.4–3.9) $\times 10^{-4}$
Gaussian lines to compensate for the incompleteness of the VNEI code			
Line	Center Energy(keV)		Norm (photons cm^{-2} s^{-1})
Fe-L blends	0.733		4.1 (3.7–4.4) $\times 10^{-4}$
Si-Kβ	2.12		3.0 (1.9–4.0) $\times 10^{-6}$
Ar-Kα	3.10		2.1 (1.5–2.8) $\times 10^{-6}$
χ^2/d.o.f.			789/718 = 1.10

*, †, and ‡ represent linked parameters.

§The differential flux at 1 keV.

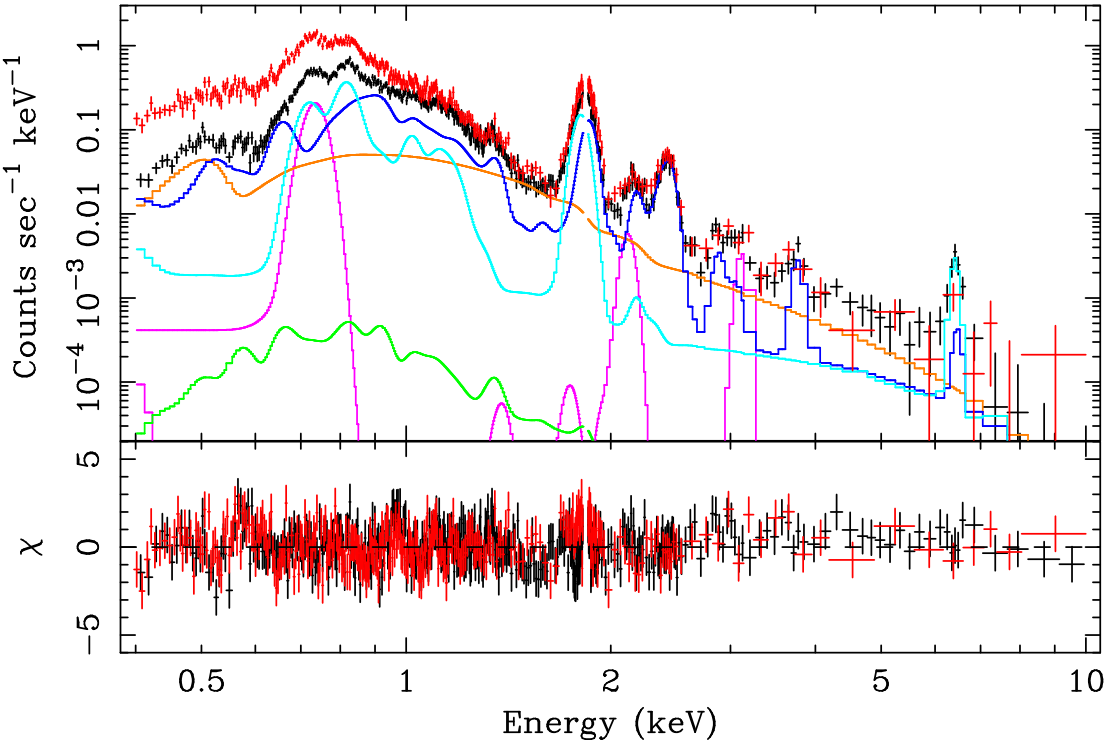

Fig. 6.6.—: XIS spectra of E0509–67.5 in the 0.4–10 keV band. The black and red data points represent the FI and BI spectra, respectively. The solid lines colored blue, light blue, orange, and magenta show the components of the Ejecta 1, Ejecta 2, Power-law, and additional Gaussians of the best-fit model for the FI spectrum. The green solid line indicates an estimated flux of an ISM component assuming the density of ambient medium to be 0.05 cm^{-3} (see text in subsection 6.5.3). kT_e, n_et, and a metal abundance of this component are assumed to be 1 keV, 1×10^{10} cm^{-3} s, and 0.3 solar, respectively. Note that this component is not included in the spectral fitting.

6.5 Discussion for E0509–67.5

In section 6.4, we analyzed the broadband spectrum of E0509–67.5, and found that it could be described with a parameterized model including two thermal plasmas in non-equilibrium ionization (VNEI 1 and VNEI 2, in table 6.4) and one power-law component (Power-law in table 6.4). In following, we discuss the implications of our spectral results.

6.5.1 Origin of the Components

Both of the thin-thermal plasmas, VNEI 1 and VNEI 2, are overabundant in heavy elements. Therefore we interpreted they have ejecta origin. Since VNEI 1 has a larger ionization parameter than the other, this plasma must be heated by the reverse shock in the early stage of the remnant evolution (hereafter Ejecta 1). On the other hand, VNEI 2 has relatively low ionization age. Therefore it should have been heated by the reverse shock very recently (hereafter Ejecta 2). We found that the Ejecta 2 consists of Si, Fe, and Ni only.

The Fe-K emission is mainly produced by the Ejecta 2 component (see figure 6.6), which suggests the mean ionization age of Fe is lower than the other elements (e.g., S and Ca) whose K-shell emission is purely produced by the Ejecta 1. This result differs from the Chandra result derived by Warren & Hughes (2004): the plasma consisting of the Fe ejecta has a higher ionization timescale (and a much higher electron temperature) than the other elements. They used the VPSHOCK spectral code for their fitting and obtained the best-fit kT_e and n_et for the Fe ejecta to be 10.0 keV and 3.4×10^{10} cm^{-3} s, respectively. However, we found these spectral parameters with the VPSHOCK model predicts the Fe-K energy centroid of 6489 eV, which is significantly higher than our result (6436 ± 30 eV: subsection 6.3.1). Because of its limited effective area, the Chandra spectrum has no sufficient photon statistics of Fe-K line (see figure 4 of Warren & Hughes 2004). Therefore, the ionization timescale for the Fe ejecta would be determined only from the profile of Fe-L blends, of which the atomic physics is not as well understood, and would be overestimated as the result.

The power-law component is most likely to be a synchrotron emission. The photon index of $\Gamma = 3.7$ ($3.5 - 3.8$) is almost consistent with the Chandra result of Warren & Hughes (2004). As shown in figure 6.2, the filamentary hard emission (blue) is found at the outermost of the remnant. It suggests the electrons are accelerated up to more than TeV energy at the blast wave of the remnant with a very high shock velocity ($\gtrsim 3600$ km s^{-1}: Tuohy et al. 1982), similarly to SN 1006 (Koyama et al. 1995, Bamba et al. 2003).

6.5.2 Relative Abundance and Mass of the Ejecta

The low abundances of O and Ne compared to those of intermediate-mass elements (i.e., Si and S) suggest E0509–67.5 is a product of a Type Ia SN. Therefore we compare our best-fit relative abundances with the predicted nucleosynthesis yield of the Type Ia SN deflagration model (W7

Table 6.5:: Mass of major elements in the ejecta for several assumed filling factors.

f *	0.5	0.8	0.9	0.95	0.99
O ($M_\odot$)	0.14	0.18	0.19	0.20	0.20
Si ($M_\odot$)	0.56	0.47	0.41	0.37	0.31
S ($M_\odot$)	0.19	0.24	0.26	0.27	0.27
Fe ($M_\odot$)	0.64	0.44	0.33	0.26	0.16
Total ($M_\odot$)	1.68	1.50	1.38	1.27	1.12

*Filling factor for the Ejecta 1.

model: Nomoto et al. 1984). The data points in figure 6.7a indicate the relative abundances in the Ejecta 1, while the solid line shows those of W7 model. Since the model does not reproduce our result well, we also compare the data with the delayed detonation model (WS15DD3 model) predicted by Iwamoto et al. (1999), which is shown as the dashed line in figure 6.7a. We can see the latter model has the better reproducibility of the abundance ratio between O, Mg, and S. However, the abundances of Si, Ca, and Fe relative to O are much lower than the predicted values. This result suggests these elements are concentrated on the inner layer of the remnant and hence did not heated enough in the early stage of the SNR evolution. Indeed, Si and Fe are enhanced in the Ejecta 2, which is interpreted as the ejecta heated more recently. Although the Ne abundance (relative to O) is much larger than the predicted value, note that it is not so reliable because the Ne K-shell lines (at the energies of 0.9–1.1 keV) are very weak and embedded in the Fe-L blends.

As shown in figure 6.2, E0509–67.5 has a clear shell-like structure. By the image fitting, Warren & Hughes (2004) determined the inner and outer radii of the shells to be 12.8 arcsec and 15.2 arcsec, respectively. These values correspond to $r_{\rm in} = 9.4 \times 10^{18}$ cm and $r_{\rm out} = 1.1 \times 10^{19}$ cm, from which we estimate the emission volume to be $V = 4\pi(r_{\rm in}^3 - r_{\rm out}^3)/3 = 2.4 \times 10^{57}$ cm^3. Here, we define the filling factor for the Ejecta 1 as f, and assume that for the Ejecta 2 as $(1-f)$. The mass (sum of Ejecta 1 and 2) of each major element for several values of f is estimated as shown in table 6.5. (Note that the elemental mass values do not depend on the assumed oxygen or silicon abundances relative to hydrogen.) The relative abundances for the several f are also shown in figure 6.7b.

If we assume $f \lesssim 0.8$, the estimated total mass of the ejecta exceeds the Chandrasekhar limit of a white dwarf. Therefore, the filling factor for the Ejecta 1 may larger than ~ 0.8. Then the Fe mass must be $\lesssim 0.4 M_\odot$, which is significantly lower than the predicted value of ~ 0.6–$0.8 M_\odot$ (e.g., Iwamoto et al. 1999). This result suggests a large amount of Fe ejecta still remain at the inner region of the remnant, and hence have not been heated by the reverse shock yet.

6.5.3 Contribution of the ISM

Differently from the result of SN 1006 (section 5.5), our best-fit model for the E0509–67.5 broadband spectrum does not need the contribution of an emission from the ISM heated by the

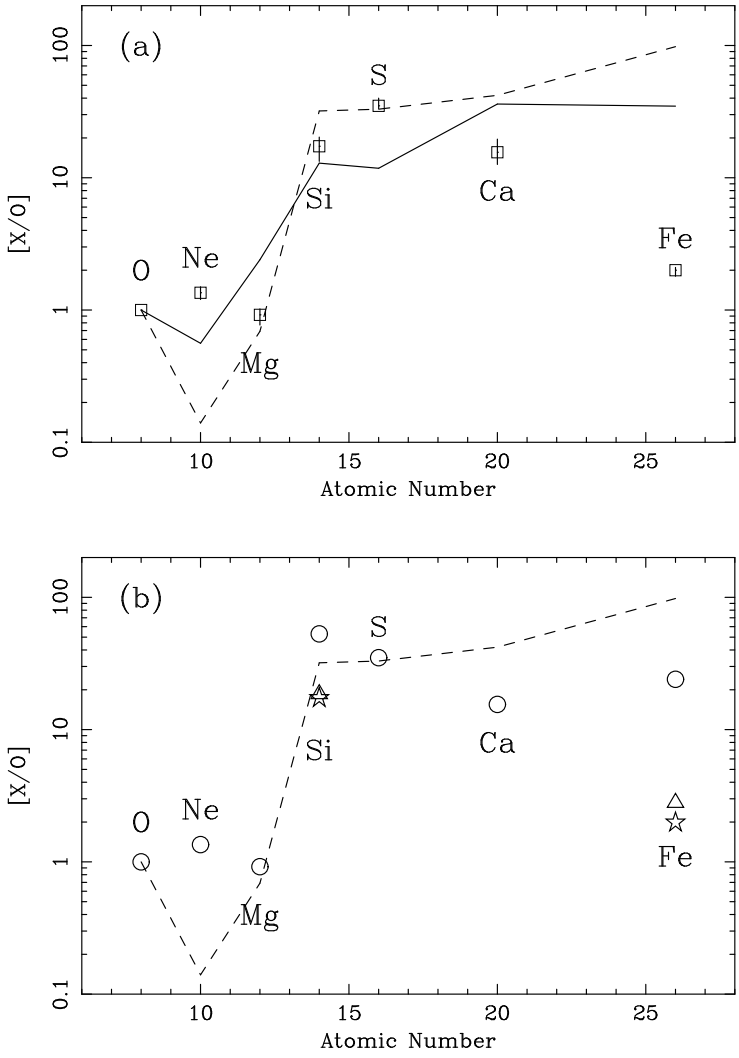

Fig. 6.7.—: (a) Metal abundances of the Ejecta 1 as a function of atomic number derived from the spectral fitting. The solid and dashed lines show the abundance relative to oxygen calculated in the W7 (Nomoto et al. 1984) and WS15DD3 (Iwamoto et al. 1999) models for a Type Ia supernova. (b) Abundance ratio for the sum of the Ejecta 1 and 2 , when the filling factor for the Ejecta 1 (see text) is assumed to be 0.5 (circle), 0.9 (triangle), and 0.99 (star). The dashed line is the same to (a).

blast wave. This result is consistent with Warren & Hughes (2004). Here, we estimate the flux of the ISM emission and compare it with that of the full-band spectrum. The optical studies constrained the density of the ambient medium to $n_{\rm H} \lesssim 0.02$ cm^{-3} (Tuohy et al. 1982). Furthermore, it was also confirmed by the X-ray study ($n_{\rm H} \lesssim 0.05$ cm^{-3}: Warren & Hughes 2004). If we assume that the ambient medium is homogeneous with the density of 0.05 cm^{-3}, the EM of the swept-up ISM is estimated to be 5.6×10^{55} cm^{-3}. The spectrum with this EM is shown as the green solid line in figure 6.6, assuming kT_e, n_et, and a metal abundance to be 1 keV, 1×10^{10} cm^{-3} s, and 0.3 solar (the abundance of the LMC: Dickey & Lockman 1990), respectively. The flux of this component is found to be much lower than the other components. Therefore, the contribution of the ISM emission is negligible relative to the whole SNR spectrum, independently of the actual kT_e and n_et values of this component.

6.5.4 Summary for E0509–67.5

We have analyzed the high-quality spectra of E0509–67.5 which is the youngest and the brightest SNR in the LMC, obtained with Suzaku. The results and interpretations are summarized as follows:

1. The spectrum can be described by a model with at least two NEI thermal plasmas and one power-law component.
2. The fits yield different ionization parameters of $n_et \sim 3.5 \times 10^9$ cm^{-3} s (low), and $n_et \sim 1.4 \times 10^{10}$ cm^{-3} s (high).
3. The Fe-K emission is mainly produced by the low-n_et plasma. The center energy of the Fe-Kα line is $\sim$ 6.44 eV.
4. The high-n_et plasma is overabundant in Si and S. However, the abundance of Fe is much lower than the predicted value for Type Ia SN ejecta.
5. The spectrum contains a power-law component with the photon index of $\Gamma \sim$3.7, suggesting that this component has a synchrotron origin.
6. The contribution of the emission from the swept-up ISM is much smaller than those of the other components.

Chapter 7

RCW 86

As shown in chapters 5 and 6, the ejecta in SN 1006 and E0509–67.5, which are evolving in thin ambient gas, have extremely low ionization ages. These facts suggest that progresses of heating and ionization processes in SNR ejecta are strongly influenced by the densities of the circumstellar matter. RCW 86, the oldest historical SNR, is known to be expanding in non-uniform ISM (spatial variation of the ambient density is quite large: e.g., Vink et al. 1997). Therefore, it is expected that the plasma ages of the ejecta are different from position to position even in one SNR. In this chapter, we summarize the results of Suzaku observation and analysis on RCW 86 northeastern shell, where the largest non-uniformity (in the entire SNR) of the ISM density is suggested. Unless otherwise stated, figures in this chapter are taken from Yamaguchi et al. (2008b), which this chapter mainly follows.

7.1 Previous Results

RCW 86 (G315.4–2.3) is one of the historical Galactic supernova remnants (SNRs), a possible remnant of supernova in AD 185 (Stephenson & Green 2002). It was first discovered by a radio survey observation (Mills et al. 1961). The energy index in radio band is measured by Caswell et al. (1975) to be $\alpha = 0.6$. Dickel et al. (2001) presented the imaging and polarimetry of this SNR at a frequency of 1.34 GHz with the Australia Telescope Compact Array (ATCA), and found that the southwest (SW) rim is colliding with dense gas just now. Figure 7.1 shows the 1.34 GHz radio contour (Dickel et al. 2001) of RCW 86 overlaid by Hα image (gray scale: Smith 1997). Their morphologies are different from each other. The distance to RCW 86 was determined to be 2.8 kpc by optical observations (Rosado et al. 1996); we assume this value in this chapter.

In X-ray band, RCW 86 was discovered by Naranan et al. (1977) with Apollo space-craft. A higher energy spectrum (2–20 keV) with the Ginga satellite was explained by a high temperature plasma of $kT_e \gtrsim 4$ keV (Kaastra et al. 1992). The ASCA observations discovered synchrotron X-rays from the SW and northeast (NE) shells of RCW 86 (Bamba et al. 2000; Borkowski et

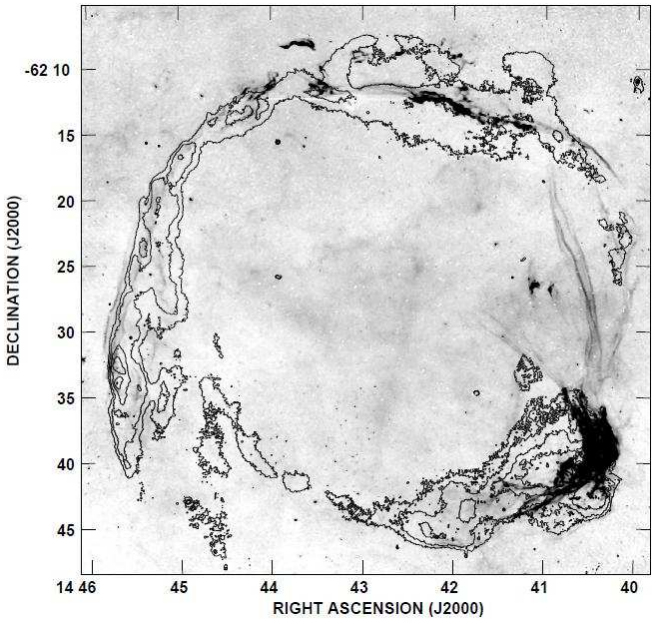

Fig. 7.1.—: 1.34 GHz radio contours and Hα gray scale (Smith 1997) of RCW 86. This picture is taken from Dickel et al. (2001).

al. 2001), which indicates that the energy of the electrons reaches up to ∼100 TeV by shock acceleration, similar to the mechanism in SN 1006 (Koyama et al. 1995). Another remarkable discovery with ASCA is the ∼6.4 keV line in the spectra of the SW (Vink et al. 1997) and NE rims (Tomida 1999) of RCW 86. Since the center energy of the line is consistent with Kα from neutral Fe, a fluorescent origin had often been proposed (Vink et al. 1997; Tomida 1999). However, Bamba et al. (2000) and Borkowski et al. (2001) showed that the X-ray spectrum of the SW shell could be represented by a three-component model; two thin-thermal plasmas with low (∼0.3–0.8 keV) and high (>5 keV) temperatures, and a non-thermal component. The Fe-Kα line was explained by the high-temperature plasma with an extremely low ionization parameter ($\tau = n_e t$) of $\sim 10^9$ cm^{-3} s.

Rho et al. (2002) observed the SW shell with Chandra, and spatially resolved the low-temperature plasma and non-thermal emission. Since the low-temperature plasma is spatially correlated with optical Hα emission, they concluded the origin to be a blast wave. On the other hand, the non-thermal emission is localized at the inner region of the low-temperature plasma; hence, the origin was suggested to be reverse shock. They found, furthermore, that the Fe-Kα emission correlated with the non-thermal emission, and suggested that the Fe-Kα line originates from a high-temperature plasma of Fe-rich ejecta heated by the synchrotron-emitting reverse shock. However, the morphology of the Fe-Kα emitting region could not be determined.

Recently, the SW region of RCW 86 was observed with Suzaku. Utilizing the good sensitivity and spectroscopic performances of the XIS in the energy band of Fe-K lines for diffuse sources (section 4.3), Ueno et al. (2007) determined the center energy of the Fe-Kα line to be

6404 (6400–6407) eV, which indicates the emission is from low-ionized iron less than Si-like (Fe XIII). Furthermore, they revealed the Fe-K line morphology for the first time and discovered its distribution is spatially different from that of the non-thermal emission. They thus confirmed that the origin of the Fe-Kα is not fluorescence caused by supra-thermal electrons, nor non-thermal X-rays, but concluded that a more likely origin is a high-temperature ejecta in an extremely ionization non-equilibrium.

The NE region of RCW 86 also exhibits an Fe K-shell emission (albeit the flux is less than that of SW) as well as the soft thermal and the non-thermal X-rays (ASCA: Tomida 1999). Therefore, this region would be another good place to solve the puzzle concerning the origin of the Fe-Kα related to the thermal and non-thermal emission in RCW 86. Chandra and XMM-Newton revealed that the soft-thermal and non-thermal emission filaments join smoothly along the outer shell (see figure 7.2; Vink et al. 2006). They, however, failed to detect Fe-Kα from this region, possibly due to the limited sensitivity and the high background level near the Fe K-shell energy. We therefore observed the NE shell with Suzaku to see if the Fe-Kα is really present or not. If present, we will study its morphology and spectra to reveal the origin.

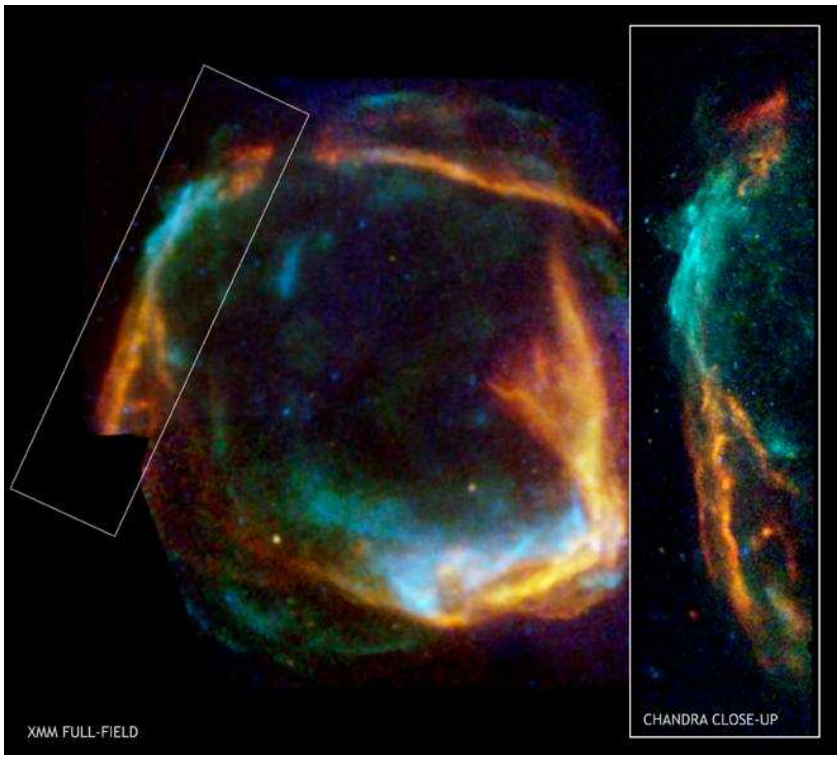

Fig. 7.2.—: Left: XMM-Newton image of RCW 86. Red, green, and blue represent 0.5–1.0 keV, 1.0–2.0 keV, and 2.0–6.6keV, respectively. North is up and east is to the left. Right: Chandra image of northeast rim (indicated with the white rectangle in the XMM-Newton image) of RCW 86. The color is same to the left. Credit: ESA/Univ. of Utrecht/Vink et al. (left), NASA/CXC/Univ. of Utrecht/Vink et al. (right).

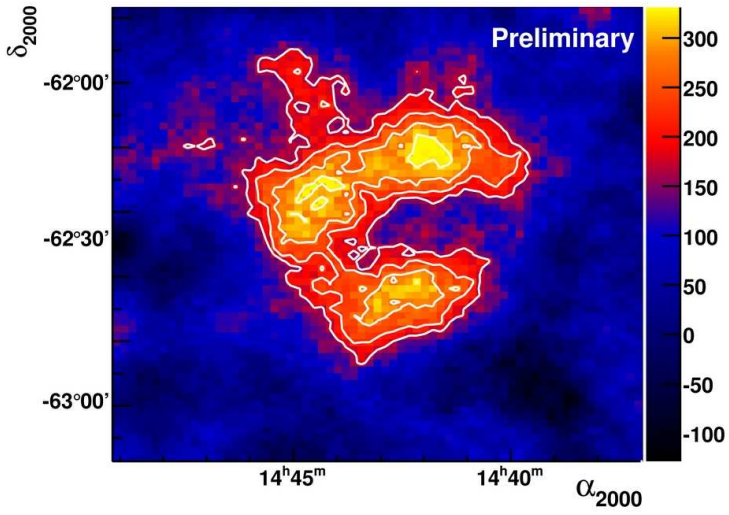

Fig. 7.3.—: HESS image of RCW 86, but a preliminary result. White contours correspond to 3, 4, 5, 6σ significance. This picture is taken from Hoppe et al. (2007).

Furthermore, TeV γ-rays from RCW 86 were detected by HESS very recently (figure 7.3: Hoppe et al. 2007). The morphology of the γ-ray emission was confirmed to be shell-like, similarly to RX J1713.7–3946 (Aharonian et al. 2007a) and RX J0852.0–4622 (Aharonian et al. 2007b). At present, the origin of the γ-ray is not determined to be hadronic or leptonic. The wide-band spectral studies of the non-thermal emission will help to reveal the origin.

7.2 Suzaku Observation

The Suzaku observation of the NE region of RCW 86 was made on 2006 August 12 (Observation ID = 501037010). The XIS were operated in the normal full-frame clocking with the 3×3 or 5×5 editing mode. We employed cleaned revision 1.2 data, and used the HEADAS software version 6.0.4 and XSPEC version 11.3.2 for the data reduction and analysis. After screening, the effective exposure time was obtained to be $\sim$53 ksec. The response matrix files (RMF) and ancillary response files (ARF) were made using `xisrmfgen` and `xissimarfgen` (Ishisaki et al. 2007) version 2006-10-17.

7.3 Analysis and Results

7.3.1 XIS Image

We show the Fe-Kα intensity map in figure 7.4 in gray scale. This map was made from the 6.3–6.5 keV (the Fe-Kα band) image by subtracting the continuum level in this band, which was estimated with a power-law model (with photon index of 3) fitting for the 5.0–6.2 keV continuum spectrum. For comparisons with the soft and hard X-ray fluxes, we overlaid intensity contours of the 0.5–1.0 keV band (figure 7.4 left) and the 3.0–6.0 keV band (figure 7.4 right). No spatial correlation between the Fe-Kα and the hard X-ray emission was found. Moreover, the soft X-ray emission is systematically shifted outward with respect to the Fe-Kα emission. As we show in subsection 7.3.3, the 0.5–1.0 keV emission is dominated by an optically thin-thermal plasma with an electron temperature of $\sim$0.3 keV, and the Ne IX-Kα line is the major emission of this component. We then made projection profiles of the Ne IX-Kα line band (0.87–0.94 keV), and the Fe-Kα band (6.3–6.5 keV), in the position given in figure 7.4 left. The result is shown in figure 7.5. We can see that the peak of Fe-Kα is significantly shifted to the inner region from the soft emission (Ne IX-Kα). With the fitting of a Gaussian-plus-constant model, the peak positions (right ascensions) of the soft plasma and Fe-Kα are found to be separated by 2 arcmin.

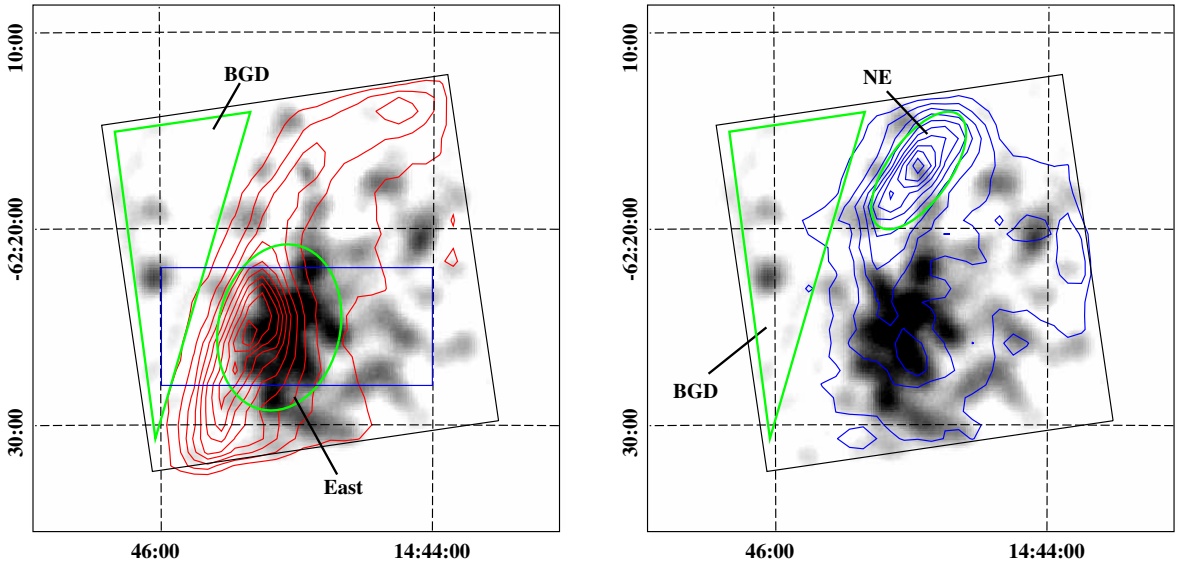

Fig. 7.4.—: 0.5–1.0 keV (left) and 3.0–6.0 keV (right) intensity contours overlaid on the Fe-K map (gray scale) smoothed with a Gaussian kernel of $\sigma = 1.1$ arcmin. The coordinates (RA and Dec) refer to epoch J2000.0. The Field of view of the XIS is indicated by the black squares, where the data from the four XIS are combined, but that of the four corners, irradiated by the ^{55}Fe calibration sources, are removed. The green ellipses and the triangles are the source and background regions, respectively. The blue rectangle indicates the region where the projection profiles are extracted (see figure 7.5).

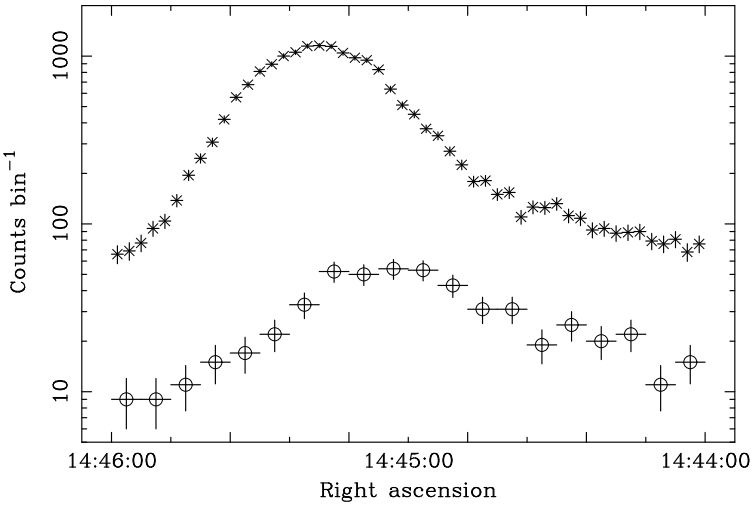

Fig. 7.5.—: The projection profiles (along Right ascension) of the Ne IX-Kα band (cross; 0.87–0.94 keV) and the Fe-Kα band (circle; 6.3–6.5 keV) for the blue rectangular region given in the left panel of figure 7.4. The bin-size of the former corresponds to $\sim 0.'28$, while that of the latter is $\sim 0.'69$.

7.3.2 Spectrum in the Hard X-Ray Band

For a quantitative study, we extracted the representative XIS spectra from two elliptical regions: the East and NE (see figure 7.4), where the soft X-ray and Fe-Kα, and the hard X-ray flux are the brightest, respectively. We did not divide the former two diffuse emissions because the separation between them is comparable to the angular resolution of the XRT ($\sim 2'$: see section 4.2), and they are overlapping each other. The solid angles of these ellipses are $\pi \times 4.'2 \times 3.'1 = 41$ arcmin^2 and $\pi \times 3.'5 \times 1.'6 = 18$ arcmin^2, respectively. The background data were taken from the outside of the remnant (the solid triangles in figure 7.4). For the background spectra, we excluded the point-like sources at (14:46:03, –62:22:30) and (14:46:03, –62:19:01), and the CCD corners which contain the ^{55}Fe calibration source.

We first determined the Fe-Kα line parameters. The background-subtracted spectra in the 3–10 keV band in the East region are shown in figure 7.6. Since the data from the three FIs are nearly identical, we merged the individual spectrum to improve the photon statistics.

We detected a clear Fe-Kα line in the spectra. We then fitted the spectra with a power-law (for the continuum) and a Gaussian (for the emission line). The best-fit parameters are given in table 7.1. The centroid energy of the Fe-Kα line is slightly higher than that of the emission line from neutral iron (6400 eV). Although the absolute energy calibration error is reported to be as accurate as $\pm 0.2\%$, above 1 keV (Koyama et al. 2007), we checked the energy scale of each XIS sensor using the ^{55}Fe calibration sources. We then confirmed that the peak energies of Mn-Kα lines were consistent with the laboratory value of 5895 eV within the statistical errors for all of the XIS sensors. We therefore conclude that the energy scale error in the Fe-K line band is less than the

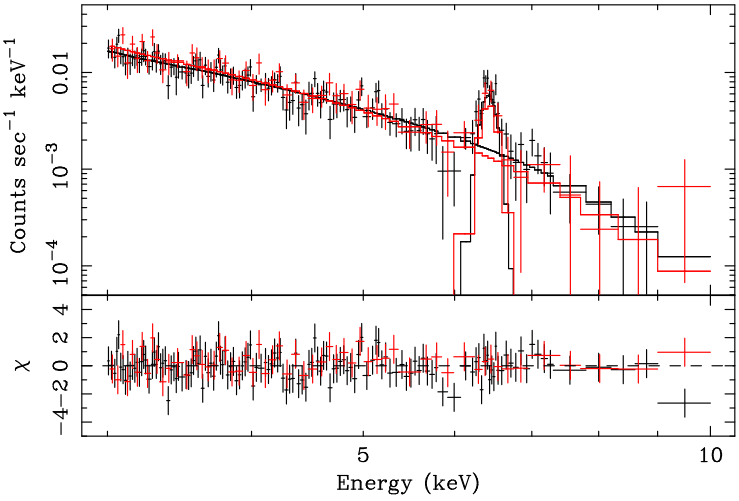

Fig. 7.6.—: XIS 3–10 keV spectra extracted from the East region. Black and red represent the FI (sum of the three sensors) and BI, respectively. The best-fit power-law and Gaussian models are shown by solid lines.

Table 7.1:: Best-fit parameters of 3–10 keV fittings.

Component	Parameter	East	NE
Power-law	Γ	3.18 (3.02–3.31)	2.96 (2.88–3.05)
	Flux*	1.10 (1.07–1.14) $\times10^{-4}$	2.44 (2.39–2.48) $\times10^{-4}$
	Surface brightness*	2.68 (2.61–2.78) $\times10^{-6}$	1.36 (1.33–1.38) $\times10^{-5}$
Gaussian	Center (eV)	6424 (6404–6444)	6424 (fixed)
	Width† (eV)	<90	0 (fixed)
	Flux‡	7.1 (5.8–8.3) $\times10^{-6}$	<8.1 $\times10^{-7}$
	Surface brightness‡	1.7 (1.4–2.0) $\times10^{-7}$	<4.8 $\times10^{-8}$
	χ^2/d.o.f.	146/192 = 0.76	204/234 = 0.87

* Photon flux (photons cm^{-2} s^{-1}) and surface brightness (photons cm^{-2} s^{-1} arcmin^{-2}) in the 3–10 keV band.

† One standard deviation (1σ).

‡ Total flux (photons cm^{-2} s^{-1}) and surface brightness (photons cm^{-2} s^{-1} arcmin^{-2}) in the line.

statistical error. The best-fit energy of 6424 (6404–6444) eV constrains the Fe ionization state to be approximately between Ar-like and Ne-like.

For a comparison, we extracted the spectra from the NE region in the same way as that of the East, and fitted the spectra with a power-law plus a Gaussian. Since we could see no clear the Fe-Kα line, we fixed the center of the Gaussian to be 6424 eV, and determined the upper limit of the line flux. The result is given in table 7.1. The surface brightness of the Fe-Kα and the power-law component in the NE are at least $\sim$3-times smaller and $\sim$5-times higher than those in the East region.

7.3.3 Full Band Spectrum

Figure 7.7 shows the 0.4–10 keV spectra from the regions of East and NE. The data reduction is the same as described in subsection 7.3.2. We can clearly see several emission lines below $\sim$2 keV in the East spectra. This suggests that the soft X-rays are dominantly from an optically thin thermal plasma. Therefore, we fitted the spectra from the East region with a thin-thermal plasma model and a power-law component. For the thermal plasma component, we used a VPSHOCK (variable abundance plane-parallel shock) model with the NEIvers 1.1 code (since the NEIvers 2.0 code does not include K-shell emission lines from low ionized Fe, we do not use this new version). Note that if we use a VNEI model which is used in the other chapters, the result and interpretation do not change essentially. We treated the abundances relative to solar (Anders and Grevesse 1989) to be free parameters, with the following elements in the parenthesis fixed to be the same: (C, N, and O), (Si and S), and (Ca, Fe, and Ni). The data in the 1.83–1.85 keV band were ignored because of the current calibration errors of the XIS; there is a small energy gap ($\sim$10 eV) at the Si K-edge that is not implemented in the current response function. Since the absolute gain of the XIS has an uncertainty (especially for low-energy X-rays), we allowed a small offset in the energy scale, independently between the FI and BI.

This 2-component model gives nice fits to the soft X-ray band including all the emission lines and the hard continuum emission with a best-fit kT_e value of the thermal component of 0.38 keV and a power-law index of 2.9. However it cannot reproduce the Fe-K line flux, with the unacceptable χ^2/d.o.f. of 1222/1054. As given in subsection 7.3.2, the center energy of the Fe-K line is slightly but significantly higher than that of Fe I, which suggests that the origin of the Fe-K line is due to a low ionized thin-thermal plasma, but is not the fluorescence of neutral Fe. We hence added another thin-thermal component with a higher temperature and a low ionized parameter. The abundances in this plasma were fixed to solar, except for Fe. Then, the best-fit χ^2/d.o.f. was significantly reduced to be 1093/1050. The best-fit parameters and models are respectively shown in table 7.2, and in figure 7.7 with solid lines.

We next fitted the spectra of the NE region. We can see emission lines in the soft X-ray band in these spectra. This suggests that the NE also includes a low-temperature plasma. However, the line profiles are too weak to obtain a reasonable fit with many free parameters of the low-temperature plasma. We therefore fixed the soft plasma parameters as those of the East region.

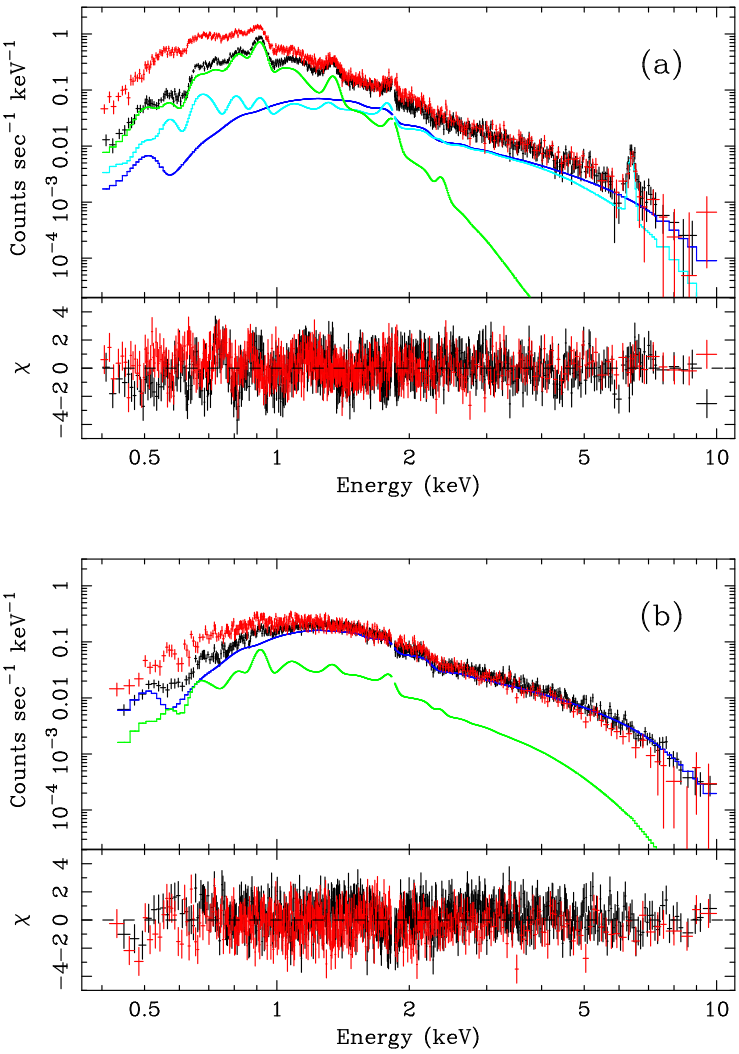

Fig. 7.7.—: (a) 0.4–10 keV spectra of the East region. Black and red represent the FI and BI, respectively. The components of the best-fit model for the FI are shown with the solid lines: green, light blue, and blue are respectively low-temperature plasma (VPSHOCK 1 in table 7.2, high-temperature plasma (VPSHOCK 2 in table 7.2), and power-law. (b) the spectra of the NE region. The colors are same to (a). Since these spectra have no significant Fe-K line, the high-temperature plasma component did not be added.

Table 7.2:: Best-fit parameters of full-band model fittings.

Component	Parameter	East	NE
Absorption	$N_{\rm H}$ ($\rm cm^{-2}$)	4.1 (3.8–4.4) $\times 10^{21}$	4.4 (4.2–4.5) $\times 10^{21}$
VPSHOCK 1	kT_e (keV)	0.33 (0.30–0.37)	1.2 (0.89–1.6)
	C, N, O	0.15 (0.11–0.24)	0.15 (fixed)
	Ne	0.33 (0.26–0.50)	0.33 (fixed)
	Mg	0.31 (0.28–0.48)	0.31 (fixed)
	Si, S	0.31 (0.19–0.43)	0.31 (fixed)
	Ca, Fe, Ni	0.23 (0.17–0.36)	0.23 (fixed)
	τ ($\rm cm^{-3}$ s)	7.7 (5.5–11) $\times 10^{10}$	6.7 (5.9–7.7) $\times 10^{9}$
	$n_e n_{\rm H} V$ ($\rm cm^{-3}$)	3.7 (2.4–5.8) $\times 10^{57}$	2.4 (2.0–2.9) $\times 10^{56}$
VPSHOCK 2	kT_e (keV)	1.8 (1.4–2.3)	–
	Fe	32 (14–90)	–
	τ ($\rm cm^{-3}$ s)	2.3 (1.8–2.9) $\times 10^{9}$	–
	$n_e n_{\rm H} V$ ($\rm cm^{-3}$)	2.0 (1.1–2.6) $\times 10^{56}$	–
Power-law	Γ	2.89 (2.45–3.28)	2.78 (2.74–2.82)
	Norm*	1.1 (0.72–1.9) $\times 10^{-3}$	3.3 (3.2–3.5) $\times 10^{-3}$
Gain (FI)	Offset (eV)	–3.2	–3.2
Gain (BI)	Offset (eV)	–5.4	–5.4
χ^2/d.o.f.		1093/1050 = 1.04	1138/1084 = 1.05

* The differential flux (photons $\rm cm^{-2}$ $\rm s^{-1}$) at 1 keV.

Since no Fe-Kα was found (see subsection 7.3.2), we did not include the thermal component with higher temperature. Thus, normalizations of the low-temperature plasma and power-law component are free parameters. To obtain the best-fit, we also fine-tuned a temperature and an ionization parameter in the low-temperature plasma and the photon index in the power-law component. The best-fit χ^2/d.o.f. is an acceptable value of 1138/1084. The best-fit parameters and spectra are given in table 7.2 and figure 7.7.

The thermal plasma parameters derived for the NE differ from the values reported by Vink et al. (2006); we find a higher τ and a lower kT_e. Indeed, kT_e and τ are correlated in the sense that both a higher kT_e or a higher τ give a higher ionization. Note that Vink et al. (2006) used a different spectral fitting code (SPEX). Both fits agree about the ionization state of the plasma, but differ concerning the relative contributions of kT_e and τ. For the NE region, the exact value for kT_e is difficult to determine, since most of the continuum has a non-thermal origin.

7.4 Discussion for RCW 86

From morphology and spectral analyses, the X-rays in the northeastern quadrant of RCW 86 can be separated into three distinct components: the low temperature (VPSHOCK 1) and high temperature (VPSHOCK 2) thermal components both in ionization non-equilibrium, and the power-law component. We separately discuss the origin of these components, and finally try to give a unified picture about them.

7.4.1 Low Temperature Plasma

As shown in figures 7.4 and 7.5, the soft X-rays are dominated in the outer shell of the East region. The spectrum is well represented by a thin-thermal plasma with a low temperature of $kT_e \sim 0.3$ keV. Since the Hα filament was reported to be localized near at the East region (figure 7.1: Smith 1997), the low-temperature plasma (VPSHOCK 1) is likely to be due to the interstellar medium (ISM) heated by a blast wave.

The metal abundances that we obtained are significantly lower than the solar values. A sub-solar abundance is also reported in the rim region of the Cygnus Loop (e.g., Miyata et al. 2007), where an ISM component is dominant. Therefore, shocked ISM spectra may generally show such low abundances. In the case of RCW 86, Bocchino et al. (2000) found the thermal spectra of the southeast and north rim show lower metal abundances than the solar values, and claimed that this result is due to metal depletion behind the shock. Since the abundances of our result are almost consistent with those of Bocchino et al. (2000), the same interpretation would be accepted. However, we should note that the complexity of our three-component model makes it difficult to determine the absolute values of the abundances. Indeed, if we fix the Ne abundance to be the solar, and fit the full band spectra of the East region, the best-fit can be obtained with an acceptable χ^2/d.o.f. (1103/1051), and almost the same relative abundances to those of table 7.2. An exact separation of the low and high-temperature components and the power-law component is necessary for a certain determination of the absolute metal abundances.

The solid angle of the East ellipse in figure 7.4 (= 41 arcmin^2) corresponds to 2.5×10^{38} cm^2 at 2.8 kpc. Assuming the depth of the emitting region to be 8.5 pc, about half of the radius of the remnant, the emission volume is estimated to be $V = 6.6 \times 10^{57}$ cm^3. Therefore, the emission measure ($EM = n_e n_{\rm H} V$) of the VPSHOCK 1 in this region corresponds to a proton density of $n_{\rm H} = 0.68\ f_{E1}^{-0.5}$ cm^{-3}, where f_{E1} is the filling factor for this component. Since the soft thermal emission concentrates at the outer thin rim in the East ellipse (see figure 7.4), the density of the low-temperature plasma is likely to be much larger than 0.68 cm^{-3}.

Similarly, the density of the VPSHOCK 1 in the NE region is estimated to be $n_{\rm H} = 0.26\ f_{N1}^{-0.5}$ cm^{-3}, where f_{N1} is the filling factor for the VPSHOCK 1 in the NE. Although several uncertainties remain (e.g., the filling factors, the temperature difference between the East and NE), the density of the swept-up ISM may be larger at the East rim than at the NE rim. The variation of the ionization parameter is consistent with this result, namely $\tau(= n_e t)$ in the East is

larger than that of the NE.

7.4.2 Fe-K Line and High Temperature Plasma

By imaging (subsection 7.3.1) and spectral (subsection 7.3.2) analyses, we proved that the Fe-Kα emission has no correlation with the hard X-ray continuum. Therefore, the origin of the Fe-Kα line is not due to fluorescence caused by supra-thermal electrons, nor non-thermal X-rays. It is located behind the blast wave (VPSHOCK 1) and is over-abundant in Fe. We hence propose that the origin of a high-temperature plasma (VPSHOCK 2) is a Fe-rich ejecta heated by a reverse shock.

The ionization parameter in VPSHOCK 2, determined from the center energy of Fe-Kα, is extremely low, $\tau \sim 2.3 \times 10^9$ cm^{-3} s. The electron density of the ejecta component is estimated to be $n_e = 0.19\ f_{E2}^{-0.5}$ cm^{-3}, where f_{E2} is the filling factor for the VPSHOCK 2 in the East region. We then estimate the elapsed time since the ejecta was heated by the reverse shock: $t = \tau/n_e = 1.2 \times 10^{10} f_{E2}^{0.5}$ sec $\lesssim 380$ yr. This is much less than the age of $\sim$1800 yr (from the historical record), and hence the ejecta must have been heated very recently.

The estimated mass of Fe is $\sim 0.07 f_{E2}^{0.5} M_\odot$, which is reasonable as a portion of the ejecta, and some of the Fe-ejecta may still remain in the interior of the remnant, which has not yet been heated by the reverse shock. However, we have to note the uncertainty in the mass determination. Although we show in subsection 7.3.3 that the spectrum of the East region is well reproduced by the three-component model, we cannot conclude this model is unique. We therefore, estimated the systematic error on the Fe mass by fitting the 3–10 keV spectrum with (1) only one VPSHOCK model (without a power-law), or (2) a pure Fe plasma and a power-law. In both cases, we fixed the values of kT_e and τ to 1.8 keV and 2.3×10^9 cm^{-3} s, the best-fit parameters given in table 7.2.

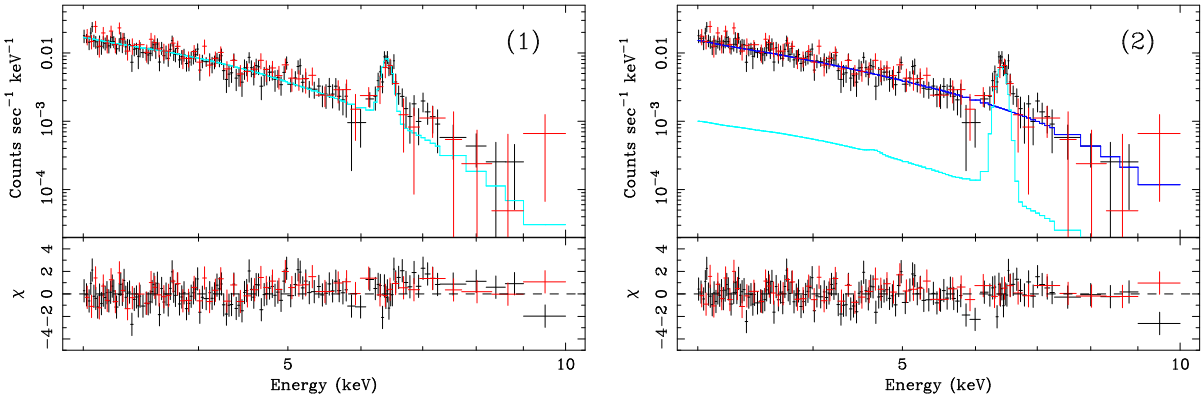

Fig. 7.8.—: 3–10 keV spectra of the East region fitted with only one VPSHOCK component (1), and a pure Fe plasma VPSHOCK and a power-law (2). The colors are same to figure 7.7. The Fe mass is estimated to be $0.06 f_{E2}^{0.5} M_\odot$ and $0.6 f_{E2}^{0.5} M_\odot$ for cases of (1) and (2), respectively.

The best-fit spectra for both cases are shown in figure 7.8. The Fe mass was, then, obtained to be $0.06 f_{E2}^{0.5} M_{\odot}$ and $0.6 f_{E2}^{0.5} M_{\odot}$ for cases of (1) and (2), respectively. These values can be regarded as the lower and upper limits of the Fe mass in the East region. Thus, there is an uncertainty of one order of magnitude.

7.4.3 Non-Thermal Emission

Since the non-thermal X-rays are well represented by a power-law with photon indices of ~ 2.8, synchrotron radiation is the most plausible origin. The synchrotron filament of the NE rim is spatially connected from the soft thermal rim (the East) along the outer shell of RCW 86 (see figure 7.2). Therefore, this filament may be produced by the blast wave.

In the case of the SW rim of RCW 86, Rho et al. (2002) and Ueno et al. (2007) suggested that the non-thermal filament is not a blast wave, but reverse shock, because the non-thermal filament is inside the soft thermal emission on the SNR shell. Also the blast-wave velocity at the SW shell ($\sim$800 km s^{-1}: Rosado et al. 1996; $\sim$600 km s^{-1}: Ghavamian et al. 2001) is too slow to accelerate electrons by the standard diffusive shock acceleration theory, and to emit intense synchrotron X-rays. Since the gas density of the NE shell is $\sim$10-times lower than that of the SW shell (Pisarski et al. 1984), it is possible that the velocity of the NE blast wave is much higher than that of the present SW shell. Vink et al. (2006) interpreted that the velocity of the NE non-thermal filament should be $\sim$2700 km s^{-1}. This high speed can accelerate electrons to more than TeV energy to produce synchrotron X-rays in the blast wave shock.

7.4.4 Unified Picture for All the Components

We propose a unified picture to explain all of the results in figure 7.9. A few hundred years ago, blast waves in the East and NE rims would be expanding with the same high velocity. However the blast wave in the East collided with a dense medium very recently, and the forward shock decelerated rapidly. At that same time, the reverse shock behind the East rim began to move inward to the interior of the remnant, and it heated the Fe-rich ejecta. Since RCW 86 may be a remnant in the OB association (Westerlund 1969), a candidate for the "dense medium" is either a cavity wall surrounding the remnant, as suggested by Vink et al. (1997), or a molecular cloud. We found in the NANTEN results (Matsunaga et al. 2001) evidence of a cloud just at the position of the East rim of RCW 86 (l=315.7, b=–2.4), as shown in figure 7.10. We strongly propose a deeper radio observation to reveal whether the shell of the remnant is truly interacting with the cloud.

The forward shock in the NE rim, on the other hand, is still expanding in a tenuous region, and hence keeps a high shock velocity. The reverse shock behind the NE may also expand with high velocity, and hence has not yet reached the Fe-rich ejecta layers. This may explain the absence of Fe-K emission behind the NE region.

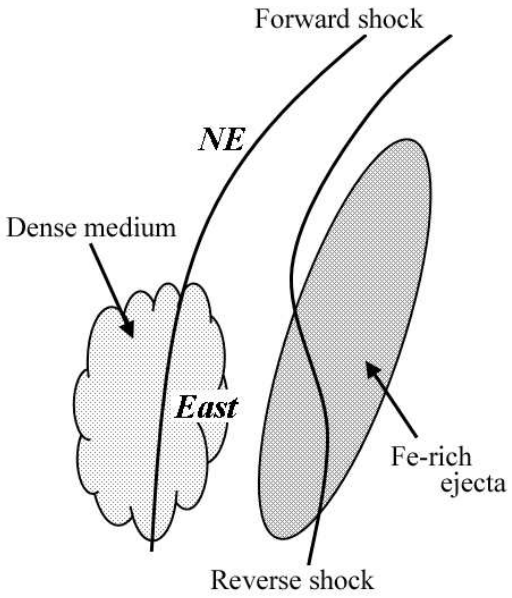

Fig. 7.9.—: Schematic view of the interpreted structure of RCW 86 NE region.

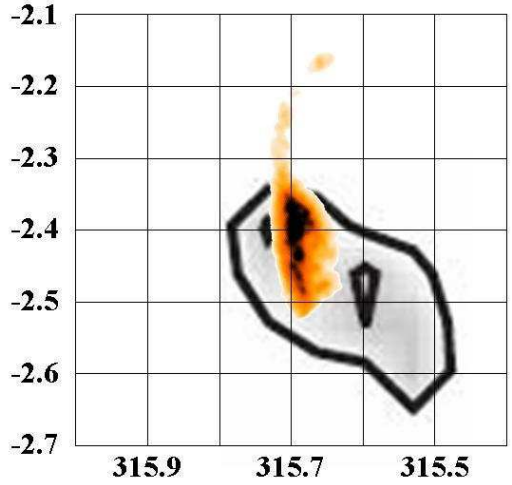

Fig. 7.10.—: NANTEN CO (J = 1–0) map of the RCW 86 northeast region (gray scale: Matsunaga et al. 2001), and XIS 0.5–1.0 keV image (color), shown in Galactic coordinates.

7.4.5 Summary for RCW 86

We have analyzed Suzaku/XIS data obtained from the northeast quadrant of RCW 86. The results and interpretations are summarized as follows:

1. The Fe-Kα emission is enhanced at the inner region from the soft thermal rim (the East region), and has no correlation with the hard X-ray non-thermal filament (the NE region).
2. The centroid of the Fe-Kα line (6404–6444 eV) and the lack of Fe-L lines constrain the Fe ionization state to be approximately between Ar-like (Fe IX) and Ne-like (Fe XVII).
3. The spectra extracted from the soft X-rays and Fe-Kα enhanced region (the East) are well fitted with two thin-thermal plasmas, which have different temperature of $kT_e \sim 0.3$ keV and ~ 1.8 keV and one power-law with a photon index of $\Gamma \sim 2.9$.
4. The spectra extracted from the hard X-ray filament (the NE) can be represented by a lower temperature plasma and a power-law.
5. The lower temperature plasma has sub-solar metal abundances. The origin of this component would be a blast-shocked ISM.
6. The higher temperature plasma includes an over-solar abundant iron, and has an extremely low plasma age of $\tau = n_e t \sim 2.3 \times 10^9$ cm^{-3} s. Hence it produces nearly 6.4 keV Kα lines. This component may be Fe-rich ejecta heated by reverse shock very recently.
7. The power-law component, which is the brightest in the NE region, can be regarded as synchrotron emission.
8. The shock front at the East rim would recently have collided with dense ISM, after which the blast wave decelerated rapidly, and the reverse shock began to move toward the center of the remnant.
9. The blast wave at the NE rim may still be expanding in a tenuous region. Therefore, it keeps a high shock velocity for efficient particle acceleration.

Chapter 8

Fe-K Emission in Other SNRs

In this chapter, we analyze the Suzaku data of Tycho and N103B, which are also young but slightly more evolved than the SNRs discussed in the previous chapters. Since both of Tycho and N103B show very strong emission lines, their spectral properties and morphologies of the intermediate-weight elements (i.e., Si or S) have been relatively well-studied. This chapter, therefore, concentrates on the studies of their spectra in the energy band above 5 keV including Fe-K emission. As proved in the previous chapters, Suzaku is superior to the other X-ray missions in the sensitivity for the Fe-K band. Utilizing this merit, we perform the Fe-K spectroscopy with the highest quality which had ever been obtained.

8.1 Tycho

8.1.1 Previous Results

The Tycho's SNR (G120.1+1.4, 3C10) recorded by Tycho Brahe in 1572 is generally considered to be a historical Type Ia SNR (e.g., Baade 1945). The distance to Tycho was determined to be 2.3 kpc by Green (1984); we assume this value in this section. The average energy index in radio band is measured to be $\alpha = 0.5$ (Katz-Stone et al. 2000). From the the width of the broad Hα emission, Ghavamian et al. (2001) derived the blast wave velocity of the east rim to be ~ 2000 km s^{-1}. However, the X-ray proper motion study by Hughes (1996; 2000) using ROSAT showed the average blast wave velocity is much higher, 4600 ± 400 km s^{-1}. FCRAO and Nobeyama CO data showed that a large molecular cloud surrounds the SNR along the northeastern boundary (Lee et al. 2004). Therefore, we can consider that the blast wave in this region is decelerated by this molecular cloud.

Hwang & Gotthelf (1997) found many emission-line features of Mg, Si, S, Ar, Ca, and Fe, using data obtained by ASCA. All narrow band images of these emission lines showed the shell-like morphology, but they are clearly distinct from each other. Especially, the radial profile of the Fe-K

line peaks at a smaller radius than the those of the other emission lines and continuum emission. This fact suggests an incomplete mixing of the Si and Fe layers. The average ionization age of the Si and S ejecta is reported to be (0.8–1.3) $\times$ 10^{11} cm^{-3} s (Hwang & Gotthelf 1997), whereas that of Fe ejecta is suggested to be much lower ($\sim 10^9$ cm^{-3} s: Hwang et al. 1998). The high-resolution XMM-Newton images confirmed that the Fe-K emission clearly peaks at a smaller radius (Decourchelle et al. 2001). Furthermore, the XMM-Newton image showed the contact discontinuity between the ejecta and ISM is partly distorted by the Rayleigh-Taylor instability.

The cosmic ray acceleration has also been studied for a long time. Hard X-rays were detected at energies up to 20 keV with Ginga (Fink et al. 1994); and 30 eV with RXTE (Petre et al. 1999). Using Chandra data, Hwang et al. (2002) showed the spectra at the SNR rim can be described by a non-thermal model, but could not reject the possibility of the thermal origin. Bamba et al. (2005) discovered very thin filaments on the outer edge of the SNR, and concluded they have the non-thermal origin.

8.1.2 Suzaku Observation

The Suzaku observation of the Tycho's SNR was made on 2006 June 27. The observation ID and exposure time were 500024010 and $\sim$ 102 ks, respectively. In addition, the background observation was made on 2006 June 29 (observation ID = 500025010) with the targeted position at (RA, Dec) = (00:36:54, 64:17:42), the nearby sky of Tycho. The exposure time was $\sim$ 51 ks. The Galactic latitudes of the source and background regions are almost consistent with each other.

The XIS were operated in the normal full-frame clocking mode, during both of the observations. We employed the cleaned revision 1.2 data, and used the HEADAS software version 6.0.4 and XSPEC version 11.3.2 for the data reduction and analysis. The response matrix files (RMF) and ancillary response files (ARF) were made using `xisrmfgen` and `xissimarfgen` (Ishisaki et al. 2007) version 2006-10-17.

8.1.3 Analysis and Results

Figure 8.1 shows the XIS 5.0–8.0 keV image of the Tycho's SNR (left), and the background region (right). First, we extracted the spectrum of the entire SNR from a 4.′3-radius circular region shown with a large green circle in figure 8.1 (left). For the background, we used the spectrum taken from the elliptical region shown in figure 8.1 (right). Since the data of the three FIs are nearly identical, we merged the individual spectrum to improve the photon statistics. The background-subtracted full-band spectra are shown in figure 8.2.

Although Kα and Kβ lines of intermediate-mass elements (Mg, Si, S, Ar, and Ca) are clearly divided, we concentrate on the spectral analysis in the energy band above 5 keV where Fe-K lines are included. In this energy band, Cr-Kα and Fe-Kβ as well as Fe-Kα are detected. Therefore, we study the features of these lines by fitting the 5–12 keV spectra with a power-law (for the

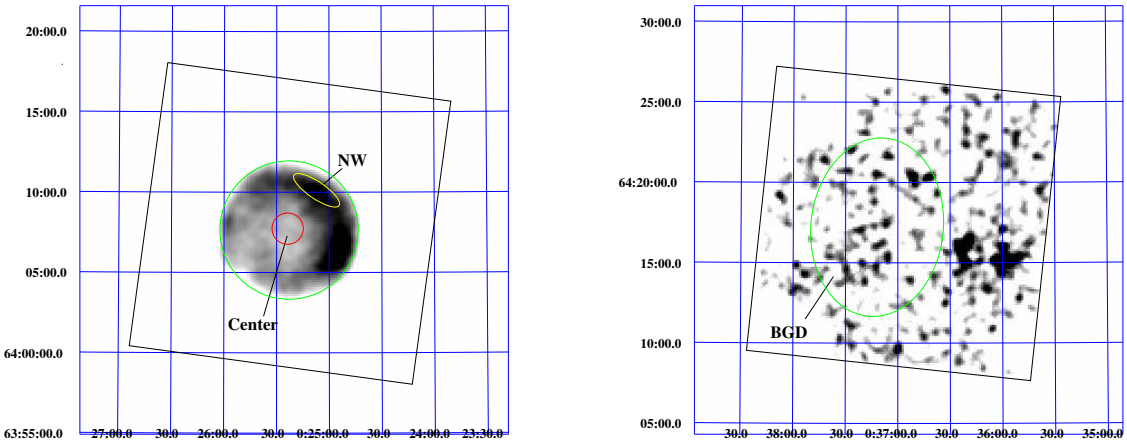

Fig. 8.1.—: Left: XIS 5.0–8.0 keV image of the Tycho's SNR. The large circle (green), the small circle (red), and the ellipse (yellow) show the regions where we extracted the spectra. The coordinates (RA and Dec) refer to epoch J2000.0. The Field of view of the XIS is indicated by the black square, where the data from the four XIS are combined, but that of the four corners, irradiated by the ^{55}Fe calibration sources, are removed. Right: XIS 5.0–8.0 keV image of the background sky. The green ellipse show the region for the background spectrum.

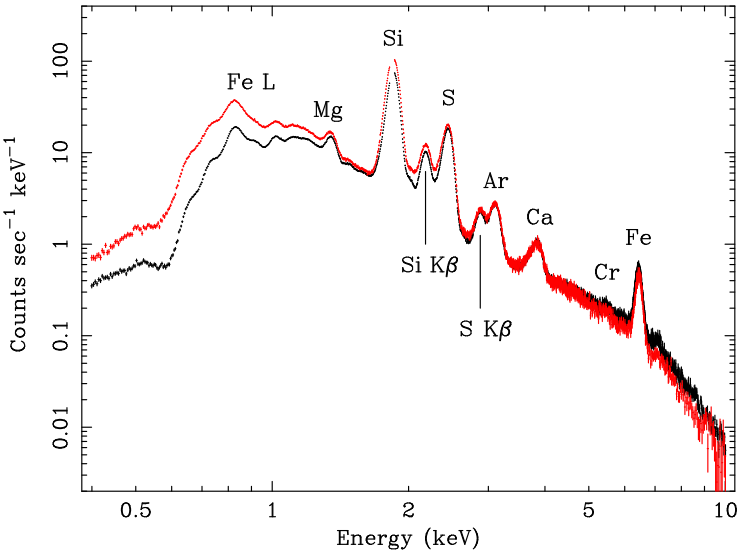

Fig. 8.2.—: Background-subtracted XIS spectra extracted from the whole region of the Tycho's SNR. Black and red represent the FI and BI, respectively.

Table 8.1:: Center energies and widths of the emission lines in the 5–12 keV spectrum of the Tycho's SNR.

Line	Center energy (eV)	Width* (eV)
Cr-Kα	5480 (5464–5496)	0
Fe-Kα	6444 (6443–6446)	61 (59–62)
Fe-Kβ	7104 (7087–7118)	0

*One standard deviation (1σ).

continuum) and Gaussians (for the lines). The best-fit central energies and widths are given in table 8.1. Although the central energy of the Fe-Kα is marginally higher than those of the SN 1006 and E0509–67.5 spectra (chapter 5 and 6), it is still much lower than that of He-like Fe-Kα (see table 3.1). Since an atomic physics for ionized Cr has not yet been well-studied at present, the ionization state of the Cr cannot be determined from the central energy. However, the ionization state must be extremely low, because the central energy of the Cr-Kα in the Tycho spectrum is found to be significantly lower than that of a Cr-Kα in a spectrum of N103B (see section 8.2), of which the ionization age is much higher than that of Tycho.

Ionization Age of the Fe Plasma

In order to estimate the ionization age of the plasma which produces Fe-K emission, we fitted the 5–12 keV spectra using a VNEI model. As seen in the previous sections, continuum fluxes above 5 keV of young SNRs are often explained by a non-thermal emission. Also in the case of Tycho, there is a high possibility that the origins of the hard continuum and the line emissions are different from each other. Indeed, bright non-thermal filaments had been discovered from the forward shock region of Tycho (Hwang et al. 2002; Bamba et al. 2005). Therefore, we tried to fit the continuum with a power-law, and the Fe-K line with a pure Fe plasma (a VNEI model). Since we showed in previous chapters Fe-K lines are typically reproduced by a 2–4 keV NEI plasma, we now fixed the electron temperature of the VNEI component to 3 keV, as the assumption. Since the NEI spectral code does not include the K-shell lines from Cr and Kβ of Fe in lower ionization states than He-like, we added Gaussians at 5.48 keV and 7.10 keV (see table 8.1).

Then, the best-fit χ^2/d.o.f. was obtained to be 2081/1124. The fitted spectra are shown in figure 8.3a. We can see the significant disagreement between the data and model around the Fe-Kα line. Anticipating the result shown below, we found that this disagreement can be explained by the superposition of red- and blue-shifted lines due to proper motions of the Fe ejecta. Hence, we fitted Fe-Kα line with 2-component VNEI models, which have the same values of red and blue shifts as well as the same values of the other parameters (i.e., kT_e, $n_e t$, and emission measure). Then, the fit was significantly improved with χ^2/d.o.f. of 1275/1123. The best-fit parameters are given in table 8.2. Note that, in this table, the emission measure is given as $n_e n_{\rm Fe} V$ for the sum of the red- and blue-shifted components, where V is the emitting volume. The fitted spectra are shown

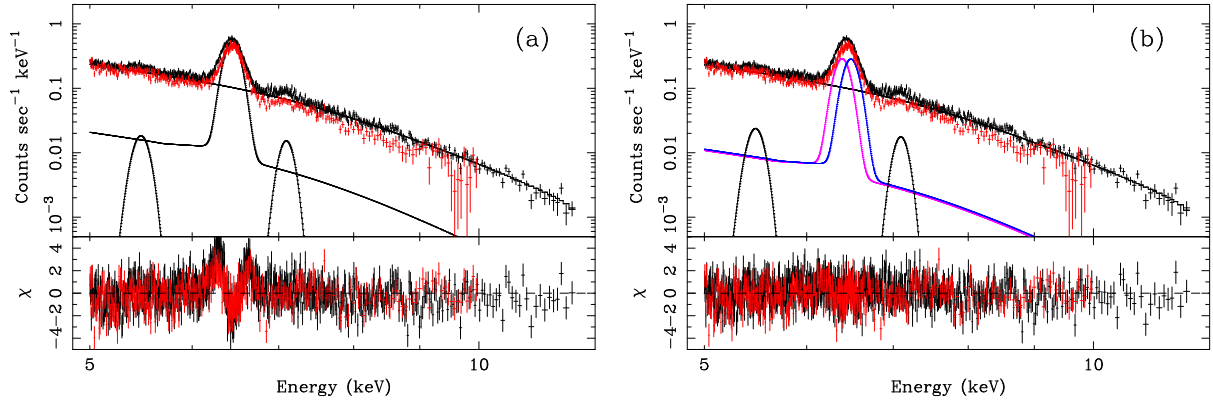

Fig. 8.3.—: (a) XIS 5–12 keV spectra of the whole region of the Tycho's SNR, fitted with the one-component VNEI, power-law, and Gaussians (see text). Black and red represent the FI and BI, respectively. (b) Same to (a), but fitted using the two-component VNEI. The red- and blue-shifted VNEI components are shown by magenta and blue solid lines, respectively.

Table 8.2:: Best-fit parameters of the fitting for the 5–12 keV spectrum of the Tycho's SNR.

Component	Parameter	Value
Power-law	Γ	2.70 (2.67–2.74)
	Norm* (photons cm^{-2} s^{-1})	7.5 (7.1–7.9) $\times$ 10^{-2}
VNEI (Fe)	kT_e (keV)	3.0 (fixed)
	$n_e t$ (cm^{-3} s)	8.0 (7.8–8.2) $\times$ 10^{9}
	$z^{\dagger}$	7.9 (7.8–8.3) $\times$ 10^{-3}
	$n_e n_{\rm Fe} V^{\ddagger}$ (cm^{-3})	1.20 (1.19–1.21) $\times$ 10^{55}
Cr-Kα	Center Energy (keV)	5.48 (fixed)
	Norm§ (photons cm^{-2} s^{-1})	1.8 (1.6–2.2) $\times$ 10^{-5}
Fe-Kβ	Center Energy (keV)	7.10 (fixed)
	Norm§ (photons cm^{-2} s^{-1})	2.2 (2.0–2.6) $\times$ 10^{-5}
χ^2/d.o.f.		1275/1123 = 1.14

*The differential flux at 1 keV.

†Red and blue shifts.

‡Sum of two components of the VNEIs (see text).

§Total flux in the Gaussians.

in figure 8.3b, in which the best-fit model is shown as solid lines colored magenta (the red-shifted VNEI), blue (the blue-shifted VNEI), and black (the other components).

The ionization parameter of the Fe-K emitting plasma is obtained to be $n_e t \sim 8 \times 10^9$ cm^{-3} s. In order to investigate how $n_e t$ depends on kT_e, we fixed kT_e to several values (other than 3 keV) and fitted the spectra. However, we found that the value of $n_e t$ does not change so much, when kT_e is higher than 2 keV.

If we fit the continuum with a bremsstrahlung model instead of the power-law, the good fit was also obtained with the electron temperature and emission measure of the bremsstrahlung component of $kT_e = 5.1$ keV and $n_e n_{\rm H} V = 2.2 \times 10^{58}$ cm^{-3}, respectively. The values of the other parameters (in the VNEI or Gaussian components) did not change from those listed in table 8.2.

Evidence of Doppler Shift

We extracted spectra from two regions: the Center and Northwest (NW) represented in figure 8.1 (left). For the background, we used the spectra taken from the elliptical region shown in figure 8.1 (right) again. The background-subtracted 5–12 keV spectra of the Center and NW are shown in figures 8.4a and 8.4b, respectively. We can see that the width of the Fe-Kα line is larger in the Center spectrum (a) than in the NW spectrum (b). In order to confirm it quantitatively, we fit these spectra with the same model what we used for the whole SNR spectrum. Then, the best-fit models are obtained as shown by the solid lines in figure 8.4. The obtained red and blue shift (z) for the Center spectra was 1.1 (1.0–1.2) $\times$ 10^{-2}. This value corresponds to the expansion velocity of $\sim$ 3300 km s^{-1}. On the other hand, z for the NW spectra was obtained to be 6.8 (5.3–7.5) $\times$ 10^{-3}, which is significantly lower than the value for the Center. Therefore, we can conclude that the shock-heated Fe ejecta is now expanding with the velocity of $\sim$ 3300 km s^{-1}, and the line

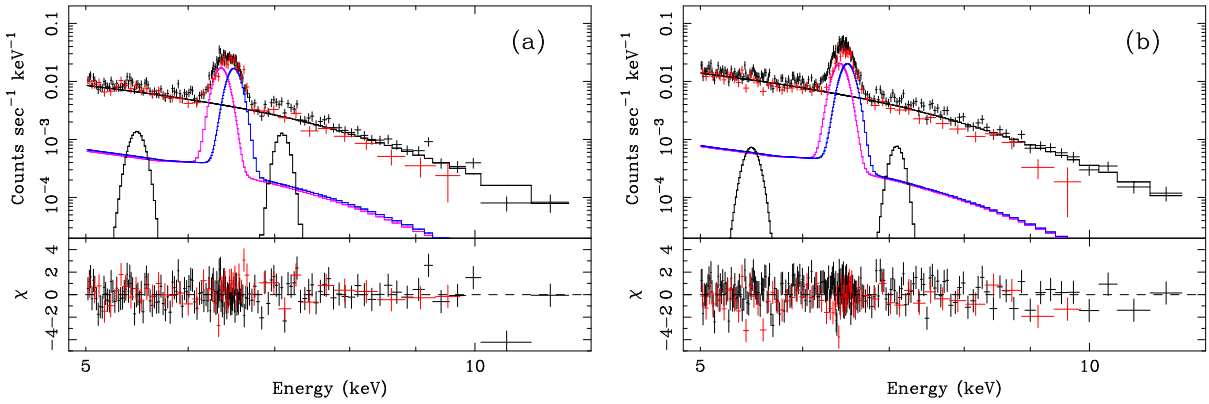

Fig. 8.4.—: XIS 5–12 keV spectra of the Center (a) and NW (b) of the Tycho's SNR. Black and red represent the FI and BI, respectively. Magenta and blue solid lines show the red- and blue-shifted VNEI components.

broadening is due to the superposition of the Doppler shifts.

8.2 N103B

8.2.1 Previous Results

N103B is the fourth brightest X-ray SNR in the LMC. It was first identified as a SNR by Mathewson et al. (1983) based on the non-thermal nature of its radio spectrum and the relative strengths of Si II and Hα emission lines. From its small size (3 pc-radius), Hughes et al. (1995) estimated the age to be $\sim$ 1500 yrs. Chandra data showed that the remnant is much brighter on the western rim than toward the East (Lewis et al. 2003), this is possibly due to density contrasts between the East and West.

The remnant is located on the northeastern edge of an H II region DEM 84, $\sim$ 40 pc from the young star cluster NGC 1850. Furthermore, the optical spectrum is not dominated by the strong Balmer lines which are often associated with the remnants of Type Ia SN (Tuohy et al. 1982). For long years, therefore, it was considered that N103B had a massive star progenitor (e.g., Chu & Kennicutt 1988). However, Hughes et al. (1995) found strong emission lines from Si, S, Ar, Ca, and Fe, while no emission from O, Ne, or Mg in ASCA spectrum. They hence concluded that N103B is the result of a Type Ia SN. On the other hand, the high energy resolution spectra of the Reflection Grating Camera (RGS) on board XMM-Newton showed prominent O, Ne, and Mg emission (van der Heyden et al. 2002). They hence claimed that N103B was the result of a core-collapse SN. However, Lewis et al. (2003) analyzed Chandra data and considered that the O emission was associated with the ISM rather than the ejecta. Thus, the classification of N103B is still somewhat uncertain.

8.2.2 Suzaku Observation

The Suzaku observation of the SNR N103B was made on 2005 August 30 with the targeted position at (RA, Dec) = (05:08:58, –68:43:10). The observation ID and exposure time are 100013010 and $\sim$ 33 ks, respectively. The XIS were operated in the normal full-frame clocking mode. We employed the cleaned revision 1.2 data, and used the HEADAS software version 6.0.4 and XSPEC version 11.3.2 for the data reduction and analysis. The response matrix files (RMF) and ancillary response files (ARF) were made using `xisrmfgen` and `xissimarfgen` (Ishisaki et al. 2007) version 2006-10-17.

8.2.3 Analysis and Results

Since the diameter of the SNR ($\sim 30''$) is much smaller than the angular resolution of the XRT, ($\sim 2'$: Serlemitsos et al. 2007), N103B can be regarded as a point-like source. Therefore, we

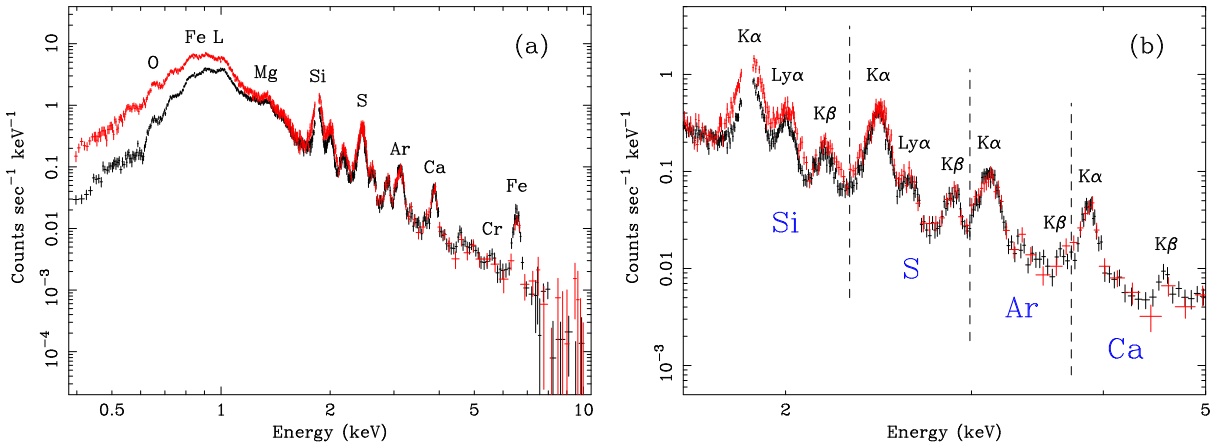

Fig. 8.5.—: (a) Background-subtracted XIS spectra of N103B. Black and red represent the FI and BI, respectively. (b) Same to (a), but in 1.5–5.0 keV.

Table 8.3:: Center energies and widths of the emission lines in the 5–10 keV spectrum of N103B.

Line	Center energy (eV)	Width* (eV)
Cr-Kα	5600 (5520–5665)	0
Fe-Kα	6550 (6539–6561)	95 (81–105)

*One standard deviation (1σ).

extracted XIS spectra from a circular region of $3'$ radius centered on the SNR. The background spectra were extracted from the annular region around the source with inner and outer radii of $3'$ and $6'$, respectively. Since the data of the three FIs are nearly identical, we merged the individual spectrum to improve the photon statistics. The background-subtracted full-band spectra are shown in figure 8.5a. Figure 8.5b shows the same spectra but in the 1.5–5.0 keV band, where Lyα lines of H-like Si and S as well as K-shell lines of the He-like ions are clearly seen. This implies the ionization age of the plasma in N103B is older than those in SN 1006, E0509–67.5, and Tycho, because the spectra of these SNRs show no feature of the H-like lines of the intermediate-mass elements (see figure 8.2, for example).

Similarly to section 8.1, we concentrate on the spectral analysis in the energy band above 5 keV. The XIS 5–10 keV spectra are shown in figure 8.6. In addition to Fe-Kα, we detected the Cr-Kα line, for the first time. We fitted the 5–10 keV spectra with a power-law (for the continuum) and Gaussians (for the emission lines), and then determined the center energies and the widths of the lines as given in table 8.3. We found the Kα of both of Cr and Fe have higher central energies than those of the Tycho spectrum (for comparison, see table 8.1).

Ionization Age of the Fe Plasma

We fitted the 5–10 keV spectra using a VNEI model to determine the ionization age of the Fe-K emitting plasma. Similarly to the previous section, we included a power-law to reproduce the continuum flux, and fitted the Fe-K line with a VNEI model which consists purely of Fe ions and electrons. The electron temperature of the VNEI was assumed to be 3 keV. Since the NEI code does not include Cr-Kα lines, we added Gaussians at 5.60 keV.

Then, the best-fit χ^2/d.o.f. was obtained to be 57/45. Although the fit was acceptable from a statistical point of view, we found that the model could not reproduce the Fe-Kα profile, as shown in figure 8.6a. On the analogy of the result obtained in section 8.1, we considered this line broadening is due to the superposition of Doppler shifts. We, therefore, fitted the Fe-Kα line with 2-component VNEI models, which have the same values of red and blue shifts as well as the same values of the other parameters. Then, the fit was significantly improved with χ^2/d.o.f. = 22/44. The best-fit parameters are given in table 8.4. Note that emission measure is given as $n_e n_{\rm Fe} V$ for the sum of the red- and blue-shifted components, where V is emitting volume. The fitted spectra are shown in figure 8.6b, in which the best-fit model is shown as solid lines colored magenta (the red-shifted VNEI), blue (the blue-shifted VNEI), and black (the other components). The red (or blue) shift was obtained to be $z \sim 0.01$, which corresponds to the proper motion velocity of ~ 3000 km s^{-1}. Note that, however, the spectrum is what integrated with the emission from the whole SNR. Therefore, the actual expansion velocity (of the shock-heated Fe-rich ejecta) is possibly higher than 3000 km s^{-1}.

We fitted the spectra fixing kT_e to several values other than 3 keV, and investigated the dependence of $n_e t$ to kT_e. However, we found that the value of $n_e t$ does not change so much, when

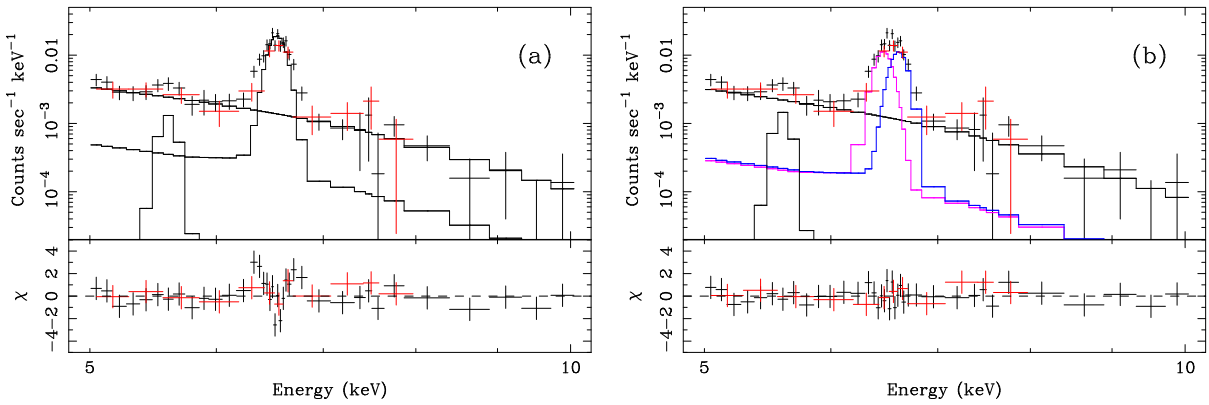

Fig. 8.6.—: (a) XIS 5–10 keV spectra of N103B, fitted with the one-component VNEI, power-law, and Gaussian. Black and red represent the FI and BI, respectively. (b) Same to (a), but fitted using the two-component VNEI. The red- and blue-shifted VNEI components are shown by magenta and blue solid lines, respectively.

Table 8.4:: Best-fit parameters of the fitting for the 5–10 keV spectrum of N103B.

Component	Parameter	Value
Power-law	Γ	3.1 (2.4–4.0)
	Norm* (photons cm^{-2} s^{-1})	1.7 (0.55–9.1) $\times 10^{-3}$
VNEI (Fe)	kT_e (keV)	3.0 (fixed)
	$n_e t$ (cm^{-3} s)	3.5 (3.2–4.0) $\times 10^{10}$
	$z^{\dagger}$	1.1 (0.93–1.2) $\times 10^{-2}$
	$n_e n_{\rm Fe} V^{\ddagger}$ (cm^{-3})	1.5 (1.3–1.7) $\times 10^{54}$
Cr-Kα	Center Energy (keV)	5.60 (fixed)
	Norm§ (photons cm^{-2} s^{-1})	9.3 (2.0–16) $\times 10^{-7}$
χ^2/d.o.f.		22/44 = 0.50

*The differential flux at 1 keV.
†Red and blue shifts.
‡Sum of two components of the VNEIs (see text).
§Total flux in the Gaussian.

kT_e is higher than 2 keV.

If we fit the continuum with a bremsstrahlung model instead of the power-law, the good fit was also obtained with the electron temperature and emission measure of the bremsstrahlung component of $kT_e = 3.5$ keV and $n_e n_{\rm H} V = 4.3 \times 10^{58}$ cm^{-3}, respectively. The values of the other parameters (in the VNEI or Gaussian components) did not change from those listed in table 8.4.

8.3 Summary of the Chapter

We have analyzed Suzaku/XIS data obtained from the Tycho's SNR and N103B. The new facts revealed in this chapter are summarized as follows:

1. The ionization ages of the Fe-K emitting plasmas in the Tycho's SNR and N103B were respectively determined to be $n_e t = 8.0$ (7.8–8.2) $\times 10^9$ and $n_e t = 3.5$ (3.2–4.0) $\times 10^{10}$, which are the tightest constraints obtained so far.

2. Cr-Kα lines were detected from both the SNRs, for the first time.

3. Evidences of Doppler shift due to the expansion of the Fe-rich ejecta were found from Fe-Kα lines of the spectra of both the SNRs.

Chapter 9

Discussion

9.1 Summary of the Results

In the previous chapters, we analyzed the X-ray data of several young SNRs (SN 1006, E0509–67.5, RCW 86, Tycho, and N103B) obtained with the newest X-ray astronomical satellite Suzaku. Thanks to the superior performances of Suzaku, especially the sensitivity and the spectral resolution in the Fe-K band, we successfully demonstrated a lot of new results. From SN 1006, we firmly detected the K-shell emission from Fe, for the first time, and found that the Fe ionization state is quite low. We accurately determined the ionization age of Fe ejecta in E0509–67.5, and showed it was significantly lower than what was previously reported. The Fe-K line morphology in the RCW 86 northeastern region was revealed for the first time, and the origin of the Fe-K emission was determined to be the Fe-rich ejecta. From the Fe-K spectra of Tycho and N103B, we found the evidences of Doppler shift due to the ejecta expansion. Furthermore, we detected the Cr-K lines from these SNRs, for the first time.

In particularly the analyses of SN 1006 and E0509–67.5, we performed the full-band fittings by logically dividing the spectra into several components: the ejecta (heated by reverse shock), the ISM (heated by the blast wave), and the non-thermal component. As the results, we found that the ionization ages ($n_e t$) of Fe-rich ejecta (in both the SNRs) are significantly different from those of the ejecta abundant with the other elements (i.e., Si, S). Here, we summarize in table 9.1 the physical properties of all the SNRs which we observed. In this table, $n_e t$[Si] and $n_e t$[Fe] respectively means the ionization ages of Fe-rich and Si-rich ejecta, and n_0 indicates the average ambient density. The values which are not obtained in this thesis referred to other papers (see footnote in table 9.1). We will use these values to develop further discussions in sections 9.3 and 9.4.

Table 9.1:: Summary of the results.

	n_et[Si] (cm^{-3} s)	n_et[Fe] (cm^{-3} s)	n_0^* (cm^{-3})	Age (yr)	Radius (pc)
SN 1006	1.4 (1.2–1.6) $\times 10^{10}$	7.7 (6.7–9.2) $\times 10^8$	0.03	1000	9.5
E0509–67.5	1.4 (1.3–1.5) $\times 10^{10}$	3.5 (3.1–3.6) $\times 10^9$	$\lesssim 0.05^\dagger$	$\lesssim 850^\dagger$	3.7
Tycho	1.0 (0.8–1.3) $\times 10^{11}$ ‡	8.0 (7.8–8.2) $\times 10^9$	$1.0^\S$	430	2.8
N103B	$> 10^{12}$ $^\parallel$	3.5 (3.2–4.0) $\times 10^{10}$	?	$\sim 1500^\#$	3.7
RCW 86	?	2.3 (1.8–2.9) $\times 10^9$	Various**	1820	18

*Ambient density. †Warren & Hughes (2004); ‡Hwang & Gotthelf (1997);
§Badenes et al. (2006); $^\parallel$Lewis et al. (2003); $^\#$Hughes et al. (1995);
**Spatial variation of the ambient density is quite large.

9.2 Nucleosynthesis in Type Ia SNe

SN 1006, E0509–67.5, and Tycho are surely classified as the remnants of Type Ia SN (e.g., Schaefer 1996; Hughes et al. 1995; Baade 1945). Indeed, we showed (in sections 5.6 and 6.5) that the relative abundances in the ejecta components of SN 1006 and E0509–67.5 are almost consistent with the predicted nucleosynthesis yield of the carbon deflagration model (W7: Nomoto et al. 1984), except for the high-Z elements such as Fe (see figures 5.12a and 6.7a). The reason of the lack of the Fe abundances will be discussed again in section 9.3. The W7 model is widely used as the standard model for the nucleosynthesis in Type Ia SNe. Strictly speaking, however, we can see that the abundance ratios of Si/O and S/O which we obtained are slightly higher than the predicted values. These results suggest that the amount of O ejected by Type Ia SN explosion is smaller than the predicted value by the deflagration model.

A more efficient burning (relative to the deflagration model) of C and O at the surface of a white dwarf is predicted by the delayed detonation model (e.g., Iwamoto et al. 1999). The delayed detonation in Type Ia SNe was first proposed by Khokhlov et al. (1991). This theoretical model assumes a slow initial deflagration at the center of a white dwarf and a deflagration-to-detonation transition (DDT) at some stage of the thermonuclear explosion. Due to the supersonic detonation wave, larger amounts of intermediate-weight elements (i.e., Si, S, and Ca) and Fe-group elements are expected to be synthesized, and only a few light elements (i.e., C, O, and Ne) are left without burning (see table 2.2 and figure 2.4). In the case of Tycho, Badenes et al. (2006) found that the X-ray spectra obtained with XMM-Newton and Chandra are well reproduced by an optimized delayed detonation model. Therefore, the relative abundances of the elements synthesized by Type Ia SN explosions may be generally similar to what predicted by the delayed detonation model rather than the pure deflagration model.

However, we should note that the delayed detonation models constructed by Iwamoto et al. (1999) and Badenes et al. (2006) are only one-dimensional models. They did not include any

asymmetrical effects, Rayleigh-Taylor and Kelvin-Helmholtz instabilities, and turbulence, which should be essentially taken into consideration. Some simulations have explored delayed detonation explosions in three dimensions (e.g., Gamezo et al. 2005). However, since the mechanism of the DDT had not been understood, they artificially determined the central densities (of a white dwarf) when the DDT occurs. Under the present condition, the delayed detonation is only one of the phenomenological model to explain the abundances of the produced elements obtained by observations of Type Ia SNe and their remnants.

9.3 Ejecta Distribution

Figure 9.1 shows the plot of the $n_e t$[Si] and $n_e t$[Fe] of each SNR listed in table 9.1. RCW 86 is not included because it shows no evidence of Si line emission which originates from the ejecta. We can clearly see that $n_e t$[Fe] are significantly lower than $n_e t$[Si] in the cases of all SNRs. Although the dispersion is large, $n_e t$[Fe] are approximately consistent with 10% of $n_e t$[Si]. A possible scenario to explain this fact is: when the Si ejecta began to be heated by a reverse shock, most of the Fe ejecta had not arrived at the shock front yet. After the volume of the SNRs became about 10 times larger, the Fe ejecta gradually began to be heated. As a matter of fact, since n_e is not uniform in each SNR and depends on the ionization state of the elements, it is difficult to quantitatively determine when the Si and Fe were heated. However, it is at least suggested that the Fe-rich ejecta layers were distributed inward of the Si-rich layers.

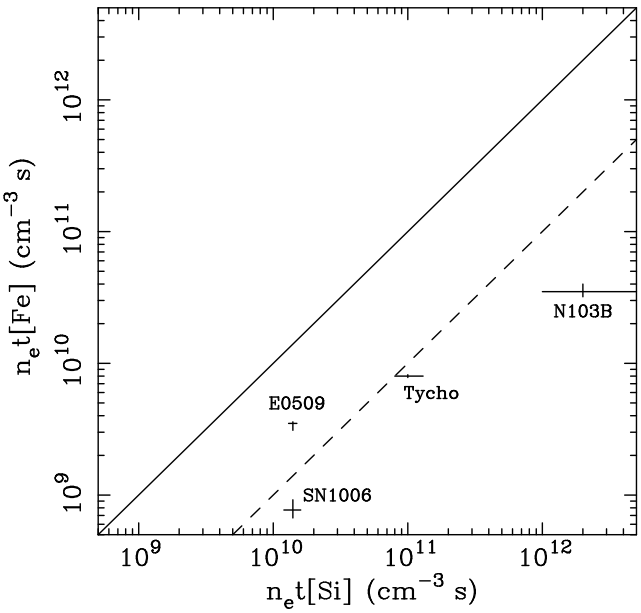

Fig. 9.1.—: Ionization parameters of Si ejecta ($n_e t$[Si]) and Fe ejecta ($n_e t$[Fe]) for each SNR. The solid and dashed lines represent $n_e t$[Si] = $n_e t$[Fe] and $n_e t$[Si] = 10 $n_e t$[Fe], respectively.

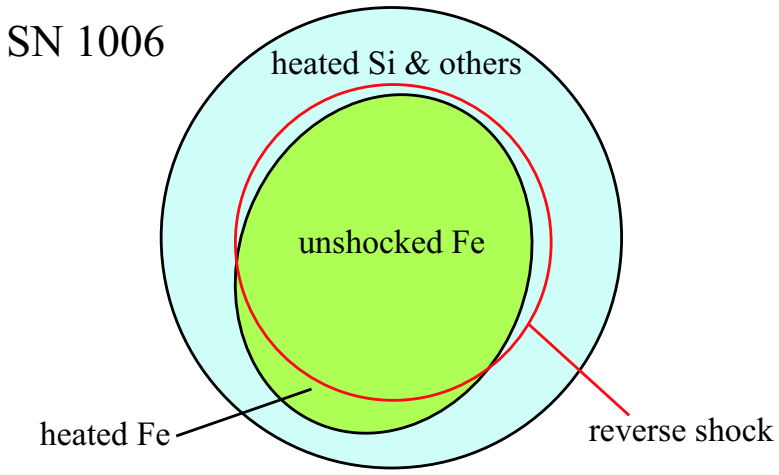

Fig. 9.2.—: Schematic view of ejecta and reverse shock structures in SN 1006.

For this interpretation, we can expect that the emission from Fe in these SNRs are spatially located interior to the emission from Si and the other elements. In the case of Tycho, it was reported that the Fe-K emission is more centrally distributed than the K-shell emission of other elements (Hwang et al. 1998; Decourchelle et al. 2001). On the other hand, in SN 1006, we could not find the interior distribution of Fe-K emission, but it was concentrated at the southern part of the SNR rim (see figure 5.6). This result suggests that most of the Fe ejecta in SN 1006 has not yet been heated by the reverse shock except for the southern rim. We show in figure 9.2 a schematic view of the SNR structure derived from our interpretation. Similarly to SN 1006, in E0509–67.5 and Tycho, a large amount of Fe ejecta may remain distinct from other ejecta in the inner layer and thus be too cool to provide enough X-ray emission. This is the possible reason why the Fe abundances we obtained from these young Type Ia SNRs are much lower than the predicted value.

In the theory for a Type Ia SN explosion, the lower expansion velocity of ^{56}Ni relative to those of the other elements is expected, as shown in figure 9.3 taken from Iwamoto et al. (1999). (Note that this figure shows the deflagration case, but the delayed detonation models produce qualitatively similar distribution.) Although this theoretical expectation is derived from an one-dimensional simulation, nevertheless our observational results qualitatively support it. Therefore, the ejecta mixing effect inside the progenitor star due to the Rayleigh-Taylor instability is suggested to be almost negligible at least in the Type Ia SN explosion.

By contrast, in several core-collapse SNRs, for example, Cas A (Hughes et al. 2000a; Hwang et al. 2000; 2004), and G292.0+1.8 (Park et al. 2002; 2007), the abundance structure is quite complex; significant mixing effects are suggested. Figure 9.4 shows an X-ray image of Cas A obtained by Chandra million-second observation (Hwang et al. 2004). Red, Blue, and Green colors represent Si-K band (1.78–2.0 keV), Fe-K band (6.52–6.95 keV), and continuum emission (4.2–6.4 keV), respectively. In the southeastern side of the remnant, we can see that the Fe ejecta lies exterior

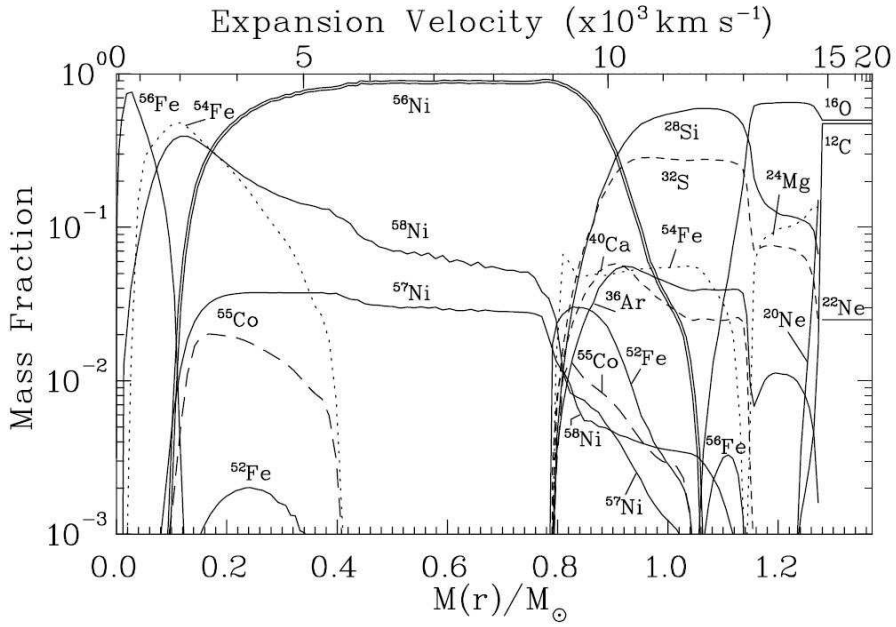

Fig. 9.3.—: Composition structure of Type Ia SNe after the freezing of nuclear reactions for the case of the W7 model. The horizontal axis is the distance from the stellar center indicated by the mass coordinate; the corresponding expansion velocity is shown at the top of the panel. This figure is taken from Iwamoto et al. (1999).

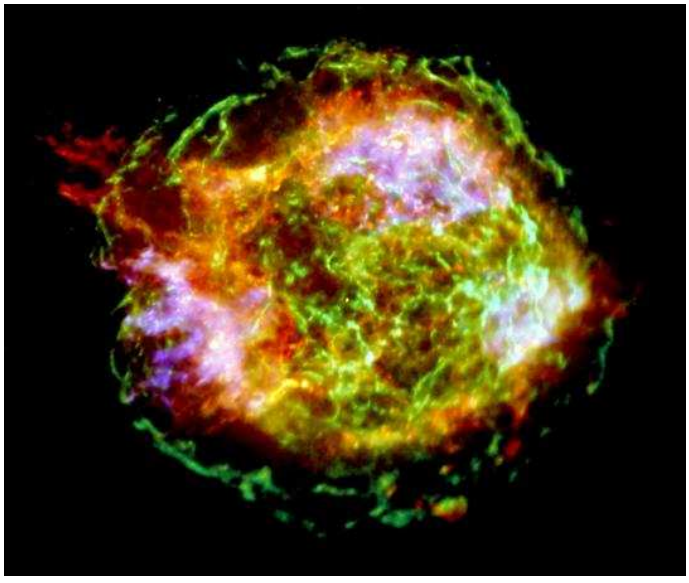

Fig. 9.4.—: Chandra million-second image of Cas A. Red, Blue, and Green contain emission from 1.78–2.0 keV (Si-K band), 6.52–6.95 keV (Fe-K band), and 4.2–6.4 keV band (continuum), respectively. North is up and east is to the left. Credit: NASA/CXC/GSFC/Hwang et al. (2004).

to the lighter Si ejecta; this structure was first reported by Hughes et al. (2000a). Since ^{56}Ni is synthesized (by complete Si burning) at deeper region in the progenitor star than Si is synthesized (by O burning), this ejecta distribution requires that a spatial overturning of a significant portion of the SN core. As the source of such large-scale mixing, neutrino-driven convection for initiating core-collapse SN explosions is proposed (Herant et al. 1994; Burrows et al. 1995).

The contrast between the ejecta distribution of Type Ia SNRs and that of core-collapse SNRs may be useful to presume progenitors of the other SNRs. In chapter 7, we found that the Fe-K emission observed from RCW 86 northeastern region has the ejecta origin. If the lower-Z elements (e.g., O or Si) distribute exterior to the Fe ejecta, we must have observed emission from them. However, we did not find any evidence of such elements in the ejecta component. Therefore, we consider that the inversion of the ejecta occurred in RCW 86, similarly to Cas A and G292.0+1.8, and hence the lower-Z elements have not yet been heated enough. Indeed, since RCW 86 is spatially coincident with an OB association (Westerlund 1969), RCW 86 is likely to be the remnant of a core-collapsed SN.

N103B (section 8.2) is also located in a star forming region. Therefore, the progenitor of this SNR is still debatable. However, Lewis et al. (2003) found that the Fe-K emission is located centrally, as seen in Tycho (Hwang & Gotthelf 1997), while the Si-K emission is more prominent in exterior regions of the remnant. Qualitatively, such ejecta distribution is more similar to that seen in Tycho than that seen in Cas A and G292.0+1.8. Furthermore, as we show in figure 9.1, the relation between the n_et[Si] and n_et[Fe] is also similar to those of the other Type Ia SNRs (i.e., SN 1006, E0509–67.5, and Tycho). For these reason, we strongly propose that N103B is a Type Ia remnant. However, van der Heyden et al. (2002) claimed that N103B has a Type II origin because the XMM-Newton spectra showed prominent O-K emission. In this thesis, we analyzed the Suzaku spectra of N103B only in the energy band above 5 keV, but Suzaku has good sensitivity and energy resolution also in the energies below 1 keV (Koyama et al. 2007). Utilizing these performances, we must investigate the amounts of O and other lower-Z elements to determine the origin of this SNR, in the future work.

9.4 ISM Density and Evolutional State of the SNRs

The ages of SN 1006 and Tycho are well-known from their historical records: 1000 yr and 430 yr, respectively. Although the real age of SN 1006 is more than two times older than that of Tycho, the ionization age (both of the n_et[Si] and n_et[Fe]) is significantly younger in the former than the latter, as shown in figure 9.1. This may be due to the extremely low density of ISM around SN 1006. According to the equations (1), (2), and (5) of Ferrière (2001), The space-averaged number densities of H_2 (hydrogen in molecular form), H I (neutral atomic hydrogen), and H II (ionized hydrogen) as the functions of Z-height (the distance from the Galactic plane) are given as figure 9.5. The distance to SN 1006 (from the solar system) is 2.2 kpc (Winkler et al. 2003), and the Galactic latitude of this SNR is $b = +14.6$. They correspond to $Z = 550$ pc, where the average ISM density is 0.03 cm^{-3}. This is fully consistent with the value which we determined in chapter 5

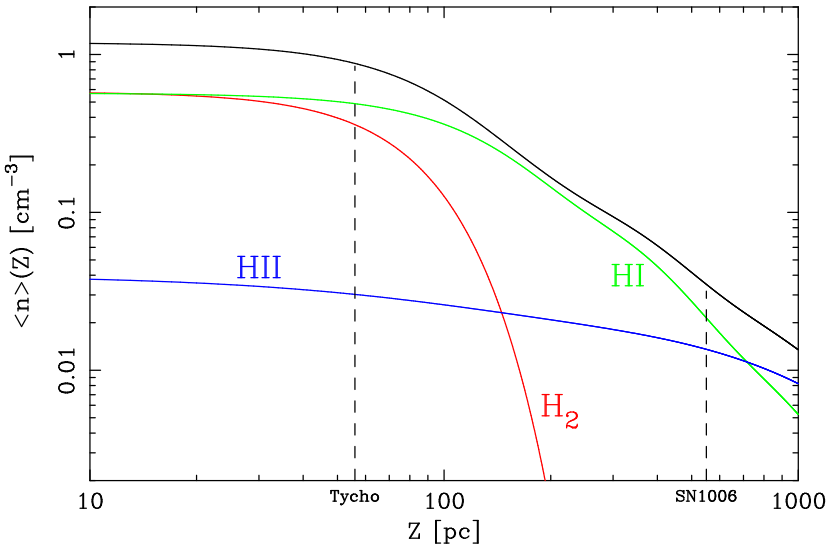

Fig. 9.5.—: Space-averaged number densities of hydrogen in the molecular form (H_2: red), neutral atomic hydrogen (H I: green), and warm ionized hydrogen (H II: blue) as the functions of the distance from the Galactic plane, according to the approximate equations given by Ferrière (2001). The black curve represents the sum of the three components. The Z-heights of SN 1006 and Tycho are also indicated.

(also listed in table 9.1). On the other hand, the distance to Tycho is 2.3 kpc (Green 1984), and its Galactic latitude is $b = +1.4$, corresponding to $Z = 56$ pc. Since it is very near to the Galactic plane, the ISM density of 1 cm^{-3} is much higher than that around SN 1006. Therefore, it seems that the ionization of the ejecta in Tycho was quickly developed in the very early phase of the remnant evolution.

As described in section 3.1, the lower an ambient density is, the slower a dynamical evolution of an SNR becomes. Using the equations given by Truelove & McKee (1999), we calculated the explosion energies (E), average radii of the reverse shock (R_r), and velocities of the blast wave and reverse shock (v_b and v_r, for the observer rest frame) of SN 1006 and Tycho. We simply assumed the uniform density profiles of the ejecta and ambient medium, and included the values of the age, ambient density (n_0), and blast wave radius (R_b), listed in table 9.1. The results are given in table 9.2. In the both cases of SN 1006 and Tycho, we found that the reverse shocks still propagate

Table 9.2:: Dynamical parameters of SN 1006 and the Tycho's SNR.

	E (10^{51} ergs)	R_b (pc)	R_r (pc)	v_b (km s^{-1})	v_r (km s^{-1})
SN 1006	1.4	9.5	6.6	5100	2700
Tycho	0.61	2.8	2.0	3600	2000

outward with high velocities, namely both the SNRs are in the early stage of the transition phase between the free expansion and Sedov phases. Even if we assumed the exponential ejecta density profiles (instead of uniform distributions) and calculated the dynamical parameters following the equations given by Dwarkadas & Chevalier (1998), the results did not change essentially. Note that, the blast wave velocity of SN 1006 northwest (NW) rim (~ 2890 km s^{-1}: Ghavamian et al. 2002) determined by the Hα observation is much lower than our estimation given in table 9.2. This is probably due to that the ISM density around NW rim is locally high. Indeed, Hα emission is the brightest at the NW rim (see figure 5.2), and the ambient density of this region is estimated to be 0.3–0.5 cm^{-3} (Dubner et al. 2002).

We again use the equations given by Truelove & McKee (1999), and expected the future dynamical evolutions of SN 1006 and Tycho. Figure 9.6 shows the expected average radii of the blast wave (solid lines) and the reverse shock (dashed lines) as the functions of ages of each SNR. In the case of SN 1006, since the ambient density is extremely low, the reverse shock will not arrive at the center of the remnant until ~ 3000 years after. Therefore, the transition phase (between the free expansion stage and the Sedov stage) will continue for a long time. On the other hand, in the case of Tycho, the reverse shock will begin to propagate inward ~ 400 years after. When the age will be ~ 1800 yr, the reverse shock will arrive at the SNR center, and hence all of the ejecta will be heated completely.

In chapter 7, we reported the results of the Suzaku observation on the RCW 86 northeast quadrant, and revealed for the first time the morphology of the shock-heated Fe-rich ejecta in this region. Then, we found that the radius of the reverse shock behind the East rim (where the ambient density is large) is smaller than that behind the NE rim (which expands in a tenuous region). It is very interesting that the evolution of the reverse shock is quite different from position to position even in one SNR, if the ambient density has a large spatial variation. The additional observation on

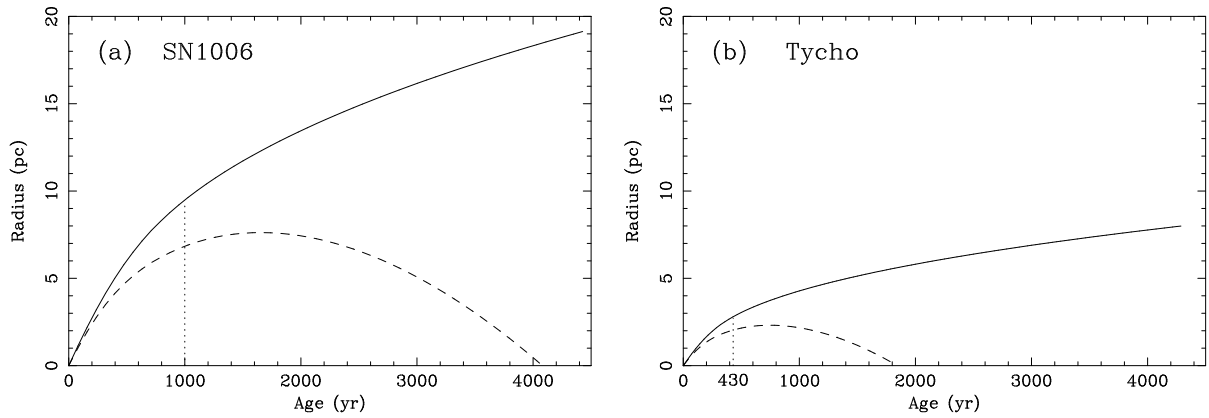

Fig. 9.6.—: (a) Expected shock evolution of the blast wave (solid line) and the reverse shock (dashed line) in SN 1006. Uniform density distributions of the ejecta and ambient medium are assumed. The dotted line indicates the present. (b) The same to (a), but for the Tycho's SNR.

the other region of RCW 86 will be helpful for the deeper understanding of the dynamical evolution of SNR shock in inhomogeneous interstellar space.

9.5 Future Works

Construction of the Plasma Code

Due to the excellent energy resolution of Suzaku, we newly detected many emission lines: Kα from low ionized Ar and Ca (in SN 1006 and E0509–67.5), Kβ from low ionized Si (in E0509–67.5) and Fe (in Tycho), Cr-Kα (in Tycho and N103B), and possibly O-K series in the higher transitions (in SN 1006). Since these lines have quite low emissivities and hence can be ignored in most cases, they have not been included in the plasma codes which we used in this thesis. However, in the case of young ejecta-dominated SNRs, contributions of these lines are never negligible as we showed. Furthermore, they are very important informations to determine more accurately the thermal condition of the plasma and the abundances of synthesized elements. It is necessary to understand the atomic physics in low ionization states, and to construct a more detailed plasma code.

Measurement of Ion Temperature

We found that in the young SNRs with low ambient densities, such as SN 1006 or E0509–67.5, both the swept-up ISM and the heated ejecta are far from the full ionization equilibrium. Therefore, it is expected that the equilibration between the ion and the electron temperatures have not been achieved as well. Indeed, the electron to proton temperature ratios of ISM just behind the forward shock are measured in several SNRs by optical observation (summarized by Rakowski 2005). For example, in the case of SN 1006, the ratio is constrained to be $T_e/T_{\rm H} \leq 0.07$ (Ghavamian et al. 2002). On the other hand, the ion temperature of ejecta can be measured from widths of the emission lines broadened by the thermal Doppler effect. However, we at present have no detector which has enough energy resolution to measure the line broadening. In young SNRs, since most of the energy must be stored in the ions *in the ejecta*, the measurement of the ion temperatures is necessary for the study of the energetics of SNRs in early evolutional state.

X-ray micro-calorimeter on board NeXT satellite, which will be launched on 2012, has a very high energy resolution of ~ 5 eV (FWHM) in the whole energy band of 0.3–12 keV. On the other hand, the line width due to a thermal Doppler broadening is described as

$$\Delta E = 2(\ln\ 2)^{1/2} E \left(\frac{2kT_i}{m_i c^2}\right)^{1/2}\ [\mathrm{eV}]\ , \tag{9.1}$$

where E, T_i, and m_i are energy of the emission line, temperature and mass of the ion, respectively. c is the light speed. Therefore, if the temperatures of Si ($kT_{\rm Si}$) or Fe ($kT_{\rm Fe}$) are respectively higher than 35 keV or 6 keV, their line widths are obtained to be $\Delta E > 5$ eV, and hence they can be

detected ideally. For example, when the reverse shock velocity is 2000 km s^{-1} (for the reverse shock rest frame), the post-shock ion temperatures are expected to be $kT_{\rm Si} \sim 220$ keV and $kT_{\rm Fe} \sim 440$ keV, according to equation 3.36 and assuming the complete collisionless shock. Therefore, we will be able to measure the ion temperatures of ejecta in typical young SNRs using the micro-calorimeter. Such observations are strongly encouraged.

Chapter 10

Conclusion

We performed an X-ray study of ejecta-dominated SNRs, SN 1006, E0509–67.5, RCW 86, Tycho, and N103B, utilizing the good energy resolution and high sensitivity of Suzaku. The important results are summarized as follows:

1. Including the low-ionized Fe K-shell emission from SN 1006, many emission lines are firmly detected for the first time, and their central energies are determined with high accuracy. Since some of these lines are not included in the plasma code which we used, a detailed study of the atomic physics and a construction of the plasma code are much required.

2. The full-band spectra extracted from SN 1006 and E0509–67.5 are well-described by models with several plasma components. The relative abundances of the heavy elements in the ejecta components are almost consistent with predicted nucleosynthesis yield of the Type Ia SN.

3. The ionization ages of the Fe ejecta in the Type Ia SNRs are significantly lower than those of the lighter element ejecta. This fact suggests that Fe have been heated by reverse shock more recently than the other elements. This explanation is consistent with a picture where the ejecta are stratified by composition with Fe in the interior.

4. The extreme non-equilibrium states of the plasma in SN 1006 and E0509–67.5 are due to the low densities of the ambient medium.

5. The ambient density of RCW 86 has a large spatial variation. Therefore, the evolution of the reverse shock in this SNR is quite different from position to position; the radius of the reverse shock behind the dense region is smaller than that behind the tenuous region.

References

Acero, F., Ballet, J., & Decourchelle, A. 2007, A&A, 475, 883

Aharonian, F., et al. 2007a, A&A, 464, 235

Aharonian, F., et al. 2007b, ApJ, 661, 236

Allen, G. E., Petre, R., & Gotthelf, E. V. 2001, ApJ, 558, 739

Anders, E., & Grevesse, N. 1989, Geochim. Cosmochim. Acta, 53, 197

Arnett, W. D. 1969, Ap&SS, 5, 180

Arnett, W. D. 1996, Supernova and Nucleosynthesis, (Princeton: Princeton University Press)

Baade, W. 1945, ApJ, 102, 309

Badenes, C., Borkowski, K. J., Hughes, J. P., Hwang, U., & Bravo, E. 2006, ApJ, 645, 1373

Bamba, A., Koyama, K., & Tomida, H. 2000, PASJ, 52, 11

Bamba, A., Yamazaki, R., Ueno, M., & Koyama, K. 2003, ApJ, 589, 827

Bamba, A., Yamazaki, R., Yoshida, T., Terasawa, T., & Koyama, K. 2005, ApJ, 621, 793

Bamba, A., et al. 2008, PASJ, 60, in press, (ArXiv e-prints, 708, arXiv:0708.0073)

Barbon, R., Ciatti, F., & Rosino, L. 1973, A&A, 29, 57

Becker, R. H., Szymkowiak, A. E., Boldt, E. A., Holt, S. S., & Serlemitsos, P. J. 1980, ApJ, 240, L33

Bell, A. R. 1978, MNRAS, 182, 147

van den Bergh, S., & Tammann, G. A. 1991, ARA&A, 29, 363

Blandford, R. D., & Ostriker, J. P. 1978, ApJ, 221, L29

Bocchino, F., Vink, J., Favata, F., Maggio, A., & Sciortino, S. 2000, A&A, 360, 671

Bolton, J. G., Gardner, F. F., & Mackey, M. B. 1964, Australian Journal of Physics, 17, 340

Borkowski, K. J., Rho, J., Reynolds, S. P., & Dyer, K. K. 2001, ApJ, 550, 334

Bressaard, P. J., & van de Hulst, H. C. 1962, Rev. Mod. Phys., 34, 507

Burrows, A., Hayes, J., & Fryxell, B. A. 1995, ApJ, 450, 830

Caswell, J. L., Clark, D. H., & Crawford, D. F. 1975, Australian Journal of Physics Astrophysical Supplement, 39

Chevalier, R. A. 1974, ApJ, 188, 501

Chevalier, R. A., & Klein, R. I. 1978, ApJ, 219, 994

Chu, Y.-H., & Kennicutt, R. C., Jr. 1988, AJ, 96, 1874

Cioffi, D. F., McKee, C. F., & Bertschinger, E. 1988, ApJ, 334, 252

Decourchelle, A., et al. 2001, A&A, 365, L218

Dickel, J. R., Strom, R. G., & Milne, D. K. 2001, ApJ, 546, 447

Dickey, J. M., & Lockman, F. J. 1990, ARA&A, 28, 215

Dubner, G. M., Giacani, E. B., Goss, W. M., Green, A. J., & Nyman, L.-Å. 2002, A&A, 387, 1047

Dwarkadas, V. V., & Chevalier, R. A. 1998, ApJ, 497, 807

Elias, J. H., Matthews, K., Neugebauer, G., & Persson, S. E. 1985, ApJ, 296, 379

Feast, M., Whitelock, P., & Menzies, J. 2002, MNRAS, 329, L7

Ferrière, K. M. 2001, Reviews of Modern Physics, 73, 1031

Fink, H. H., Asaoka, I., Brinkmann, W., Kawai, N., & Koyama, K. 1994, A&A, 283, 635

Gaetz, T. J., Butt, Y. M., Edgar, R. J., Eriksen, K. A., Plucinsky, P. P., Schlegel, E. M., & Smith, R. K. 2000, ApJ, 534, L47

Gamezo, V. N., Khokhlov, A. M., & Oran, E. S. 2005, ApJ, 623, 337

Gardner, F. F., & Milne, D. K. 1965, AJ, 70, 754

Ghavamian, P., Raymond, J., Smith, R. C., & Hartigan, P. 2001, ApJ, 547, 995

Ghavamian, P., Winkler, P. F., Raymond, J. C., & Long, K. S. 2002, ApJ, 572, 888

Green, D. A. 1984, MNRAS, 209, 449

Green D. A. 2006, A Catalogue of Galactic Supernova Remnants (`http://www.mrao.cam.ac.uk/surveys/snrs/`)

Gull, S. F. 1973, MNRAS, 161, 47

Gull, S. F. 1975, MNRAS, 171, 263

Hachisu, I., Kato, M., & Nomoto, K. 1996, ApJ, 470, L97

Hamilton, A. J. S., Fesen, R. A., Wu, C.-C., Crenshaw, D. M., & Sarazin, C. L. 1997, ApJ, 481, 838

Hendrick, S. P., & Reynolds, S. P. 2001, ApJ, 559, 903

Herant, M., Benz, W., Hix, W. R., Fryer, C. L., & Colgate, S. A. 1994, ApJ, 435, 339

Hess, V. F. 1912, Phys. Zeits., 13, 1084

van der Heyden, K. J., Behar, E., Vink, J., Rasmussen, A. P., Kaastra, J. S., Bleeker, J. A. M., Kahn, S. M., & Mewe, R. 2002, A&A, 392, 955

Hoppe, S., Lemoine-Goumard, M., & for the H. E. S. S. Collaboration 2007, ArXiv e-prints, 709, arXiv:0709.4103

Hughes, J. P., et al. 1995, ApJ, 444, L81

Hughes, J. P. 1996, Bulletin of the American Astronomical Society, 28, 1334

Hughes, J. P., Rakowski, C. E., Burrows, D. N., & Slane, P. O. 2000a, ApJ, 528, L109

Hughes, J. P., Rakowski, C. E., & Decourchelle, A. 2000b, ApJ, 543, L61

Hughes, J. P. 2000, ApJ, 545, L53

Hwang, U., & Gotthelf, E. V. 1997, ApJ, 475, 665

Hwang, U., Hughes, J. P., & Petre, R. 1998, ApJ, 497, 833

Hwang, U., Holt, S. S., & Petre, R. 2000, ApJ, 537, L119

Hwang, U., Decourchelle, A., Holt, S. S., & Petre, R. 2002, ApJ, 581, 1101

Hwang, U., et al. 2004, ApJ, 615, L117

Ishisaki, Y., et al. 2007, PASJ, 59, 113

Iwamoto, K., Brachwitz, F., Nomoto, K., Kishimoto, N., Umeda, H., Hix, W. R., & Thielemann, F.-K. 1999, ApJS, 125, 439

Kaastra, J. S., Asaoka, I., Koyama, K., & Yamauchi, S. 1992, A&A, 264, 654

Karzas, W. J., & Latter, R. 1961, ApJS, 6, 167

Katz-Stone, D. M., Kassim, N. E., Lazio, T. J. W., & O'Donnell, R. 2000, ApJ, 529, 453

Kelley, R. L., et al. 2007, PASJ, 59, 77

Khokhlov, A. M. 1991, A&A, 245, 114

Kokubun, M., et al. 2007, PASJ, 59, 53

Koyama, K., Petre, R., Gotthelf, E. V., Hwang, U., Matsuura, M., Ozaki, M., & Holt, S. S. 1995, Nature, 378, 255

Koyama, K., Kinugasa, K., Matsuzaki, K., Nishiuchi, M., Sugizaki, M., Torii, K., Yamauchi, S., & Aschenbach, B. 1997, PASJ, 49, L7

Koyama, K., et al. 2007, PASJ, 59, 23

Ksenofontov, L. T., Berezhko, E. G., Volk, H. J. 2005, A&A, 443, 973

Laming, J. M. 2000, ApJS, 127, 409

Laming, J. M. 2001, ApJ, 546, 1149

Lee, J.-J., Koo, B.-C., & Tatematsu, K. 2004, Journal of Korean Astronomical Society, 37, 223

Lewis, K. T., Burrows, D. N., Hughes, J. P., Slane, P. O., Garmire, G. P., & Nousek, J. A. 2003, ApJ, 582, 770

Long, K. S., Helfand, D. J., & Grabelsky, D. A. 1981, ApJ, 248, 925

Long, K. S., Reynolds, S. P., Raymond, J. C., Winkler, P. F., Dyer, K. K., & Petre, R. 2003, ApJ, 586, 1162

Masai, K. 1984, Ap&SS, 98, 367

Masai, K. 1993, NASA STI/Recon Technical Report N, 94, 24866

Masai, K. 1994, ApJ, 437, 770

Mathewson, D. S., Ford, V. L., Dopita, M. A., Tuohy, I. R., Long, K. S., & Helfand, D. J. 1983, ApJS, 51, 345

Matsumoto, H., et al. 2006, Proc. SPIE, 6266

Matsunaga, K., Mizuno, N., Moriguchi, Y., Onishi, T., Mizuno, A., & Fukui, Y. 2001, PASJ, 53, 1003

McKee, C. F., & Ostriker, J. P. 1977, ApJ, 218, 148

Mills, B. Y., Slee, O. B., & Hill, E. R. 1961, Australian Journal of Physics, 14, 497

Minkowski, R. 1940, PASP, 52, 206

Minkowski, R. 1939, ApJ, 89, 156

Mitsuda, K., et al. 2007, PASJ, 59, 1

Miyata, E., Katsuda, S., Tsunemi, H., Hughes, J. P., Kokubun, M., & Porter, F. S. 2007, PASJ, 59, S163

Mueller, E., & Arnett, W. D. 1982, ApJ, 261, L109

Nakajima, H., et al. 2008, PASJ, 60, in press, (ArXiv e-prints, 705, arXiv:0705.1771)

Naranan, S., Shulman, S., Yentis, D., Fritz, G., & Friedman, H. 1977, ApJ, 213, L53

Nomoto, K., Sugimoto, D., & Neo, S. 1976, Ap&SS, 39, L37

Nomoto, K. 1982, ApJ, 253, 798

Nomoto, K., Thielemann, F.-K., & Yokoi, K. 1984, ApJ, 286, 644

Park, S., Roming, P. W. A., Hughes, J. P., Slane, P. O., Burrows, D. N., Garmire, G. P., & Nousek, J. A. 2002, ApJ, 564, L39

Park, S., Hughes, J. P., Slane, P. O., Burrows, D. N., Gaensler, B. M., & Ghavamian, P. 2007, ApJ, 670, L121

Petre, R., Allen, G. E., & Hwang, U. 1999, Astronomische Nachrichten, 320, 199

Pisarski, R. L., Helfand, D. J., & Kahn, S. M. 1984, ApJ, 277, 710

Rakowski, C. E. 2005, Advances in Space Research, 35, 1017

Rho, J., Dyer, K. K., Borkowski, K. J., & Reynolds, S. P. 2002, ApJ, 581, 1116

Rosado, M., Ambrocio-Cruz, P., Le Coarer, E., & Marcelin, M. 1996, A&A, 315, 243

Rothenflug, R., Ballet, J., Dubner, G., Giacani, E., Decourchelle, A., & Ferrando, P. 2004, A&A, 425, 121

Rybicki, G. B., & Lightman, A. P. 1979, New York, Wiley-Interscience, 1979. 393

Schaefer, B. E. 1996, ApJ, 459, 438

Sedov, L. I. 1959, Similarity and Dimensional Methods in Mechanics, New York: Academic Press, 1959

Serlemitsos, P. J., et al. 2007, PASJ, 59, 9

Slane, P., Plucinsky, P., Harrus, I. M., Hughes, J. P., Green, A. J., & Gaensler, B. M. 1997, Bulletin of the American Astronomical Society, 29, 1368

Smith, R. C., Kirshner, R. P., Blair, W. P., & Winkler, P. F. 1991, ApJ, 375, 652

Smith, R. C., Raymond, J. C., & Laming, J. M. 1994, ApJ, 420, 286

Smith, R. C. 1997, AJ, 114, 2664

Sokolsky, P. 1989, Frontiers in Physics, 76

Spitzer, L. 1962, Physics of Fully Ionized Gases, New York: Interscience (2nd edition), 1962

Stephenson, F. R., & Green, D. A. 2002, Historical Supernovae and their Remnants (Oxford: Oxford University Press)

Takahashi, T., et al. 2007, PASJ, 59, 35

Tanimori, T., et al. 1998, ApJ, 497, L25

Tawa, N., et al. 2008, PASJ, 60, in press

Thielemann, F.-K., Nomoto, K., & Hashimoto, M.-A. 1996, ApJ, 460, 408

Tomida, H. 1999, PhD thesis, Kyoto University.

Truelove, J. K., & McKee, C. F. 1999, ApJS, 120, 299

Tuohy, I. R., Dopita, M. A., Mathewson, D. S., Long, K. S., & Helfand, D. J. 1982, ApJ, 261, 473

Ueno, M. 2005, PhD thesis, Kyoto University.

Ueno, M., et al. 2007, PASJ, 59, S171

Vink, J., Kaastra, J. S., & Bleeker, J. A. M. 1996, A&A, 307, L41

Vink, J., Kaastra, J. S., & Bleeker, J. A. M. 1997, A&A, 328, 628

Vink, J., Kaastra, J. S., Bleeker, J. A. M., & Bloemen, H. 2000a, Advances in Space Research, 25, 689

Vink, J., Kaastra, J. S., Bleeker, J. A. M., & Preite-Martinez, A. 2000b, A&A, 354, 931

Vink, J., Laming, J. M., Gu, M. F., Rasmussen, A., & Kaastra, J. S. 2003, ApJ, 587, L31

Vink, J., Bleeker, J., van der Heyden, K., Bykov, A., Bamba, A., & Yamazaki, R. 2006, ApJ, 648, L33

Warren, J. S., & Hughes, J. P. 2004, ApJ, 608, 261

Westerlund, B. E. 1969, AJ, 74, 879

Wheeler, J. C. 1982, NATO ASIC Proc. 90: Supernovae: A Survey of Current Research, 167

Wheeler, J. C., Harkness, R. P., Barker, E. S., Cochran, A. L., & Wills, D. 1987, ApJ, 313, L69

Wheeler, J. C., Piran, T., & Weinberg, S. 1990, Supernovae, Jerusalem Winter School for Theoretical Physics

Winkler, P. F., Gupta, G., & Long, K. S. 2003, ApJ, 585, 324

Winkler, P. F., Long, K. S., Hamilton, A. J. S., & Fesen, R. A. 2005, ApJ, 624, 189

Woosley, S. E., & Weaver, T. A. 1994, ApJ, 423, 371

Wu, C.-C., Crenshaw, D. M., Fesen, R. A., Hamilton, A. J. S., & Sarazin, C. L. 1993, ApJ, 416, 247

Yamaguchi, H., et al. 2006, Proc. SPIE, 6266

Yamaguchi, H., et al. 2008a, PASJ, 60, in press, (ArXiv e-prints, 706, arXiv:0706.4146)

Yamaguchi, H., Koyama, K., Nakajima, H., Bamba, A., Yamazaki, R., Vink, J., & Kawachi, A. 2008b, PASJ, 60, in press, (ArXiv e-prints, 709, arXiv:0709.3151)

Yamazaki, R., Yoshida, T., Terasawa, T., Bamba, A., & Koyama, K. 2004, A&A, 416, 595

Acknowledgments

I deeply appreciate the guidance and support by Professor Katsuji Koyama. I am very grateful to my collaborators, especially Satoru Katsuda and Hiroshi Nakajima (Osaka University), John P. Hughes (Rutgers University), Jacco Vink (University Utrecht), Aya Bamba (ISAS/JAXA), Akiko Kawachi (Tokai University), Koji Mori (Miyazaki University), Junko S. Hiraga (RIKEN), and Ryo Yamazaki (Hiroshima University). Many helpful comments were given by Shuichiro Inutsuka (Kyoto University) and Masaomi Tanaka (University of Tokyo).

I would like to thank most of the members of the Cosmic-ray laboratory in Kyoto University, especially Yoshiaki Hyodo and Hideyuki Mori, for their continuous discussions and technical supports. Kentaro Miuchi helped me to improve the manuscript. I also thank the Suzaku satellite, the XIS, and all members of the Suzaku Science Working Group (SWG).

This work is supported by JSPS Research Fellowship for Young Scientists, and the Grant-in-Aid for the 21st Century COE "Center for Diversity and Universality in Physics" from the Ministry of Education, Culture, Sports, Science and Technology (MEXT) of Japan.